The University of
Nottingham

CARBON NANOSTRUCTURES: FORMATION AND EVOLUTION IN THE LABORATORY AND THE ISM

Rachel Kathryn Elizabeth Gover, MSci

Thesis submitted to the University of Nottingham for the
degree of Doctor of Philosophy

October 2016

Abstract

The chemistry of large carbon-containing molecules in space is widely researched with notable advances including understanding of the aromatic infrared emission features in terms of their general origin in polycyclic aromatic hydrocarbon (PAH) molecules, identification of the fullerenes C_{60} and C_{70} as the largest molecules detected in the interstellar medium, and knowledge of the structure and composition of various solid-state interstellar grains. However, there remain major challenges.

The work described in this Thesis addresses some longstanding, unanswered questions in astrochemistry, such as the origin of variation in the profiles of the aromatic infrared bands, the route to formation of C_{60}, and the role of astrophysical grains in the reactions of carbon-containing species. This research was carried out using a range of laboratory and computational techniques, in combination with astronomical data, yielding new results that can be compared with existing work to find solutions to these problems.

The varying profile of the 11.2 μm aromatic infrared emission band within two objects, NGC 7023 and the Red Rectangle, is investigated. The feature's changing spectral shape, which depends on the position within the object, is interpreted in terms of variation in the distribution of molecular masses of the PAHs that give rise to the feature. This was achieved using a model that fits astronomical data which was obtained with the instrument MICHELLE on the UKIRT telescope in Hawaii and the Spitzer satellite observatory. Based on the calculated emission features of four neutral PAHs that are taken to represent 'low-mass' (fewer than 50 C atoms) or 'high-mass' (more than 50 C atoms), it is found that, with increasing distance from the star, there is an increase in the proportion of low-mass PAHs in NGC 7023, in good agreement with less specific previous studies that have been carried out using other approaches. The modelling results for the Red Rectangle indicate that the mass distribution does not change significantly with offset, although evidence from other sources appears in part to contradict this conclusion.

A laboratory investigation is detailed in which formation of C_{60} from PAH precursors is explored. Transmission electron microscopy (TEM) and matrix-assisted laser desorption/ionisation time-of-flight mass spectrometry (MALDI-TOF MS) are used to irradiate, using the electron beam (e-beam) in TEM and the UV laser in MALDI-TOF MS, samples of PAH molecules and to monitor the products of any resulting transformations within the samples. It is found that under both e-beam and UV irradiation, PAH molecules lose one or more H atoms and form larger PAH 'oligomers'. Based on the MALDI-TOF MS results, specific chemical structures of these oligomers are proposed, and it is found that the precursor molecules coronene and perylene give rise to formation of C_{60}. A mechanism is given for this process, in which an oligomer containing 60 carbon atoms or more is formed, and then 'shrinks' *via* loss of H atoms, C-C bond formation, and Stone-Wales rearrangements. Important structural features required for these mechanisms, namely the presence of 'bay' and 'fjord' carbon edge sites, are discussed in an astrophysical context. An experimental methodology was designed and implemented to use TEM and MALDI-TOF MS in conjunction with each other, in which a specific area of a PAH sample is viewed using low-dose TEM, is then irradiated using the UV laser in MALDI-TOF MS, and finally is viewed a second time using TEM to observe the effects of the UV irradiation.

Experiments were carried out to investigate reactions of acetylene and CO in the presence of astrophysically relevant grains. It was found that CO undergoes a disproportionation reaction over olivine grains, forming gaseous CO_2 and depositing solid-state carbon on the grain surface; this has implications for the formation of other carbonaceous species such as PAHs and even carbon nanotubes. The formation of PAHs from acetylene gas over grains of SiC is reported, in addition to the inhibiting impact of CO when mixed with acetylene. In one experiment olivine samples were irradiated by the e-beam in TEM, and decomposition of the olivine structure was seen to occur, resulting in the formation of metallic nanoparticles. This behaviour is discussed in terms of its likely occurrence in astrophysical environments such as the Red Rectangle, and its potential for catalysis that results from reactions of molecules on the metal nanoparticle surface.

Acknowledgements

I begin by expressing my utmost gratitude to my supervisors Professor Peter Sarre and Professor Andrei Khlobystov for their enthusiasm, inspiration and support throughout the course of my studies, in addition to their willingness and perseverance in embarking on this new collaboration.

I must also say how grateful I am to Dr Thomas Chamberlain, whose day-to-day guidance and encouragement has helped my scientific development and my confidence. His continued support even after leaving the group has meant a great deal to me.

I thank the Nottingham Nanoscale and Microscale Research Centre for the use of TEM, and thank Andrei for carrying out the TEM imaging for this project. My thanks extend to the Nottingham HPC facility, to Graham Coxhill and Mick Cooper for help with MALDI-TOF MS, to Stephen Skowron for helpful discussions, and to Graham Rance for carrying out Raman and for help with Raman analysis, in addition to many useful discussions. I also gratefully acknowledge the EPSRC for funding, and the RSC and The University of Nottingham for travel funding.

I am extremely grateful to Alessandra Candian for her assistance in the successful use of her emission model code, which contributed to a large portion of my PhD project. I would also like to thank Professor Allan Cheung and his research group at the University of Hong Kong for the collaboration that resulted in a significant proportion of the work presented in the fourth Chapter of this Thesis, and for hosting me for five weeks to carry out this research. In particular, I wish to thank Li Qian for her help with experiments during my visit to Hong Kong and the many useful discussions that we had.

My thanks extend to current and previous members of the Khlobystov group, who welcomed me with equal parts warmth and wit, and to whom I attribute a great number of fond memories: to Tom, Graham, Arran, Masha, Scott, Akos, Abdullah, Rob, Carlos, Mehtap, Rhys, Craig, Kate, Bradley, Julie and Max, in addition to the many project students who have passed through our midst. To current and previous members of the Sarre group, whom I joined as a young summer project student, thank you for your kindness and guidance: to Alessandra, Markus and Kyle, and particular thanks to Charlie Marshall, for being a friend and an ally through the ups and downs, for our many lengthy chats, and for always being understanding.

I would especially like to thank Becca Blundell for her patience, encouragement and, above all, friendship, which has seen me through every aspect of my PhD. In the many years I have known her she has helped me in more ways than I can count.

Finally, I would like to thank my parents. I am very lucky to have their support and boundless love, and I know that it is their belief in me that has helped me to achieve all that I have.

Table of Contents

1. Introduction

1.1 Molecules in the interstellar medium

Since the initial observation of diatomic molecules in the interstellar medium (ISM) back in the 1930s,[1] the abundance and ubiquity of molecules, both simple and complex, in space has come to be realised. The molecular inventory of the ISM is created by the ejection of material from stars, often towards the end of their lifetimes, and the molecules in turn go on to cycle between the diffuse ISM and dense molecular clouds – the latter being the birthplace of new stars. In this way, the molecules of the ISM are extremely important in the evolution of galaxies. To date, over 170 molecules have been identified in the ISM and circumstellar environments, ranging from simple diatomic and triatomic species to hydrocarbon chains, radicals and ionised molecules, and large very stable molecules such as fullerenes. A list of detected interstellar and circumstellar molecules is given by Muller *et al.*[2]

Molecules are detected *via* their rotational, vibrational, and/or electronic spectra. One particular class of molecules, polycyclic aromatic hydrocarbons (PAHs), has been identified through a set of emission features – known as the aromatic infrared bands – matching closely with their vibrational transitions, and have been found to be very abundant in astrophysical environments. The aromatic infrared bands and PAHs are discussed further in Sections 1.2 and 1.3, respectively. The largest molecules to have been detected in space are the fullerenes C_{60} and C_{70}, by means of their vibrational emission spectra. More recently, C_{60}^+ has also been confirmed, by the detection of IR emission features,[3] and by comparison of its electronic spectrum with two interstellar absorption features that are part of a larger family known as the diffuse interstellar bands (DIBs).[4] A more detailed discussion of fullerenes is given in Section 1.4.

With regards to the formation of the molecules that have been detected, the ‘bottom-up’ route of ion-molecule reactions was for a long time considered to be the main, if not only, pathway. It is now widely recognised, however, that surface reactions on bare cosmic dust grains and in ices play an important role in the formation and evolution of molecular species. Interstellar dust grains are identified through a combination of extinction, *i.e.* starlight being obscured, and specific spectral features, and are discussed in Section 1.5.

1.2 The aromatic infrared bands

The aromatic infrared bands (AIBs), sometimes referred to as the unidentified infrared (UIR) bands, are a set of emission features that were first observed in 1973, in three planetary nebulae.[5] In the years since, the AIBs have been seen in a huge range of objects, their pervasiveness suggestive of the abundance of their carriers. The set of AIBs include strong peaks that fall at 3.3, 6.2, 7.7, 8.6, 11.2 and 12.7 μm, which are often accompanied by a range of weaker features, and which reside on broader underlying plateaux. The carriers of these bands are widely accepted to be gas-phase PAH molecules,[6, 7] which as a class of molecules have vibrational spectra closely matching the AIBs. Identification of an individual specific PAH molecule from these spectra, however, has yet to be attained.

1.2.1 Band assignments

The AIBs are characteristic of the vibrational transition frequencies of PAHs, and each feature can be attributed to a stretching or bending mode of this class of molecule. The 3 μm region encompasses C-H stretching modes, and the 3.3 μm (~ 3030 cm^{-1}) band is assigned to C-H stretching within aromatic molecules. The exact frequency of this C-H stretch was found to be dependent on the ‘type’ of H atom, when further analysis of the 3.3 μm band led to the discovery of two components – 3.28 and 3.30 μm – contributing to the overall feature,[8] which were later assigned to ‘bay’ and ‘non-bay’ hydrogens, respectively.[9] The usually weaker 3.4 μm band sometimes seen in spectra is characteristic of an aliphatic C-H stretch, and hence indicates an aliphatic component, either as alkyl functional groups or as hydrogenated PAHs with extra hydrogen atoms in some peripheral positions.[10]

The 6 – 9 μm (~ 1600 – 1100 cm^{-1}) region covers skeletal C-C stretching, C-H in-plane bending, and combination modes. These modes, and hence their frequencies, are variable, and it is more difficult to accurately assign each feature. Indeed, there is still some debate surrounding the 6.2 μm AIB, for which a satisfactory assignment has not yet been achieved, and which is currently commonly believed may belong to N-substituted PAHs.[11] In addition, the 6 – 9 μm region is generally associated with PAH cations, for which the features that fall between these wavelengths are more intense.

The final region of the main AIB spectrum, at 10 – 15 μm (~ 1000 – 660 cm^{-1}), holds the features assigned to the C-H out-of-plane (OOP) bending modes of PAHs. The exact peak position for a C-H OOP bend feature has been found to be dependent on the number of adjacent hydrogen atoms on the same six-membered ring.[12] The hydrogen atoms are categorised in the following way: solo H atoms are on their own on a six-membered ring, *i.e.* they have no adjacent C-H groups. Duo H atoms are two adjacent C-H groups on the same six-membered ring, trios are three adjacent C-H groups, and quartets are four adjacent C-H groups – these are illustrated in Figure 1.1.

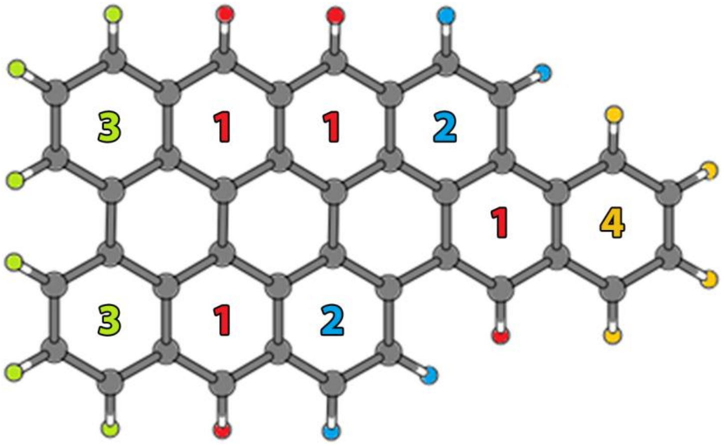

Figure 1.1. An example PAH structure with the different hydrogen atom types labelled. Solo hydrogen atoms (red) have no adjacent hydrogen atoms on the same six-membered ring, duos (blue) are two adjacent hydrogen atoms on the same ring, trios (green) are three, and quartets (yellow) are four.

Rows of solo H atoms can also be thought of as ‘zig-zag’ edges of a PAH, and rows of duos can be thought of as ‘armchair’ edges. The solo OOP bend is responsible for the strong 11.2 μm band, duo modes tend to fall between 11.7

and 12.8 μm, trios at around 13 μm and quartets between around 13 and 13.7 μm. Due to the sensitivity of the vibrational spectra in this region to the type of H atoms present, these bands can provide insight into the edge structure of their PAH carriers. For example, a strong 11.2 μm feature relative to any others is indicative of a large number of solo H atoms, which are associated with straight, zig-zag edges, whereas duos can be suggestive of armchair edges, and trios are usually found on 'corners', indicating a more irregular, less compact structure.

Some aspects of the AIBs within the 10 – 15 μm range are attributed to PAH cations, rather than neutral molecules. For example, it is suggested that the profile of the 12.7 μm band is better matched by the trios of PAH cations,[12] that there is a contribution to the longer wavelength part of the 11.2 μm band from cationic PAH duos,[13] and that the 11.0 μm feature sometimes seen accompanying the 11.2 μm band is due to the solo C-H OOP bend of PAH cations.[12, 13]

1.2.2 Band variations

The AIBs can exhibit variations in their relative intensities, peak positions, and profile (shape). These variations have been noted *between* different objects,[14, 15] and at different spatial positions *within* the same object.[8, 16, 17] The fact that the AIBs can vary in this way indicates their sensitivity to their carriers and to local conditions, and for this reason many studies have been carried out to determine the origin of the variations and hence learn more about the objects and areas being observed.

The profiles of some of the AIBs are very distinctive. For example, both the 6.2 and 11.2 μm bands exhibit, in most cases, a characteristic asymmetry, with a steep blue edge and an extended red tail. In both cases, shifts in this profile are seen and have been investigated.

Peeters *et al*. classified a number of objects based on the profile of their 6.2 μm features, and additional variations in the 6 – 9 μm region.[14] Their 'Class A' objects exhibited a 6.2 μm band with a steep blue side and a red tail, in addition to a '7.7' feature that peaks at 7.6 µm. 'Class B' objects showed a more symmetric 6.2 µm feature that peaked at longer wavelengths, along with a '7.7' feature of longer wavelength also. 'Class C' objects, whose 6.2 µm features landed at 6.3 µm, showed a broad emission at 8.2 µm and no feature at 7.7 µm. The changes in the features in this region appear to be correlated – *i.e.* the bands shift in the same way between sources. The authors attributed these shifts to the nature of the carriers, assigning the 6.2 µm component to N-substituted PAHs and the 6.3 µm component to pure PAHs. This implies that a longer wavelength peak (*i.e.* in Class B and C objects) is associated with a more intense 6.3 µm component and hence reflects a larger proportion of pure PAHs. It was found that a 7.6 µm component was well-matched with both pure and substituted PAHs, but that the carriers of both the 7.8 µm component and the broad 8.2 µm emission remain unknown.

Similarly, a classification of objects based on the profiles of their 3.3 µm and 11.2 µm bands, *i.e.* those attributed to C-H modes, was carried out by van Diedenhoven *et al.*[15] It was found that Class $A_{11.2}$ objects had 11.2 µm features with shorter peak wavelengths (11.20 – 11.24 µm), a steep blue edge and a shorter red tail. Class $B_{11.2}$ in general exhibited slightly higher peak positions (~ 11.25 µm), a less steep blue edge and a more extended red tail. Some objects were classified as Class $A(B)_{11.2}$, and these show the characteristics of Class $A_{11.2}$ objects in terms of the peak position and steepness of the blue edge, but have a more extended red tail, similar to Class $B_{11.2}$. Finally, Class $C_{11.2}$ objects, less commonly seen, exhibit longer peak wavelengths and are more symmetric in appearance. To illustrate these variations, Figure 1.2 gives examples of the 11.2 µm bands of two objects, NGC 7023 and the Red Rectangle. In this Figure, the 11.2 µm band of NGC 7023 can be seen to have a profile that would fall into the Class $A_{11.2}$ category, while that of the Red Rectangle appears closer to Class $B_{11.2}$. The specific examples of these two objects, and the origin of the 11.2 µm profile variations, are discussed in further detail in Chapter 2 of this Thesis.

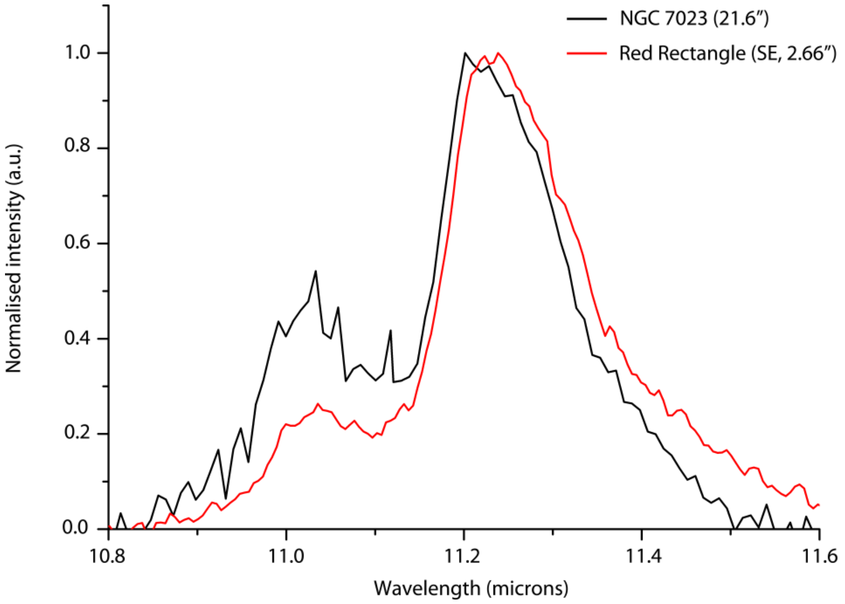

Figure 1.2. Examples of the 11.2 μm feature from NGC 7023 (black) and the Red Rectangle (red), to illustrate the variation in peak position and profile. The NGC 7023 data are taken at 21.6" from the exciting star, and are from the *Spitzer* Infrared Spectrograph (IRS) short-wavelength-high-resolution (SH) spectral map of NGC-7023-NW. The Red Rectangle data are taken at 2.66" along the South East 'whisker', and were obtained using the MICHELLE instrument at the United Kingdom Infrared Telescope (UKIRT). Both data sets are discussed in Chapter 2 of this Thesis.

In the same work,[15] objects were classified based on their 3.3 μm bands. Class $A_{3.3}$ was found to have a symmetric profile and to peak at ~ 3.290 μm, while Class $B1_{3.3}$ and $B2_{3.3}$ were asymmetric with slightly longer peak wavelengths of ~ 3.297 and ~ 3.293 μm, respectively. The authors reported some correlation between their classified objects and those from the earlier 6 – 9 μm work,[14] but state that there is a much stronger correlation between the profile class and object type in the 6 – 9 μm region than for the 3.3 μm and 11.2 μm bands.

1.3 Polycyclic aromatic hydrocarbon molecules

1.3.1 PAH structure

PAHs are molecules made up of fused benzene rings, and have also been referred to as hydrogen-terminated graphene flakes. Six-membered rings can adopt many arrangements, and hence there are a vast number of PAH molecules, some examples of which are shown in Figure 1.3.

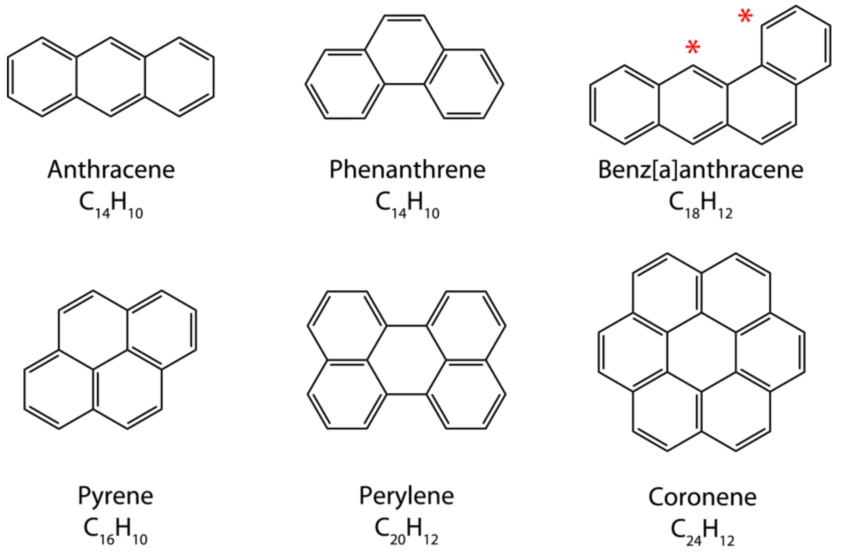

Figure 1.3. A selection of PAH molecules. The red asterisks indicate an example of ‘bay’ hydrogen positions.

PAH molecules have some interesting structural features that can impact upon their spectra and potential reactivity. As mentioned in Section 1.2.1, a PAH’s hydrogen atoms can be defined as solo, duo, trio or quartet (and more rarely, quintet). The number of each of these a PAH molecule has affects its vibrational spectrum, especially in the 10 – 15 μm region. The H atoms on a PAH can also be categorised as ‘bay’ or ‘non-bay’, the bay hydrogens being on either side of a ‘notch’ in the edge of a PAH so that they are facing slightly towards each other, and such that their stretching modes may interfere. Examples of bay hydrogen positions are indicated by the red asterisks in Figure 1.3. In addition, some PAHs have five-membered rings included in their structures – corannulene, for example – which induce curvature in the structure. Others can have heteroatoms incorporated, replacing one or more carbon atoms, the most commonly discussed in an astrophysical context being nitrogen-substituted PAHs.

1.3.2 Spectroscopy of PAHs

Since the assignment of PAHs as the carriers of the AIBs,[6, 7, 18] much effort, both experimental and theoretical, has been put into understanding the spectroscopy of these molecules and obtaining as close a match to astronomical data as possible. The AIBs are believed to occur as a result of the absorption, by a PAH, of a UV/visible photon which results in the molecule being heated to a high internal temperature, before cooling through its vibrational modes, resulting in IR emission.[6, 7, 18-20]

Many experiments have been carried out to measure the IR spectra of PAHs, in conditions as relevant to astronomical spectra as possible. A review of laboratory IR spectroscopy of PAHs is given by Oomens,[21] in which the most commonly used techniques are summarised. The problem with achieving laboratory spectra that can be compared directly with astronomical spectra is that the AIBs originate from gas-phase PAH molecules, and are seen in *emission*, whereas most laboratory techniques measure the *absorption* spectra of molecules.

A popular and widely-used technique is matrix isolation spectroscopy, in which a PAH and an inert gas, such as Ar or Ne, are condensed simultaneously onto an optical window that is kept at cryogenic temperatures. This technique has been used in a number of studies on ‘pure’ PAHs,[22, 23] PAH cations,[24-26] N-substituted PAHs,[27] and in an investigation into the far-IR spectra of PAHs.[28] While matrix isolated spectra are typically recorded at high resolution, and produce peaks with wavelengths that fall within about 1% of gas-phase results, band intensities have been found to vary significantly and hence there is some question as to the effect of the matrix on the results.[29] Gas-phase spectra, preferable because of their astrophysical relevance, are difficult to record due to the low vapour pressures of PAHs. This can be addressed by the use of an oven within the spectrometer,[29] although this produces significantly broader linewidths than matrix isolated spectra.

In addition to laboratory measurements, there is now a huge amount of computational data on the vibrational frequencies of PAH molecules. The most popular computational technique for these calculations is overwhelmingly density functional theory (DFT), and many results of theoretical studies have been brought together and are available from the

NASA Ames PAH IR Spectroscopic Database (www.astrochem.org/pahdb).[30] This database contains the theoretical spectra of approximately 700 different PAH molecules, and covers neutral PAHs, cations and anions, in addition to N-substituted PAHs.

1.3.3 Formation and evolution of PAHs

The formation of astrophysical PAH molecules has been discussed largely in the context of the outflows of carbon stars,[31] where conditions are expected to be similar to those in the high temperature sooting environments, such as flame chemistry, where PAHs are found terrestrially. Mechanisms that have been explored in these environments generally involve acetylene (C_2H_2) as a precursor to benzene formation, followed by addition of further acetylene units to radical sites to build up the PAH structure.[32, 33] More recently, the activation of acetylene on surfaces of oxygen-containing cosmic dust analogues has been investigated, and it was found that PAHs could be formed from acetylene in the presence of alumina, pyroxenes[34] or olivines.[35] Silicon carbide (SiC) grains have also been explored in this connection, as discussed in Chapter 4 of this Thesis, and have been found to perform a similar role, resulting in the formation of PAH molecules.[36] The involvement of SiC grains in PAH formation processes has also been proposed by Merino *et al.*[37] who invoked the etching of graphene layers formed on the surface of SiC grains by hydrogen atoms as the origin of PAH molecules.

The chemistry and evolution of PAHs, once formed, is driven in part by the photochemistry of these molecules. It is known that under UV photon irradiation, PAHs can lose H atoms, and can become fully dehydrogenated.[38, 39] On full dehydrogenation, photon-induced loss of C atoms from the structure can lead to fragmentation, resulting in smaller planar structures, rings or chains, or isomerisation, and on towards cages and fullerene structures.[40]

1.4 The C_{60} fullerene

1.4.1 Discovery of terrestrial and interstellar C_{60}

The fullerene C_{60}, a molecule with a truncated icosahedron structure like that of a traditional black and white soccer ball, was discovered in 1985 by means of a set of experiments originally directed towards investigating the formation of long-chain carbon molecules analogous to those found in the ISM.[41] During laser irradiation of graphite, in which products were detected by time-of-flight MS, a peak corresponding to C_{60} dominated significantly over other peaks. Due to the remarkable stability of the C_{60} molecule implied by this, a spheroidal structure was proposed to satisfy all valences. The molecule's stability additionally prompted the authors to suggest that it may be expected that C_{60} is widely distributed throughout the Universe.

Some years later, a vibrational emission spectrum of C_{60} was detected in a planetary nebula[42] and in reflection nebulae.[43, 44] The initial detection provided the necessary information to prompt successful searches for this molecule in many more objects, including those in their later stages of stellar evolution,[45-51] as well as some young stellar objects (YSOs).[52] Despite having four infrared active bands in its vibrational spectrum, C_{60} is usually first identified in astronomical spectra by its 18.9 μm feature, which is often the only one that can be easily distinguished from the intense PAH bands.

1.4.2 Formation of C_{60}

In the laboratory, C_{60} is commonly synthesised by electric arc vaporisation of carbon rods[53] or through the incomplete combustion of hydrocarbons,[54] however the exact formation mechanism is not known for either of these processes. Similarly, the formation mechanism of interstellar C_{60} has been the topic of much discussion following its detection.

C_{60} formation mechanisms can be categorised into two types: 'bottom-up' and 'top-down'. Bottom-up routes have largely been the main focus of the laboratory formation of C_{60},[55-57] as the building up of fullerene cages from carbon atoms, C_2 units or small carbon clusters would be expected in the high temperature carbon-rich environments involved in carbon rod vaporisation or hydrocarbon combustion. These bottom-up mechanisms, however, are applicable to only a narrow range of astrophysical environments due to the high temperatures and densities needed for it to occur on a reasonable timescale.[40, 58] Other mechanistic routes must therefore be considered to account for the abundance of C_{60} detected, and the range of objects in which it is seen, and attention has turned in more recent years to top-down mechanisms.

Experiments using transmission electron microscopy (TEM) to image the fullerene formation process have revealed that under electron beam (e-beam) irradiation, flakes of graphene can roll up to form a fullerene.[59] Combined with quantum chemical modelling, a top-down mechanism has been proposed for this fullerene formation, in which the loss of carbon atoms from the edge of the graphene results in the formation of pentagons within the structure. This pentagon formation is a key step in the process, as it introduces curvature into the previously planar species, which then drives the system to 'zip-up' to form the fullerene. The mechanism, with the calculated energies of the required intermediates, is given in Figure 1.4. This figure demonstrates the stability of the fullerene molecules and hence the overall driving force of the process.

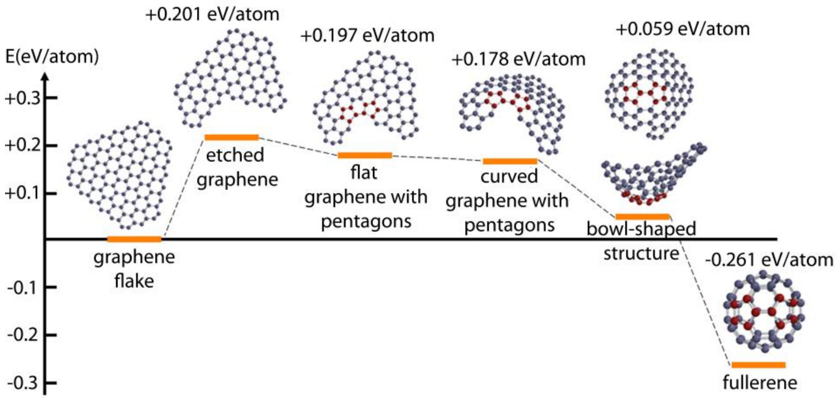

Figure 1.4. Adapted with permission from Chuvilin *et al.*,[59] a scheme showing a flake of graphene undergoing transformations including C-atom loss and pentagon formation to form a fullerene. Energies corresponding to each of the intermediates are shown, illustrating the stability of the fullerene product.

In astrophysical environments also, it appears that top-down routes to fullerene formation are important. Berné and Tielens proposed a mechanism analogous to the TEM graphene-to-fullerene transformation of Chuvilin *et al.*,[59] in which PAHs of approximately 70 C atoms were the precursors to fullerenes.[40] Under UV irradiation, these PAHs would be dehydrogenated, and would then, *via* the loss of a C atom from a zig-zag edge, form a pentagon at this position, initiating the zipping up of the fullerene cage. In contrast, Micelotta *et al.* proposed a model in which the photochemical processing of hydrogenated amorphous carbon (HAC), rather than PAH molecules, acted as a precursor to fullerene formation.[58] It was suggested that this originated in a type of structure the authors termed 'arophatic' – aromatic clusters linked by aliphatic groups – which would shrink down by ejecting C_2 units to form C_{60} or C_{70} fullerenes. However, it has been noted since that a route requiring aliphatic-containing particles would not be feasible based on the low abundance of aliphatic groups in some objects.[60] In the laboratory, experiments carried out by Zhen *et al.* have demonstrated that the photofragmentation patterns of PAHs containing more than sixty carbon atoms lead to the formation of C_{60}.[61] More recently, modelling of specific transformations of circumovalene ($C_{66}H_{20}$) has detailed the key processes involved in the formation of C_{60} from this molecule, but led to the conclusion that for PAHs containing more than 66 carbon atoms the process would occur on unreasonably long timescales.[62]

1.5 Cosmic dust

The suggestion of the existence of cosmic dust grains was first made in 1930, when they were proposed to be the species causing the obscuration of starlight.[63] Dust grains are believed to have a typical size of up to 1 μm, and are usually classed as either carbonaceous or silicate grains, with some being encased in ices. Cosmic dust grains have been recognised as important components of the ISM for their part in grain-surface chemistry, in which they may act as either a catalyst or as a surface for the adsorption of atomic or molecular species. In particular, the role of cosmic grains in the formation of H_2, the most abundant molecule in the Universe, has received much attention.[64]

1.5.1 Carbonaceous grains

The term carbonaceous grains is used to encompass graphitic and amorphous carbon, as well as, in some cases, large PAH molecules, or PAH clusters.[65] There is thought to be a significant proportion of sp^2 carbon in these grains, due to the observation of a broad absorption feature at ~ 2175 Å,[66] whose carrier was first proposed to be small graphitic particles.[67] Since the initial observation of the feature, a number of carbon-based, sp^2-containing species have been suggested, including HAC particles,[68] carbon onion type structures,[69] and mixtures of PAHs.[70]

In the context of H_2 formation, many experiments have been carried out using carbonaceous dust grain analogues. It has been found that H_2 can form efficiently on the surface of highly ordered pyrolytic graphite (HOPG),[71-73] and on amorphous carbon.[74]

1.5.2 Silicate grains

Evidence for the existence of interstellar silicate grains lies in part in the apparent depletion in the abundance of some elements, including magnesium, silicon and iron, compared with the observed values in our Sun.[75] Amorphous silicates, which are believed to be the dominant form of these grains in the ISM,[76] were first observed in astronomical spectra by means of their characteristic broad absorption features at ~ 10 and 18 μm.[77] Crystalline silicates, which have sharper and more prominent spectroscopic features, have also been identified, usually in circumstellar environments.[78-80]

Silicate grains contain Si atoms coordinated to four O atoms, forming a tetrahedron. To balance the charge of this group, Mg and Fe (in the context of astrophysical grains particularly) cations are dispersed in between. Among the possible structures and compositions of silicate grains are groups known as neosilicates, which contain isolated $[SiO_4]^{4-}$ tetrahedra, and inosilicates, which contain chains of $[SiO_3]^{2-}$ groups.[81] Commonly discussed in an astrophysical context, olivines have the general formula $(Mg_xFe_{1-x})_2SiO_4$ and belong to the neosilicates group, and pyroxenes have the general formula $(Mg_xFe_{1-x})SiO_3$

and belong to the inosilicates group. The 10 and 18 μm features mentioned above are attributed to the Si-O stretching mode and O-Si-O bending mode of amorphous silicates, respectively. In crystalline silicates, vibrational spectra are more complicated; olivines exhibit bands between 10 and 11.6 μm, due to asymmetric stretches, and have bending modes that fall at 16, 20 and 23 μm.[81] In addition, both olivines and pyroxenes exhibit shifts in peak positions depending on the relative Fe content within a particular structure.[79]

H_2 formation on the surface of silicate grains (olivines, in particular) has been investigated and found to be an efficient process within a certain temperature range.[82, 83] As mentioned earlier, the catalytic capability of silicate grains has also been extended to the formation of PAH molecules, in studies demonstrating the production of PAHs from acetylene over pyroxenes, alumina and olivines.[34, 35]

1.6 Thesis overview

The aim of the work described in this Thesis was to develop the current knowledge of certain areas of astrophysical chemistry, particularly those concerning carbon-containing species, by using a combination of laboratory and theoretical techniques to investigate some of the unresolved problems facing researchers. To that end, this Thesis is laid out as follows:

Chapter 2 describes a computational study into the relationship between the distribution of masses of PAH molecules in a population and the profile of the 11.2 μm solo OOP bend feature. Two objects are studied – NGC 7023 and the Red Rectangle – in the context of tracking the variation in the size of PAHs *within* each object.

Chapter 3 presents the results of a laboratory exploration of the mechanism of formation of interstellar fullerenes and their origins from PAH molecules. The products of irradiation-induced transformations of PAHs are determined, and mechanistic steps to fullerene formation are proposed. A new, combined-technique experimental methodology for the irradiation and monitoring of samples is detailed.

Chapter 4 investigates catalytic reactions of cosmic dust analogues, specifically olivine and SiC grains. Some of the lesser-discussed reactions are explored, including reactions of CO on grains, and the formation of PAH molecules. The behaviour of olivine grains, both ‘bare’ and carbon-coated, under e-beam irradiation is also examined.

Finally, Chapter 5 summarises the main conclusions of each of these studies, and brings them together to demonstrate the ways in which the research described in this Thesis forms a coherent body of work.

1.7 References

1. P. Swings and L. Rosenfeld, *ApJ*, 1937, **86**, 483-486.
2. H. S. G. Muller, C. P. Endres, J. Stutzki and S. Schlemmer, *The Cologne Database for Molecular Spectroscopy: Molecules in Space*, 2016.
3. O. Berné, G. Mulas and C. Joblin, *Astron. Astrophys.*, 2013, **550**.
4. E. K. Campbell, M. Holz, D. Gerlich and J. P. Maier, *Nature*, 2015, **523**, 322 - 323.
5. F. C. Gillett, W. J. Forrest and K. M. Merrill, *ApJ*, 1973, **183**, 87-93.
6. L. J. Allamandola, A. G. G. M. Tielens and J. R. Barker, *ApJ SS*, 1989, **71**, 733-775.
7. J. L. Puget and A. Léger, *Ann. Rev. Astron. Astrophys.*, 1989, **27**, 161-198.
8. I.-O. Song, J. McCombie, T. H. Kerr and P. J. Sarre, *MNRAS*, 2007, **380**, 979-985.
9. A. Candian, T. H. Kerr, I.-O. Song, J. McCombie and P. J. Sarre, *MNRAS*, 2012, **426**, 389-397.
10. W. A. Schutte, A. G. G. M. Tielens and L. J. Allamandola, *ApJ*, 1993, **415**, 397-414.
11. D. M. Hudgins, C. W. Bauschlicher and L. J. Allamandola, *ApJ*, 2005, **632**, 316-332.
12. S. Hony, C. Van Kerckhoven, E. Peeters, A. G. G. M. Tielens, D. M. Hudgins and L. J. Allamandola, *Astron. Astrophys.*, 2001, **370**, 1030-1043.

13. D. M. Hudgins and L. J. Allamandola, *ApJ*, 1999, **516**, L41-L44.

14. E. Peeters, S. Hony, C. Van Kerckhoven, A. G. G. M. Tielens, L. J. Allamandola, D. M. Hudgins and C. W. Bauschlicher, *Astron. Astrophys.*, 2002, **390**, 1089-1113.

15. B. van Diedenhoven, E. Peeters, C. Van Kerckhoven, S. Hony, D. M. Hudgins, L. J. Allamandola and A. G. G. M. Tielens, *ApJ*, 2004, **611**, 928-939.

16. C. Boersma, J. D. Bregman and L. J. Allamandola, *ApJ*, 2013, **769**, 117.

17. M. J. Shannon, D. J. Stock and E. Peeters, *ApJ*, 2016, **824**.

18. A. Léger and J. L. Puget, *Astron. Astrophys.*, 1984, **137**, L5-L8.

19. K. Sellgren, *ApJ*, 1984, **277**, 623-633.

20. A. G. G. M. Tielens, *Ann. Rev. Astron. Astrophys.*, 2008, **46**, 289-337.

21. J. Oomens, *EAS Pub. Ser.*, 2011, **46**, 61-73.

22. D. M. Hudgins and S. A. Sandford, *J. Phys. Chem. A*, 1998, **102**, 329-343.

23. D. M. Hudgins and S. A. Sandford, *J. Phys. Chem. A*, 1998, **102**, 344-352.

24. J. Szczepanski and M. Vala, *ApJ*, 1993, **414**, 646-655.

25. D. M. Hudgins and L. J. Allamandola, *J. Phys. Chem.*, 1995, **99**, 3033-3046.

26. D. M. Hudgins and L. J. Allamandola, *J. Phys. Chem.*, 1995, **99**, 8978-8986.

27. A. L. Mattioda, D. M. Hudgins, C. W. Bauschlicher, M. Rosi and L. J. Allamandola, *J. Phys. Chem. A*, 2003, **107**, 1486-1498.

28. A. L. Mattioda, A. Ricca, J. Tucker, C. W. Bauschlicher and L. J. Allamandola, *AJ*, 2009, **137**, 4054-4060.

29. C. Joblin, L. d'Hendecourt, A. Léger and D. Défourneau, *Astron. Astrophys.*, 1994, **281**, 923-936.

30. C. W. Bauschlicher, Jr., C. Boersma, A. Ricca, A. L. Mattioda, J. Cami, E. Peeters, F. S. de Armas, G. P. Saborido, D. M. Hudgins and L. J. Allamandola, *ApJS*, 2010, **189**, 341-351.

31. I. Cherchneff, in *PAHs and the Universe: A Symposium to Celebrate the 25th Anniversary of the PAH Hypothesis*, eds. C. Joblin and A. G. G. M. Tielens, E D P SCIENCES, 2011, vol. 46, pp. 177-189.

32. M. Frenklach and E. D. Feigelson, *ApJ*, 1989, **341**, 372-384.

33. I. Cherchneff, J. R. Barker and A. G. G. M. Tielens, *ApJ*, 1992, **401**, 269-287.

34. M. Tian, B. S. Liu, M. Hammonds, N. Wang, P. J. Sarre and A. S. C. Cheung, *Phil. Trans. R. Soc. A*, 2013, **371**, 20110590.

35. M. Tian, B. S. Liu, M. Hammonds, N. Wang, P. J. Sarre and A. S. C. Cheung, *Phys. Chem. Chem. Phys.*, 2012, **14**, 6603-6610.

36. T. Q. Zhao, Q. Li, B. S. Liu, R. K. E. Gover, P. J. Sarre and A. S. C. Cheung, *Phys. Chem. Chem. Phys.*, 2016, **18**, 3489-3496.

37. P. Merino, M. Švec, J. I. Martinez, P. Jelinek, P. Lacovig, M. Dalmiglio, S. Lizzit, P. Soukiassian, J. Cernicharo and J. A. Martin-Gago, *Nature Comm.*, 2014, **5**, 3054.

38. H. W. Jochims, E. Rühl, H. Baumgärtel, S. Tobita and S. Leach, *ApJ*, 1994, **420**, 307-317.

39. H. W. Jochims, H. Baumgärtel and S. Leach, *ApJ*, 1999, **512**, 500.

40. O. Berné and A. G. G. M. Tielens, *PNAS*, 2012, **109**, 401-406.

41. H. W. Kroto, J. R. Heath, S. C. O'Brien, R. F. Curl and R. E. Smalley, *Nature*, 1985, **318**, 162-163.

42. J. Cami, J. Bernard-Salas, E. Peeters and S. E. Malek, *Science*, 2010, **329**, 1180-1182.

43. K. Sellgren, M. W. Werner, J. G. Ingalls, J. D. T. Smith, T. M. Carleton and C. Joblin, *ApJ Lett.*, 2010, **722**, L54-L57.

44. K. Sellgren, M. W. Werner, J. G. Ingalls, J. D. T. Smith, T. M. Carleton and C. Joblin, in *PAHs and the Universe: A Symposium to Celebrate the 25th Anniversary of the PAH Hypothesis*, eds. C. Joblin and A. G. G. M. Tielens, E D P SCIENCES, 2011, vol. 46, pp. 209-214.

45. D. A. García-Hernández, A. Manchado, P. García-Lario, L. Stanghellini, E. Villaver, R. A. Shaw, R. Szczerba and J. V. Perea-Calderón, *ApJ Lett*, 2010, **724**, L39-L43.

46. D. A. García-Hernández, S. Iglesias-Groth, J. A. Acosta-Pulido, A. Manchado, P. García-Lario, L. Stanghellini, E. Villaver, R. A. Shaw and F. Cataldo, *ApJ Lett*, 2011, **737**, L30.

47. D. A. García-Hernández , N. K. Rao and D. L. Lambert, *ApJ*, 2011, **729**, 126.

48. Y. Zhang and S. Kwok, *ApJ*, 2011, **730**, 126.

49. R. H. Rubin, J. P. Simpson, C. R. O'Dell, I. A. McNabb, S. W. J. Colgan, S. Y. Zhuge, G. J. Ferland and S. A. Hidalgo, *MNRAS*, 2011, **410**, 1320-1348.

50. C. Gielen, J. Cami, J. Bouwman, E. Peeters and M. Min, *Astron. Astroph.*, 2011, **536**, A54.

51. C. Gielen, J. Bouwman, H. Van Winckel, T. L. Evans, P. M. Woods, F. Kemper, M. Marengo, M. Meixner, G. C. Sloan and A. G. G. M. Tielens, *Astron. Astroph.*, 2011, **533**, A99.

52. K. R. G. Roberts, K. T. Smith and P. J. Sarre, *MNRAS*, 2012, **421**, 3277-3285.

53. W. Krätschmer, L. D. Lamb, K. Fostiropoulos and D. R. Huffman, *Nature*, 1990, **347**, 354-358.

54. J. B. Howard, J. T. McKinnon, Y. Makarovsky, A. L. Lafleur and M. E. Johnson, *Nature*, 1991, **352**, 139-141.

55. R. E. Smalley, *Acc. Chem. Res.*, 1992, **25**, 98-105.

56. N. S. Goroff, *Acc. Chem. Res.*, 1996, **29**, 77-83.

57. S. Irle, G. S. Zheng, Z. Wang and K. Morokuma, *J. Phys. Chem. B*, 2006, **110**, 14531-14545.

58. E. R. Micelotta, A. P. Jones, J. Cami, E. Peeters, J. Bernard-Salas and G. Fanchini, *ApJ*, 2012, **761**, 35.

59. A. Chuvilin, U. Kaiser, E. Bichoutskaia, N. A. Besley and A. N. Khlobystov, *Nat. Chem.*, 2010, **2**, 450-453.

60. A. G. G. M. Tielens, *Rev. Mod. Phys.*, 2013, **85**, 1021-1081.

61. J. Zhen, P. Castellanos, D. M. Paardekooper, H. Linnartz and A. G. G. M. Tielens, *ApJ Lett.*, 2014, **797**, L30 - L34.

62. O. Berné, J. Montillaud and C. Joblin, *Astron. Astroph.*, 2015, **577**, A133-A141.

63. R. J. Trumpler, *Publ. Astron. Soc. Pac.*, 1930, **42**, 214-227.

64. G. Vidali, *Chem. Rev.*, 2013, **113**, 8762-8782.

65. B. T. Draine, *Annu. Rev. Astron. Astrophys.*, 2003, **41**, 241-289.

66. T. P. Stecher, *ApJ*, 1965, **142**, 1683-1684.

67. T. P. Stecher and B. Donn, *ApJ*, 1965, **142**, 1681-1682.

68. V. Mennella, L. Colangeli, E. Bussoletti, P. Palumbo and A. Rotundi, *ApJ*, 1998, **507**, L177-L180.

69. S. Wada, C. Kaito, S. Kimura, H. Ono and A. T. Tokunaga, *Astron. Astrophys.*, 1999, **345**, 259-264.

70. C. Joblin, A. Léger and P. Martin, *ApJ*, 1992, **393**, L79-L82.

71. T. Zecho, A. Güttler, X. W. Sha, B. Jackson and J. Küppers, *J. Chem. Phys.*, 2002, **117**, 8486-8492.

72. J. S. A. Perry, J. M. Gingell, K. A. Newson, J. To, N. Watanabe and S. D. Price, *Measurement Science & Technology*, 2002, **13**, 1414-1424.

73. S. C. Creighan, J. S. A. Perry and S. D. Price, *J. Chem. Phys.*, 2006, **124**, 114701.

74. V. Mennella, *ApJ Lett.*, 2008, **684**, L25-L28.

75. D. A. Williams and S. D. Taylor, *Q. J. R. Astr. Soc.*, 1996, **37**, 565-592.

76. F. Kemper, W. J. Vriend and A. Tielens, *ApJ*, 2004, **609**, 826-837.

77. N. J. Woolf and E. P. Ney, *ApJ*, 1969, **155**, L181.

78. L. B. F. M. Waters, F. J. Molster, T. de Jong, D. A. Beintema, C. Waelkens, A. C. A. Boogert, D. R. Boxhoorn, T. de Graauw, S. Drapatz, H. Feuchtgruber, R. Genzel, F. P. Helmich, A. M. Heras, R. Huygen, H. Izumiura, K. Justtanont, D. J. M. Kester, D. Kunze, F. Lahuis, H. J. G. L. M. Lamers, K. J. Leech, C. Loup, D. Lutz, P. W. Morris, S. D. Price, P. R. Roelfsema, A. Salama, S. G. Schaeidt, A. G. G. M. Tielens, N. R. Trams, E. A. Valentijn, B. Vandenbussche, M. E. van den Ancker, E. F. van Dishoeck, H. van Winckel, P. R. Wesselius and E. T. Young, *Astron. Astrophys.*, 1996, **315**, L361-L364.

79. C. Jäger, F. J. Molster, J. Dorschner, T. Henning, H. Mutschke and L. Waters, *Astron. Astrophys.*, 1998, **339**, 904-916.

80. L. B. F. M. Waters, C. Waelkens, H. van Winckel, F. J. Molster, A. G. G. M. Tielens, J. T. van Loon, P. W. Morris, J. Cami, J. Bouwman, A. de Koter, T. de Jong and T. de Graauw, *Nature*, 1998, **391**, 868-871.

81. T. Henning, *Annu. Rev. Astron. Astrophys.*, 2010, **48**, 21-46.

82. V. Pirronello, C. Liu, L. Y. Shen and G. Vidali, *ApJ Lett.*, 1997, **475**, L69-L72.

83. V. Pirronello, O. Biham, C. Liu, L. O. Shen and G. Vidali, *ApJ Lett.*, 1997, **483**, L131-L134.

2. Variation in the mass distribution of PAHs within astronomical objects

2.1 Background

The aromatic infrared bands (AIBs), astronomical emission features seen in the near- to mid-IR spectra of many astronomical objects, include peaks that fall at wavelengths of 3.3, 6.2, 7.6, 7.8, 8.6, 11.2 and 12.7 μm and are generally assigned to a class of molecules called polycyclic aromatic hydrocarbons (PAHs).[1] PAHs emit in the infrared *via* the mechanism outlined in Figure 2.1.

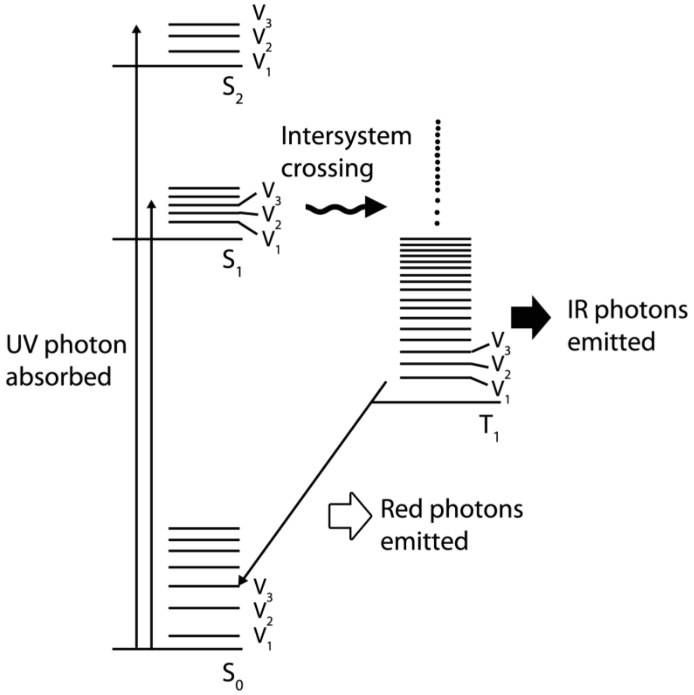

Figure 2.1. A Jablonski energy level diagram illustrating the emission mechanism of neutral PAHs.

Absorption of photons by interstellar PAHs can lead to the production of excited states in the molecule or to ionisation, among other effects, depending on the energy of the photon absorbed. The AIBs arise when a PAH molecule absorbs a UV photon, causing an excitation – an $S_1 \leftarrow S_0$ transition, for example. These excitations are followed by internal conversion to vibrationally excited states, which in turn can be followed by intersystem crossing to the triplet state, T_1. Relaxation through the vibrational levels causes IR fluorescence, giving rise to the emission features that can be so closely matched to the AIBs. Also interesting to note in this system is that relaxation to the ground state causes emission in the visible region.

Due to the fact that these astronomical emission features arise from a mixture of different PAH molecules, the positions and profiles of the peaks are sensitive to changes in many parameters, including the composition of the PAH population, the mass distribution, and electric charge. As such, there have been seen variations in the profiles and peak positions of individual emission features, both *between* and *within* astronomical objects.[2-6] Classification systems have been developed to distinguish between certain variations in the 3.3 μm feature – attributed to the aromatic C-H stretch,[2] and in the features belonging to the 6 – 9 μm region which are attributed to transitions involving C-C vibrational modes and are commonly assigned to PAH cations.[7] There are larger variations in the 6 – 9 μm region than in either the 3.3 μm or 11.2 μm features, *i.e.* in those attributed to C-H vibrational modes,[2] and variations in the ratio of the 6 – 9 μm region to either the 3.3 μm or 11.2 μm bands are often used as a reflection of the relative abundance of ionised PAHs within an object.

The 11.2 μm feature is one of the strongest and most recognisable of the AIBs. It arises from the out-of-plane (OOP) bending mode of C-H bonds of PAHs, specifically of solo hydrogen atoms – hydrogen atoms with no adjacent hydrogens on the same ring.[8] The profile of the 11.2 μm feature is very distinctive; it is asymmetric, with a steep blue edge and an extended red tail (Figure 2.2). The various profiles of the 11.2 μm feature that are seen from object to object have been grouped together and a classification system has been proposed to distinguish between objects that exhibit particular profile characteristics.[2] 'Class $A_{11.2}$' objects have, in general, lower peak wavelengths, in the range 11.20 – 11.24 μm, in addition to a short red tail. 'Class $B_{11.2}$' objects have a higher peak wavelength – 11.25 μm – and tend to have a more extended red tail. These appear less asymmetric as a result, and are also less commonly seen than Class $A_{11.2}$ objects. A third class, 'Class $C_{11.2}$', of which there are only a small number of examples, characteristically have longer peak wavelengths making the band almost symmetric. Objects that exhibit short peak wavelengths and extended red tails are classified as $A(B)_{11.2}$.

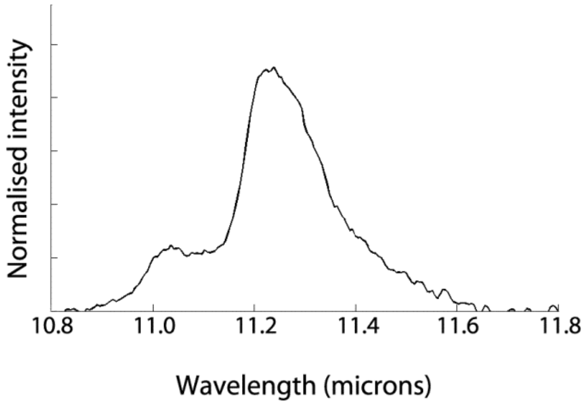

Figure 2.2. Example of the profile of the 11.2 μm feature. The data shown here was obtained using the MICHELLE instrument at the United Kingdom Infrared Telescope, from the Red Rectangle nebula, and is discussed in Section 2.4.

Concerning the origin of the observed profile variations of the 11.2 μm feature, discussions are ongoing. The variation in the peak position has been interpreted in terms of its dependence on the temperature of the exciting star.[9] The red wing of the 11.2 μm feature has been proposed to arise from anharmonic effects, although it was noted by van Diedenhoven *et al*. that this is likely not the sole factor involved.[2] It has also been suggested that contributions to the feature's red tail are made by the OOP bend mode of duo hydrogens on the periphery of cationic PAHs,[8, 10] or, in studies that found a contribution to the red tail from species that exist far from the exciting star, from so-called Very Small Grains (VSGs).[3, 4, 11] Recently, Candian & Sarre proposed a dependence of the profile of the 11.2 μm feature on the mass distribution of the PAH carriers.[12] They suggested that the steep blue edge of the feature is a result of the peak wavelength of the solo C-H OOP mode reaching an asymptotic value with increase in PAH mass, and that smaller PAHs contribute to the red tail. In addition, they used an emission model to fit the spectra of three objects and found that Class $A_{11.2}$ type profiles correspond with a higher proportion of high-mass PAHs – resulting in a shorter wavelength peak and steep blue side – whereas Class $B_{11.2}$ type profiles are suggestive of a PAH mass distribution that contains a larger proportion of lower mass PAHs – contributing to a longer peak wavelength and a more extended red tail.

Shannon *et al.*[13] investigated the 11.2 μm feature of three objects, and have evaluated the contributing species in terms of a five-component Gaussian decomposition. They found that the 11.0 μm peak that often accompanies the 11.2 μm feature, and is commonly attributed to PAH cations, contains a contribution from neutral PAHs, in support of the theory by Candian and Sarre that neutral acenes may be responsible for this feature.[12] Within the 11.2 μm feature itself, three contributing components were stipulated by the authors:[13] One strong band was found to carry most of the 11.2 μm emission, whereas another, smaller, broader component was responsible for the red wing of the feature, and a final small and narrow component was deduced to arise at 11.20 μm. This final component was assigned by the authors to PAH cations, and was considered to be responsible for a small feature at 11.20 μm that can be seen on top of the usual 11.2 μm profile in some instances. It was proposed that the fraction of PAH cations to neutrals, dictating this component's 11.0/11.2 relative intensity, could have an influence on the peak position of the overall 11.2 μm peak along with the influence of varying mass distribution as reported by Candian and Sarre.[12]

This Chapter details a theoretical investigation into the variation in the 11.2 μm AIB *within* astronomical objects, as a function of distance from the exciting star. This was carried out with particular focus on the influence of PAH mass distribution on the 11.2 μm feature profile. Two objects were examined, the reflection nebula NGC 7023 (Section 2.3), and the Red Rectangle nebula (Section 2.4); both of these objects exhibit changes in their mid-IR emission spectra, depending on the positions within the nebulae that are being observed. An emission model, developed and reported by Candian,[12, 14] was used to calculate the 11.2 μm emission features of four PAHs, shown in Figure 2.3, and these were used to fit spectra taken at varying offsets within NGC 7023 and the Red Rectangle. The results of the emission model were used to obtain a ratio of the relative proportion of low-mass (number of carbon atoms (N_C) < 50) PAHs to the proportion of high-mass (N_C > 50) PAHs for each spectrum. This was used as an indicator of the mass distribution of PAHs at each position within the nebulae, hence linking the profile variations of the 11.2 μm feature with PAH mass distribution. In addition, the PAH mass distribution within each of the objects, specifically its variation with offset from the exciting star in each case, was analysed and compared with the results of previous studies,[6, 15, 16] in order to gain an overall picture of the evolution of the PAH population within these environments.

2.2 Theoretical approach

An emission model was used to investigate profile variation in the 11.2 μm feature with specific focus on the effect of the mass distribution of PAHs. This emission model, reported by Candian,[12, 14] is based on the Density Functional Theory (DFT)-calculated vibrational frequencies and intensities of four selected PAHs (Figure 2.3). DFT predicts the vibrational frequencies of a molecule, following the evaluation of its optimised geometry, by calculating the second derivative of the total energy at various displacements from the optimal geometry. The emission model calculates the emission from each PAH following the absorption of UV photons, taking into account the stellar spectral energy distribution (SED) of the object being studied. It important to note that using the four PAHs depicted in Figure 2.3 does not imply identification of these particular molecules in space; instead, the emphasis is on the fact that the 11.2 μm emission feature can be fitted well using neutral, solo-containing PAHs of this size range.

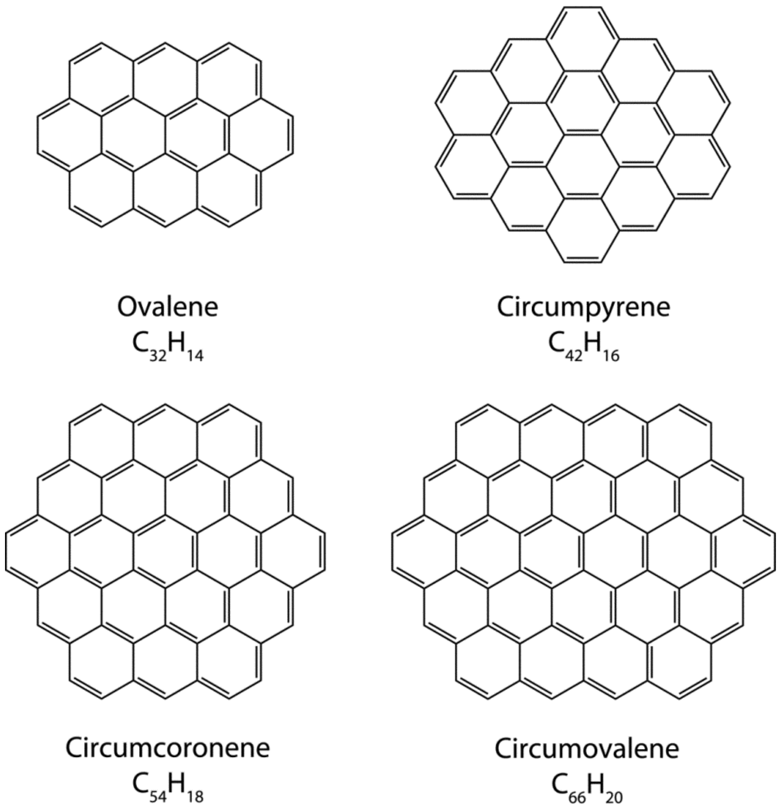

Figure 2.3. Structures of the four PAHs used in the emission model for this investigation. For the purposes of this study, ovalene and circumpyrene represent ‘low-mass’ PAHs ($N_C < 50$) and circumcoronene and circumovalene represent ‘high-mass’ PAHs ($N_C > 50$).

A brief description of the emission model utilised in this Chapter is given below. For a more in-depth discussion, see Candian (2011).[14]

The model is based on the thermal approximation, as described by Léger *et al.*,[17] and as employed by Pathak & Rastogi,[18] as an example. Within the thermal approximation, a PAH molecule is treated as a heat bath with a temperature T_p and average molecular energy of U. Following absorption of a UV photon, a PAH is excited to an internal energy of $U(T)$. In the harmonic approximation, the potential energy well of a system is described by a parabola and the vibrational levels within are evenly spaced. This works well at lower energies but breaks down at higher energies where the spacing between vibrational states decreases. Within the harmonic approximation, $U(T)$ can be expressed in terms of T_p using the following equation:

$$U(T) = \sum_{i=1}^{n} \frac{hc\omega_i}{\exp\left(hc\omega_i / k_B T_p\right) - 1}$$

where *U(T)* is the internal energy of the PAH in eV, *n* is the total number of vibrational modes of the molecule, and *i* is the number of the vibrational modes with frequency ω_i, calculated using DFT.[12] Values of T_p can range from 100 – 1200 K, depending on the energy of the absorbed photon (between 0 and 10 eV) and the size of the molecule (between 32 and 96 C atoms). Following photon absorption, the PAH cools through its vibrational modes, *via* a radiative cascade. The rate of emission, ϕ_i, for each vibrational mode *i* is calculated using the following:

$$\phi_i = \frac{A_i^{1,0}}{\exp(hc\omega_i / k_B T_p) - 1}$$

where the Einstein coefficient $A_i^{1,0}$ can be calculated using the DFT transition intensities.[19] The energy emitted for each vibrational transition is then calculated. The equation for the energy emitted in the *i*th mode – for a change in the internal energy of the molecule, δU, that corresponds with a drop in *T* of 1 K is given below:

$$\delta E_i(T) = \frac{\phi_i \times \omega_i}{\sum_{i=1}^{m} \phi_i \times \omega_i} \times \delta U(T)$$

The sum of the emitted energies for each vibrational transition at each temperature in steps of 1 K, from T_p to 50 K, is then calculated, and is weighted against the probability of photo-ionisation of the PAH and the rate of photon absorption, R_{abs}, which can be calculated using the following equation:

$$R_{abs} = \int_0^{13.6} \frac{B_\nu^d \sigma_\nu}{h\nu} \mathrm{d}\nu$$

in which ν is the frequency of the absorbed photon, with 13.6 eV as the high-energy maximum as photons of a higher energy would not be expected. The term σ_ν represents the photo-absorption coefficient of the PAH molecule, and is taken from the French-Italian database.[20] A diluted Planck function, B_ν^d represents the excitation source, and depends on the physical conditions in the object.

To obtain a fit to the astronomical 11.2 μm feature data, the sum of the calculated emission for all four PAHs is taken and a χ^2-minimisation routine is employed. The only variable within the χ^2-minimisation is the relative proportion of each of the PAHs contributing to the fit, and once the best fit to the astronomical data has been evaluated, numerical values of the relative contribution of each PAH are obtained. These values are used as an indicator of the size distribution of PAHs contributing to the 11.2 μm feature by taking the sum of the relative proportions of the two 'low-mass' PAHs – ovalene ($C_{32}H_{14}$) and circumpyrene ($C_{42}H_{16}$) (Figure 2.3), and the sum of the proportions of the two 'high-mass' PAHs – circumcoronene ($C_{54}H_{18}$) and circumovalene ($C_{66}H_{20}$), and calculating a ratio of the proportion of 'low-mass' PAHs to 'high-mass' PAHs.

Fits using a χ^2-minimisation can be affected by noise in observational data, impacting on the accuracy of the fit. The χ^2-minimisation technique is, however, commonly used to fit astronomical data, and for the purpose of the studies outlined in this Chapter, very noisy data are excluded (Sections 2.4.1 and 2.4.2).

In this investigation, the variation in the ratio of the proportion of low-mass to high-mass PAHs at each offset within the two objects studied, NGC 7023 and the Red Rectangle, was used as an indicator for the overall mass distribution of PAHs within each of these objects. How the mass distribution changes as a function of distance from the main star in these objects was investigated, and the results of this and corresponding discussions are given in Sections 2.3 and 2.4.

2.3 NGC 7023

NGC 7023 is a reflection nebula (RN) irradiated by the star HD 200775, around which are located three photodissociation regions (PDRs) to the star's

East, South, and North West. PDRs are areas between UV-rich regions and molecular clouds, and characteristically have a varying radiation environment *i.e.* the UV flux of the exciting star decreases in intensity on moving further from the star and into the molecular cloud. As such, variations in the 'PAH' spectra obtained from PDRs can be observed as a result of the changing nature of emitting species with change in the local environment. The North West PDR of NGC 7023 (NGC-7023-NW) is the brightest of the three PDRs and has been studied extensively.[11, 16, 21-23] Figure 2.4 shows a Hubble Space Telescope (HST) image of NGC-7023-NW in which the star, HD 200775, is located at the bottom left corner, there is a bright diagonal edge, showing the boundary between the dense molecular cloud and the PDR, and a young stellar object (YSO) in the top right corner.[6]

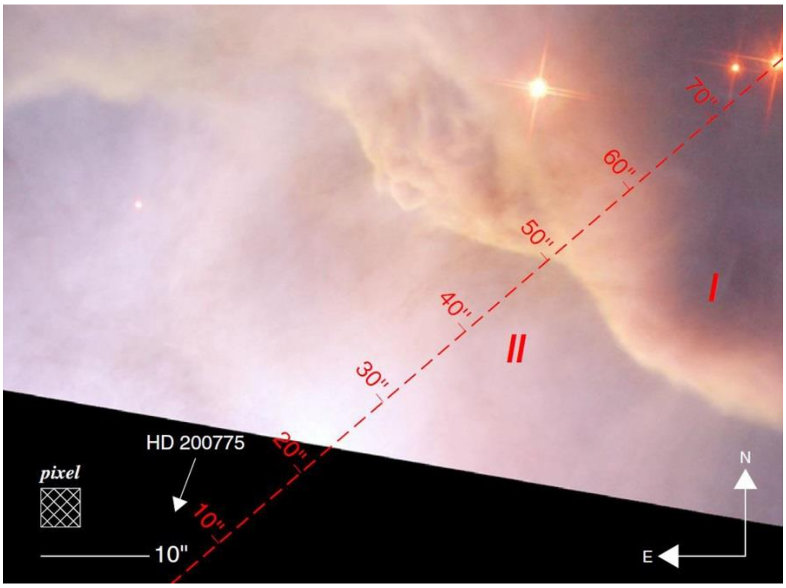

Figure 2.4. HST image of NGC-7023-NW adapted from Boersma (2013).[6] The dashed red line shows the line along which *Spitzer* spectra were obtained at various intervals, with distances in arcsec from HD 200775 labelled.

NGC-7023-NW is known to exhibit spectral IR emission variation with distance from HD 200775.[24] Berné *et al.* (2007)[3] and Rosenberg *et al.* (2011)[4] investigated this variation, applying a Blind Signal Separation (BSS) technique to mid-IR data recorded by the *Spitzer* Space Telescope,[25] and found three main spectral components which were assigned to three separate classes of carrier: PAH cations (PAH^+) – found to dominate spectra closest to the star; neutral PAHs – found slightly further from the star; and so-called Very Small

Grains (VSGs) which were found to be the main component furthest from the star towards the molecular cloud. Boersma *et al.*[6] analysed the spectra using a fitting model based on calculated IR spectra of PAHs available in the NASA Ames PAH IR Spectroscopic Database (www.astrochem.org/pahdb),[26] aiming to achieve a picture of the changing PAH population in terms of size, charge and composition. Their results concerning PAH size showed a reduction in the size of PAHs with increased distance from the star. At positions towards the dense medium (marked as *I* in Figure 2.4), at about 50” from the star, the authors noted that there is a “sudden swap from large to small PAHs dominating the emission”. This increase in the proportion of small PAHs was attributed to smaller PAHs being more highly vibrationally excited than larger PAHs, within the same radiation field, and to the fact that at these positions the radiation field is less intense, so the small PAHs are not destroyed. They also commented that there is a population of smaller PAHs close to the star, which was attributed to fragmentation and dehydrogenation of larger PAHs due to the high intensity of the radiation field. At this position, close to the star, larger, irregular PAHs may also exist that are not represented within the results due to their absence from the PAH database.[6]

Recently, Croiset *et al*. analysed spectra of NGC 7023 obtained by the Stratospheric Observatory for Infrared Astronomy (SOFIA). They used a ratio of the intensity of the 11.2 μm feature ($I_{11.2}$) to that of the 3.3 μm feature ($I_{3.3}$) as a tracer of PAH size within NGC 7023 and concluded, in agreement with the work of Boersma *et al.*, that smaller PAHs are more abundant further out from the star, and that closer in only larger PAHs survive the increased radiation field.[16]

In this investigation, the emission model described in Section 2.2 was used to fit the data reported by Boersma *et al.*[6] to describe the evolution of the PAH population with distance from the star, in terms of the proportion of low-mass ($N_C < 50$) to high-mass ($N_C > 50$) solo-hydrogen-containing PAHs. An important distinction between this investigation and those carried out previously is that this model fits data using only neutral solo-H-containing PAHs, whereas fitting models that include any calculated PAH within a database will usually yield a high proportion of PAH anions, which are likely to be over-represented due to their red-shifted wavelengths which are used to fit the extended red tail of the 11.2 μm feature. Significantly, the model utilised in this study calculates the *emission* of the included PAHs, in contrast to fitting models based on calculated *absorption* spectra, to which an approximate redshift, usually 15 cm^{-1}, must be applied for 'conversion' to emission. The results presented here produce a picture of the size distribution of PAHs within NGC-7023-NW, using the four PAHs depicted in Figure 2.3, which can then compared with the results described by Boersma *et al.*.[6]

2.3.1 The data set

Figure 2.5 presents data in the range 10.8 – 11.7 μm for various offsets from HD 200775 through the PDR to the dense molecular cloud (along the dashed line in Figure 2.4).[†] The data are from the *Spitzer* Infrared Spectrograph (IRS) short-wavelength-high-resolution (SH) spectral map of NGC-7023-NW, which has been normalised and is presented by Boersma *et al.* in their Figure 3.[6]

It can be seen from Figure 2.5 that with increasing distance from the star, the maximum of the 11.2 μm feature shifts to longer wavelengths; close to the star it peaks at 11.20 μm, whereas at the furthest distances the peak wavelength falls to ~ 11.24 μm. Between offsets of ~ 20" and ~ 45", a narrow feature can be seen at 11.20 μm, which is not seen at larger offsets, and which has been assigned to cationic PAHs by Shannon *et al.*[13] In addition, the intensity of the feature seen at 11.0 μm decreases on moving further from the star. According to the results of Boersma *et al.*, these trends correspond with an overall decrease in the size of PAHs with increased distance from the star.[6]

[†] Grateful acknowledgement is given to Christiaan Boersma for providing the data set for this investigation.

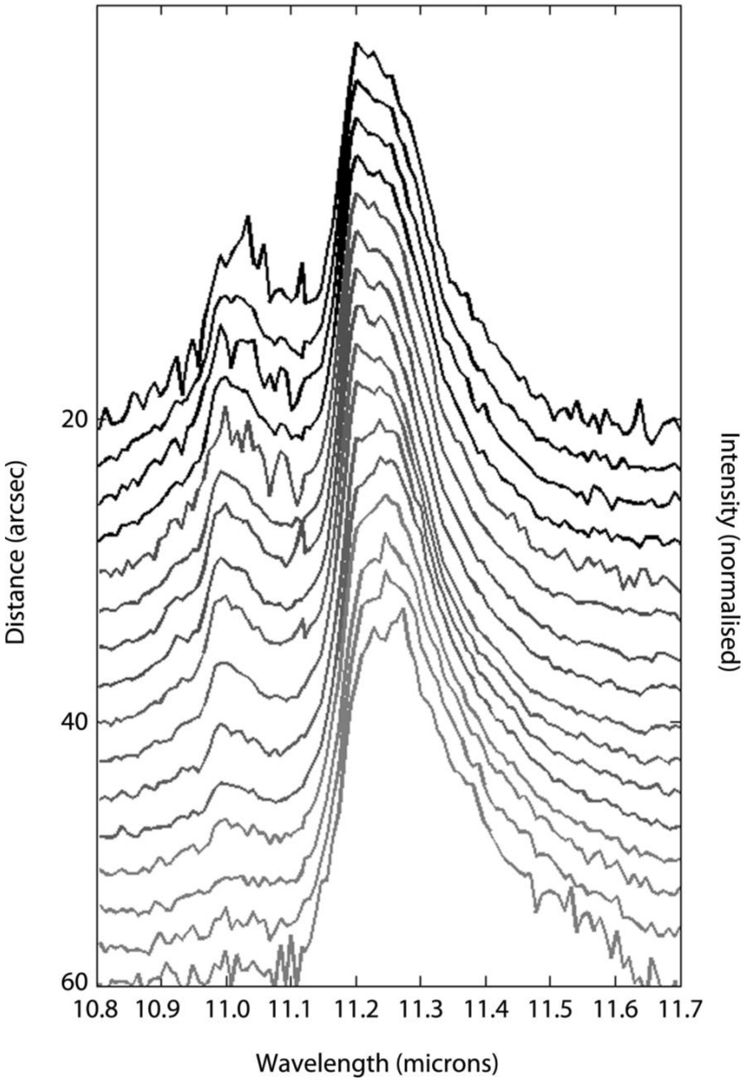

Figure 2.5. *Spitzer*-IRS SH spectra showing the 11.2 μm feature at different offsets from HD 200775 within NGC-7023-NW. Figure adapted from Boersma (2013).[6]

2.3.2 Emission modelling results

Figure 2.6 and Figure 2.7 show the results of the emission model fitting to the data given in Figure 2.5. The 11.0 μm feature is not included in the fitting process. In general, good agreement is seen between the model and the data. However, it can be seen that from 47.0" to larger offsets, the closeness of the fit to the red tail of the feature begins to decrease. It has been suggested that the red tail component of the 11.2 μm feature may arise from small PAHs,[12] PAH anions, VSGs and/or PAH clusters, or hydrogenated PAHs[27] – all of which can be expected to be present at these distances – further out from the exciting star and into the dense medium – where the reduced radiation field would suggest a greater likelihood of species of this nature surviving. If it is the case that one, or more, of these carriers were responsible for the red tail of this feature within NGC 7023, then the reason that the fit is not as close in certain spectra could simply be because the emission model does not include species of this kind.

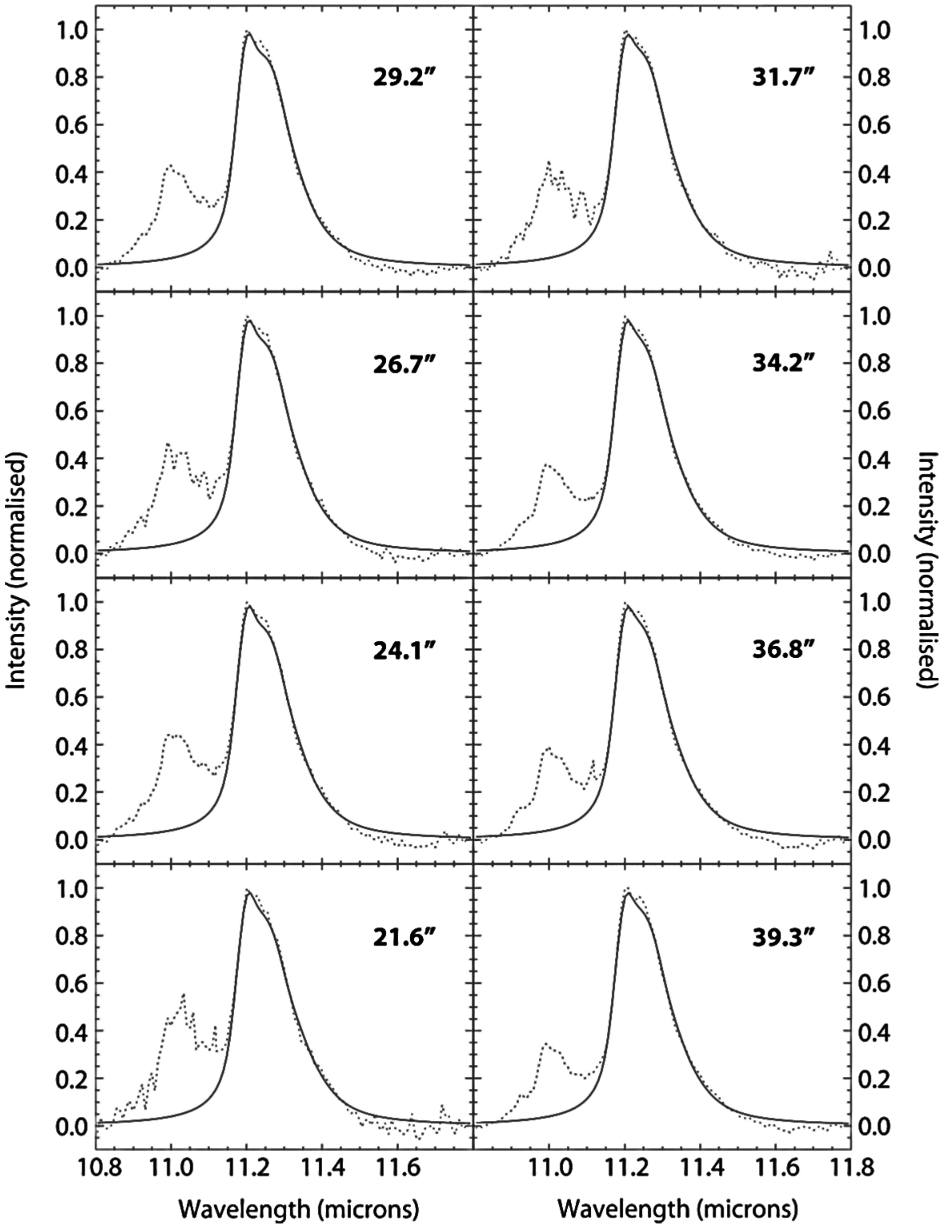

Figure 2.6. Spectra taken at intervals moving away from the star HD 200775 in NGC 7023 (dotted line) with the fit (solid line) resulting from the emission model. Spectra shown are at offsets in the range 21.6” – 39.3”, and the fitted data is continued in Figure 2.7.

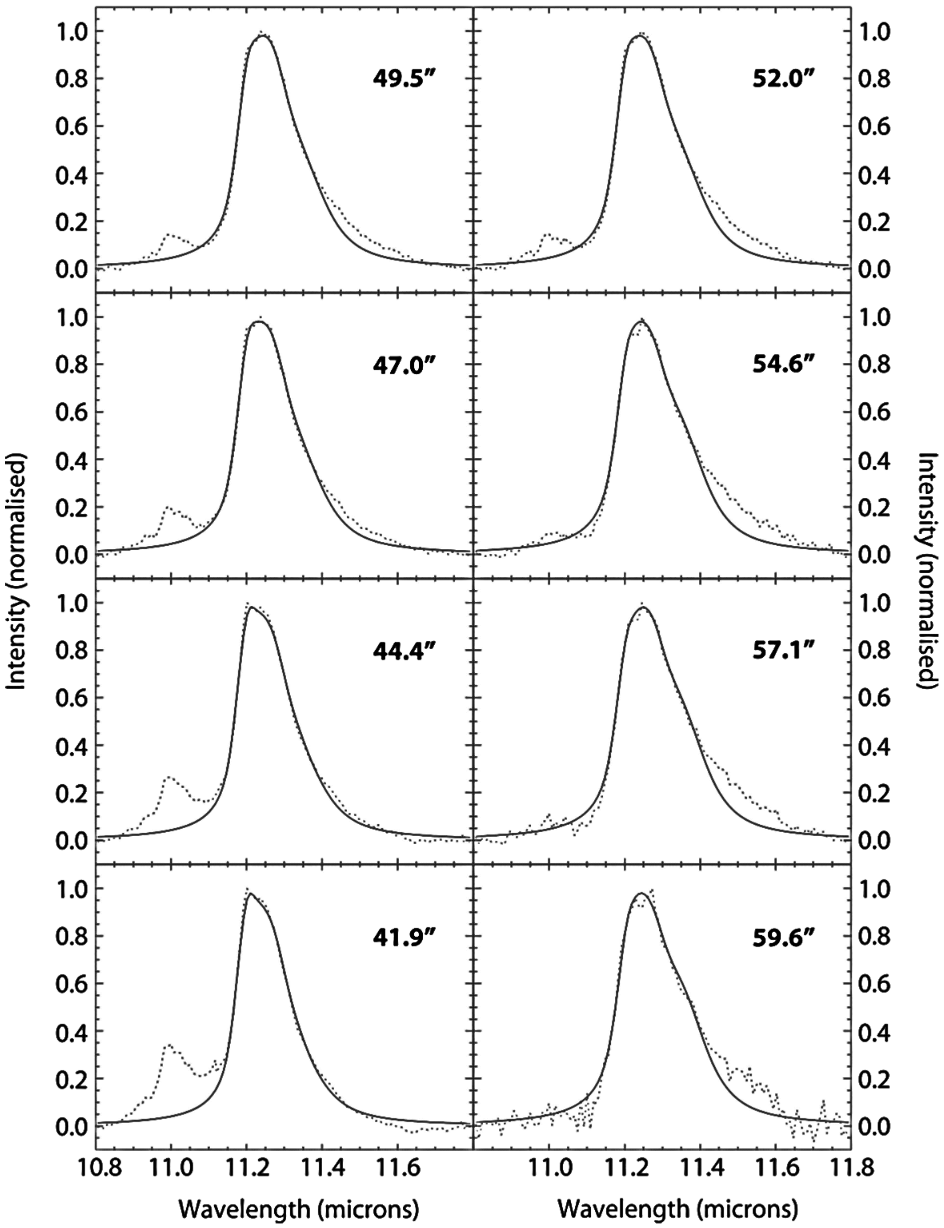

Figure 2.7. *Continued from Figure 2.6.* Spectra taken at intervals moving away from the star HD 200775 in NGC 7023 (dotted line) with the fit (solid line) resulting from the emission model. Spectra shown are at offsets in the range 41.9” – 59.6”.

The ratio of low-mass ($N_C < 50$) to high-mass ($N_C > 50$) solo-containing PAHs for each offset within NGC-7023-NW was obtained using the values of relative contribution of each of the four PAHs (Figure 2.3) to the overall fit using the emission model with the abundances as free parameters. These ratio values are presented in Table 2.1 and Figure 2.8. Included also in Table 2.1, and shown in Figure 2.9, are the relative contributions of low-mass ($N_C < 50$)

and high-mass ($N_C > 50$) PAHs to the overall fit, expressed as percentages. It can be seen that there is an overall increase in the ratio of low-mass PAHs to high-mass PAHs, with a concomitant increase in the proportion of low-mass PAHs, or a decrease in the proportion of high-mass PAHs, with increasing distance from the star. This is also indicated in Figure 2.9, in which it can be seen that the percentage contribution of low-mass ($N_C < 50$) PAHs to the overall fit increases with offset.

Table 2.1. Ratio of low-mass to high-mass PAHs, and percentage contributions of low-mass and high-mass PAHs, at each offset along the dashed line in Figure 2.4 in NGC-7023-NW.

Offset (arcsec)	Ratio of PAHs (small : large)	% contribution to fit ($N_C < 50$)	% contribution to fit ($N_C > 50$)
21.6	1.53:1	61	39
24.1	1.56:1	61	39
27.6	1.56:1	61	39
29.1	1.58:1	61	39
31.7	1.48:1	60	40
34.2	1.40:1	58	42
36.8	1.39:1	58	42
39.3	1.48:1	60	40
41.9	1.42:1	59	41
44.4	1.65:1	62	38
47.0	1.91:1	66	34
49.5	2.20:1	69	31
52.0	2.16:1	68	32
54.6	2.41:1	71	29
57.1	2.68:1	73	27
59.6	2.51:1	72	28

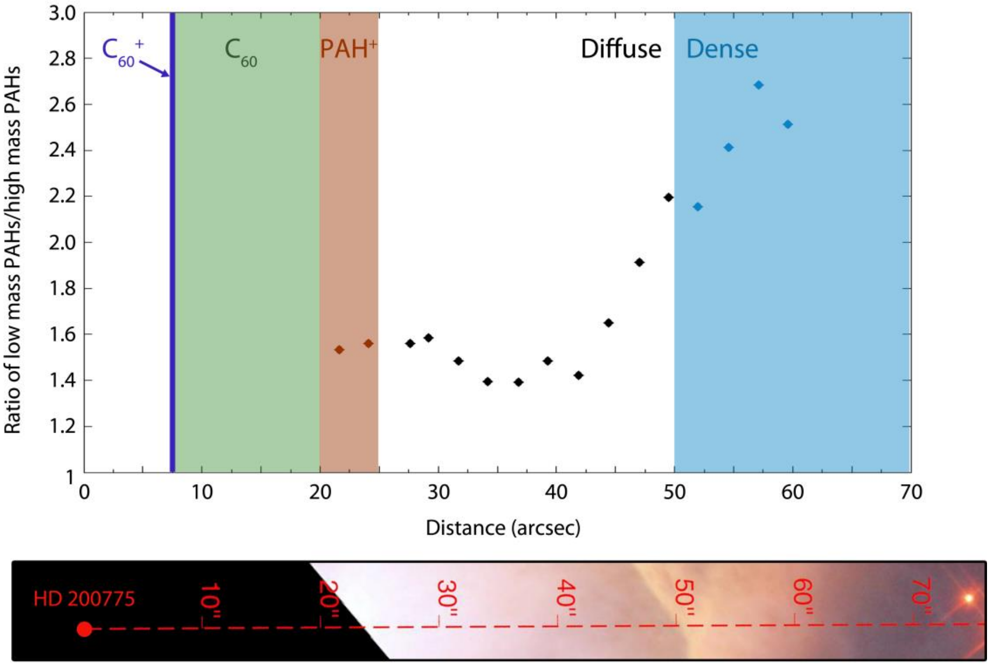

Figure 2.8. The ratio of low-mass PAHs to high-mass PAHs for each offset within NGC-7023-NW. For reference, included is a section of the HST image shown in full in Figure 2.4, with the dashed line marking various offsets, and also showing features such as the PDR-dense medium interface (~ 50”). Marked on the plot are the distances at which are detected C_{60}^{+} (dark blue), C_{60} (green), and PAH cations (red), along with the areas attributed to the diffuse (white) and dense (light blue) medium.

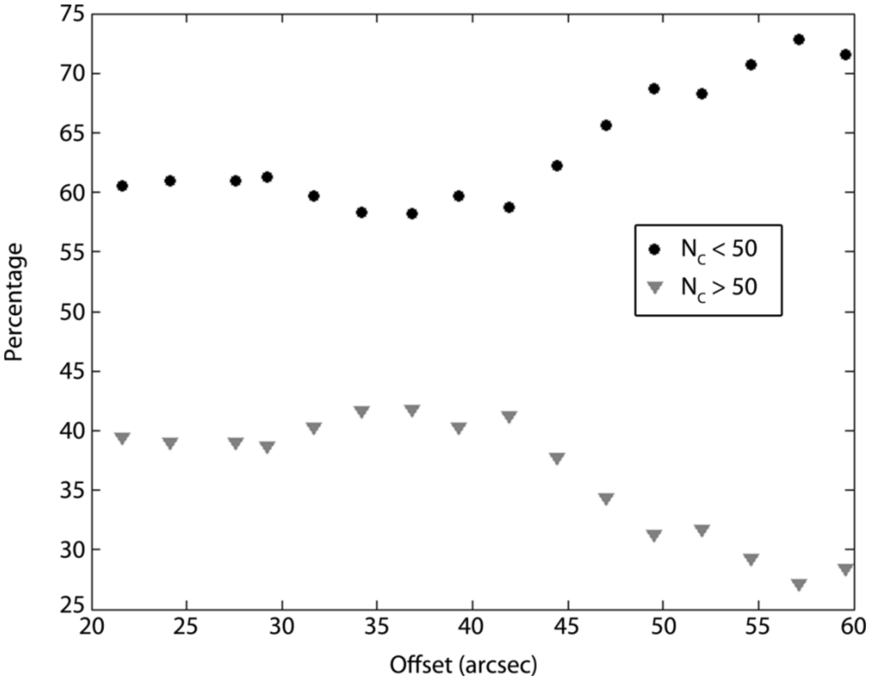

Figure 2.9. Percentage contributions of low-mass ($N_C < 50$) and high-mass ($N_C > 50$) PAHs to the overall fit of the 11.2 μm feature at each offset within NGC-7023-NW.

Figure 2.8 contains additional detail pertaining to the varying conditions within NGC-7023-NW and to previous detections that have been made. These, along with the results of the emission model, may be used to paint an overall picture of the evolving PAH population with increasing distance from HD 200775, which in turn can be compared with the results of earlier studies (discussed in Section 2.3).

Close to the exciting star, at a distance of 7.5”, emission features have been detected that are attributed to C_{60},[28, 29] and to C_{60}^{+}.[30] While C_{60}^{+} is only detected at this distance, emission features of C_{60} are seen to extend further out away from the star. This supports the assignment of C_{60}^{+} - as a result of photoionisation of C_{60} – and suggests that its existence is linked with the strong radiation field at such close proximity to the exciting star.

Within 20” of HD 200775, spectral features due to PAHs diminish, compared with those seen further from the star, and the emission peaks attributed to C_{60} are observed.[28, 29] This observation has been used as the basis for a proposed mechanism of formation of C_{60}, which invokes dehydrogenated PAHs as the precursors to fullerene formation through a top-down mechanism.[31] The foundation of this mechanism is that the strength of the radiation field in this region is so high that most PAHs undergo fragmentation or dehydrogenation, and that the abundance of PAHs decreases close to the star, with a corresponding increase in the abundance of C_{60}, suggesting a dependence of one on the other. Further discussion on the formation of fullerenes from PAHs is given in Chapter 3 of this Thesis.

Between 20 and 30”, it can be seen in Figure 2.8 that the ratio of low-mass PAHs to high-mass PAHs is slightly higher than for the region between ~ 30 and ~ 45”, suggesting a higher proportion of smaller PAHs. It is suggested by Boersma *et al.* that the spectra in the region within 25” of the star are dominated by PAH cations,[6] as is indicated on the plot in Figure 2.8. As the 11.2 μm feature is attributed to neutral PAHs, the ratios obtained for this region (*i.e.* the two points enclosed in the red region of the plot in Figure 2.8) may not be entirely representative of the overall PAH population. However, it is noted by Boersma *et al*. that in regions close to the star the radiation field would be such that larger PAHs could be dehydrogenated and would fragment to form smaller, more irregular PAHs,[6] and so the results of the emission model appear to reflect this behaviour.

In the general diffuse medium, from ~ 35” to 50”, which includes the boundary between the diffuse and dense medium, the emission model results show a gradual increase in the proportion of low-mass PAHs with increasing distance (Figure 2.8). Within this area and up to ~ 45” offset, the 11.2 μm peak exhibits a narrow feature at 11.20 μm, as seen in Figure 2.5. This feature has been assigned to PAH cations;[13] however, it has been reported that the solo OOP bend emission of large PAHs reaches an asymptotic value with increasing size, this value being reached at a PAH size of $C_{48}H_{18}$.[12] It can be postulated, therefore, that a population containing many PAHs of this size or larger would have the effect of contributing to this asymptote, which may result in the appearance of a ‘separate’ feature at 11.20 μm. The fact that this feature occurs in spectra within the region where the proportion of low-mass PAHs is lower – according to the emission model results presented here, supports the idea that it could arise from the building up of the solo OOP bend mode of high-mass PAHs.

The proportion of low-mass PAHs increases further on reaching distances within the dense molecular cloud (50” onwards). Regarding this dense region, Boersma *et al*. note a switch in domination of the emission spectra from large to small PAHs, and comment that within this shielded medium the radiation field is not strong enough to destroy the smaller molecules.[6]

The results of fitting the data in this Section using the emission model can be used to bring together the following overall picture of PAH size within NGC-7023-NW. Furthest from HD 200775, in the dense molecular cloud (60” – 50”), there resides the highest relative proportion of low-mass PAHs, which are able to exist due to the shielded environment, provided by the dense material, and reduced radiation field. In this region there may also be PAH clusters, VSG-type structures or hydrogenated PAHs which, on moving closer to the star, would be destroyed or photoevaporated to form neutral PAHs. Closing in on the star (~ 50” – 35”), the proportion of low-mass PAHs gradually decreases, reflecting the increasing radiation field which would prevent their existence and result in a larger relative proportion of high-mass PAHs. Closer still (~ 35” – 20”), the proportion of low-mass PAHs increases slightly, probably resulting from the fragmentation of large PAHs due to the increased radiation field. Here PAHs are expected to be ionised and are likely dehydrogenated. Within 20” of the star C_{60} is detected, which is a much more stable molecule in the harsh radiation field in this region, due to its lack of chemically reactive edges. Finally, upon reaching a distance of 7.5”, C_{60} is ionised, and hence emission features of C_{60}^+ are seen.

This picture of the size distribution of PAHs within NGC-7023-NW, obtained through the use of the emission model described earlier, is in broad agreement with the results of Boersma *et al.*,[6] obtained through the use of the NASA Ames PAH database, and those of Croiset *et al.*,[16] achieved using the $I_{11.2}/I_{3.3}$ ratio as a PAH size indicator. The agreement with two studies that employ very different approaches provides support that the model used within this Chapter is a valuable molecule-specific method for fitting the 11.2 μm of astronomical spectra in terms of four, representative, solo-containing neutral PAHs.

It should be noted that obtaining any values of uncertainty or error to apply to the output of this emission model is very difficult, and as such the degree to which the results can be interpreted is unclear. In the absence of values of uncertainty, a user can get a ‘feel’ of the data by altering a chosen parameter within a computational model, and noting how the output changes as a result. If the results of the model are very sensitive to changes in particular parameters, *i.e.* they exhibit large variations with varying parameters, then it may be assumed that the results obtained can be associated with a relatively high uncertainty, due to their dependence on some aspects of the model. Future use of this emission model beyond the work described in this Thesis would therefore benefit from a systematic investigation into the sensitivity of results, to place any obtained output into a context of relative certainty or uncertainty.

2.4 The Red Rectangle

The Red Rectangle (also called HD 44179) is a highly unusual and interesting object. It was discovered in 1975,[32] and consists of a binary star system at the centre of, and ejecting matter into, a biconical nebula that appears as an X-shape (Figure 2.10). The Red Rectangle is an object of so-called mixed chemistry, meaning that both oxygen-rich and carbon-rich molecules have been detected within the object. There is an oxygen-rich circumbinary disk surrounding the binary system, in which have been detected emission features that are assigned to crystalline silicates, such as olivines, and an absorption feature due to CO_2.[33] In the extended nebula, some of the strongest examples of the AIBs are detected, which are attributed to the presence of PAHs and indicate the carbon-rich nature of the nebula.[34, 35]

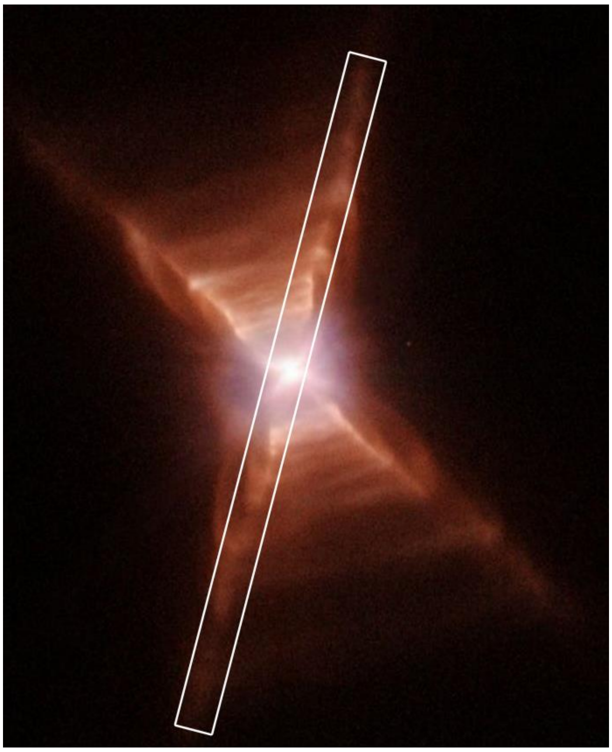

Figure 2.10. Hubble Space Telescope (HST) image of the Red Rectangle nebula.[36] The white box shows the North West and South East whiskers of the bicone structure, along which spectra have been recorded.

More recently, Hubble Space Telescope (HST) imaging of the Red Rectangle has revealed a greater level of structural detail, including a 'ladder structure' along the bicone, that may suggest pulses of ejected material.[36] The unique shape of the Red Rectangle allows observations to be carried out that give insight into the evolution and spatial distribution of material within the nebula. For example, the edges, or 'whiskers', of the bicone provide a line-of-sight along which spectral observations can be taken as a function of offset, to investigate any variation in the shape, position or intensity of features, and hence investigate the changing populations of the features' carriers.

One example of an investigation of this nature is a study that was carried out to probe the variation in profile of the 3.3 μm aromatic C-H stretch feature with increasing offset from the star.[37] Results of this study revealed the presence of two components contributing to the overall peak, at 3.30 μm and 3.28 μm. It was seen that at the on-star position the 3.30 μm component was dominant and the 3.28 μm component was not present. The relative intensity of the 3.28 μm component increased with offset along the North West whisker of the nebula. In a separate investigation, through comparison of experimental laboratory data, computational calculations and emission modelling, an explanation was found for the two components in the edge structures of PAHs.[15] So-called 'bay' hydrogens (Figure 2.11) were seen to have C-H stretching modes that fall at slightly shorter wavelengths than for non-bay hydrogens, and results of emission modelling revealed that the change in profile of the 3.3 μm feature with offset can be explained in terms of an increasing ratio of bay to non-bay hydrogens. It was argued in the same work that the formation of bay-type positions could be achieved by the addition of rings to a PAH structure, and as such an increase in the proportion of bay hydrogens would be associated with the growth of PAH molecules.

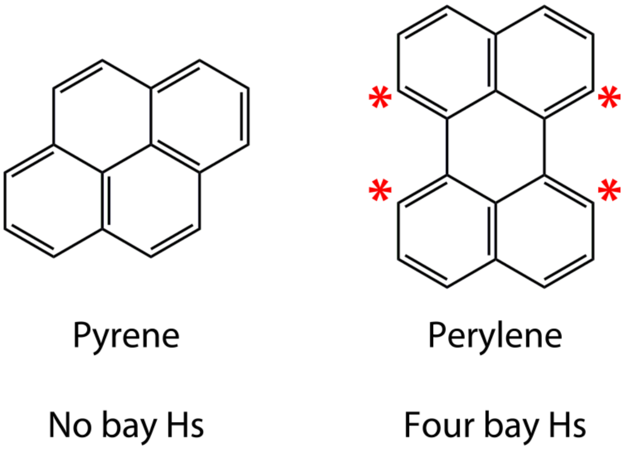

Figure 2.11. Structures of pyrene and perylene. Pyrene contains no bay hydrogen positions whereas perylene contains four; these are indicated by red asterisks.

Following this inferred growth in size of PAHs within the Red Rectangle, *i.e.* an increase with increasing offset, the emission model described in Section 2.2, and utilised in Section 2.3, was used to investigate the changing profile of the 11.2 μm feature within the Red Rectangle; the focus is on the associated change in ratio of low-mass to high-mass PAH molecules. The model was used to fit data obtained using the MICHELLE instrument at the United Kingdom Infrared Telescope (UKIRT), and first reported by Topalovic (2006).[38]

2.4.1 The data set

Figure 2.12 and Figure 2.13 show the data obtained from the observations of the Red Rectangle, focussing specifically on the 11.2 μm solo C-H OOP bend feature and taken at various offsets moving along the North West and South East whiskers of the bicone structure (Figure 2.10). Data taken between the on-star position and the 2.28” offset have not been included due to contamination of the spectrum by a silicate feature at 11.27 μm arising in the circumbinary disk.[39] It can be seen in Figure 2.12 and Figure 2.13 that as the offset increases, the 11.2 μm feature decreases in intensity, and from 4.94” onwards the signal-to-noise ratio decreases significantly. Inspection of Figure 2.12 and Figure 2.13 also appears to show very little variation in peak wavelength with increased offset, as indicated by the blue lines which run approximately through the peak maximum of each spectrum. Despite the lack of variation in the peak positions of the feature, increased symmetry of the peak can be seen with increased offset, which would be caused by either a decrease in the gradient of the steep blue edge or an increase in the gradient of the red tail.

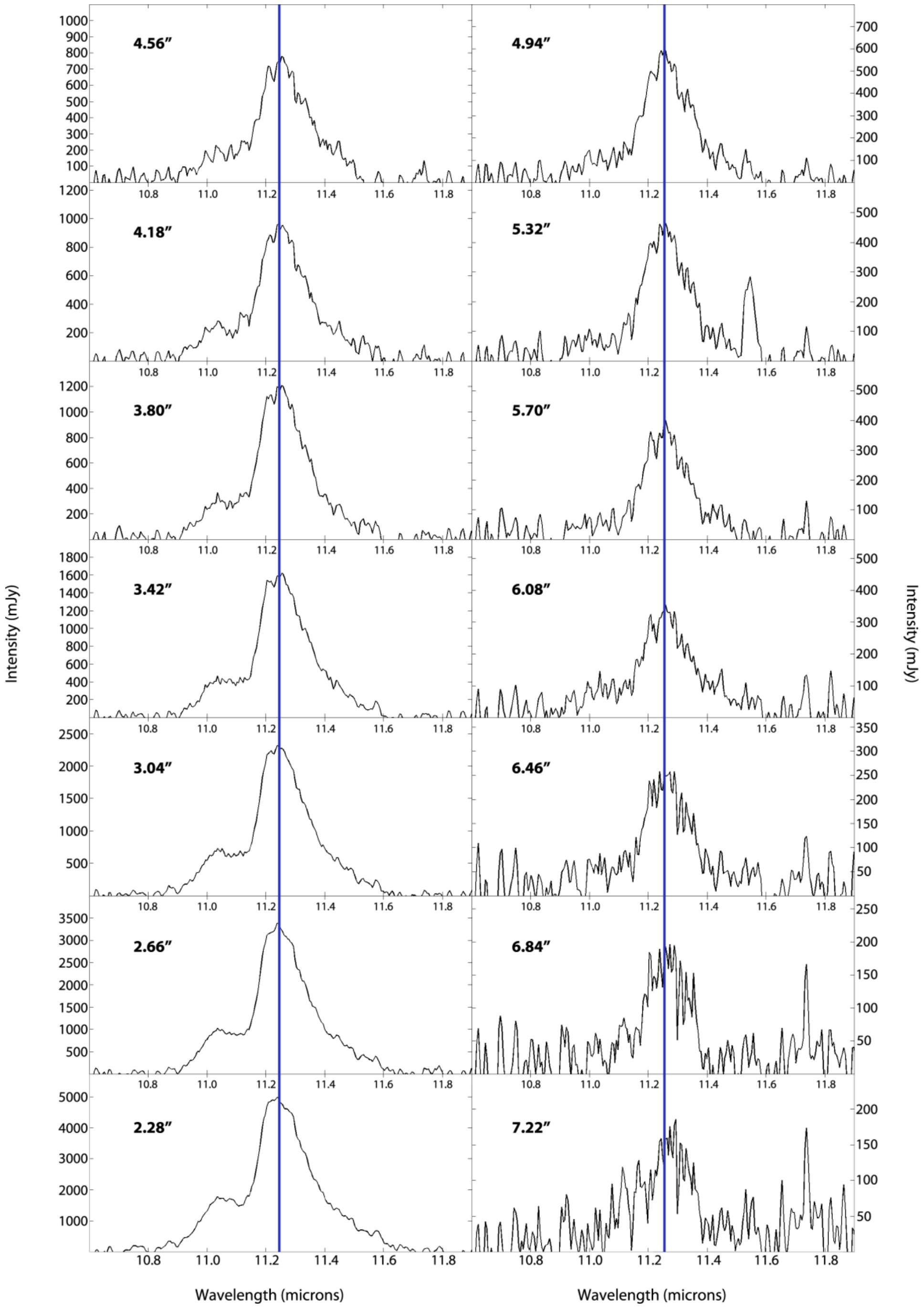

Figure 2.12. Spectra showing the 11.2 μm feature at different offsets along the North West whisker of the Red Rectangle. The blue lines approximately indicate the positions of the peak maxima.

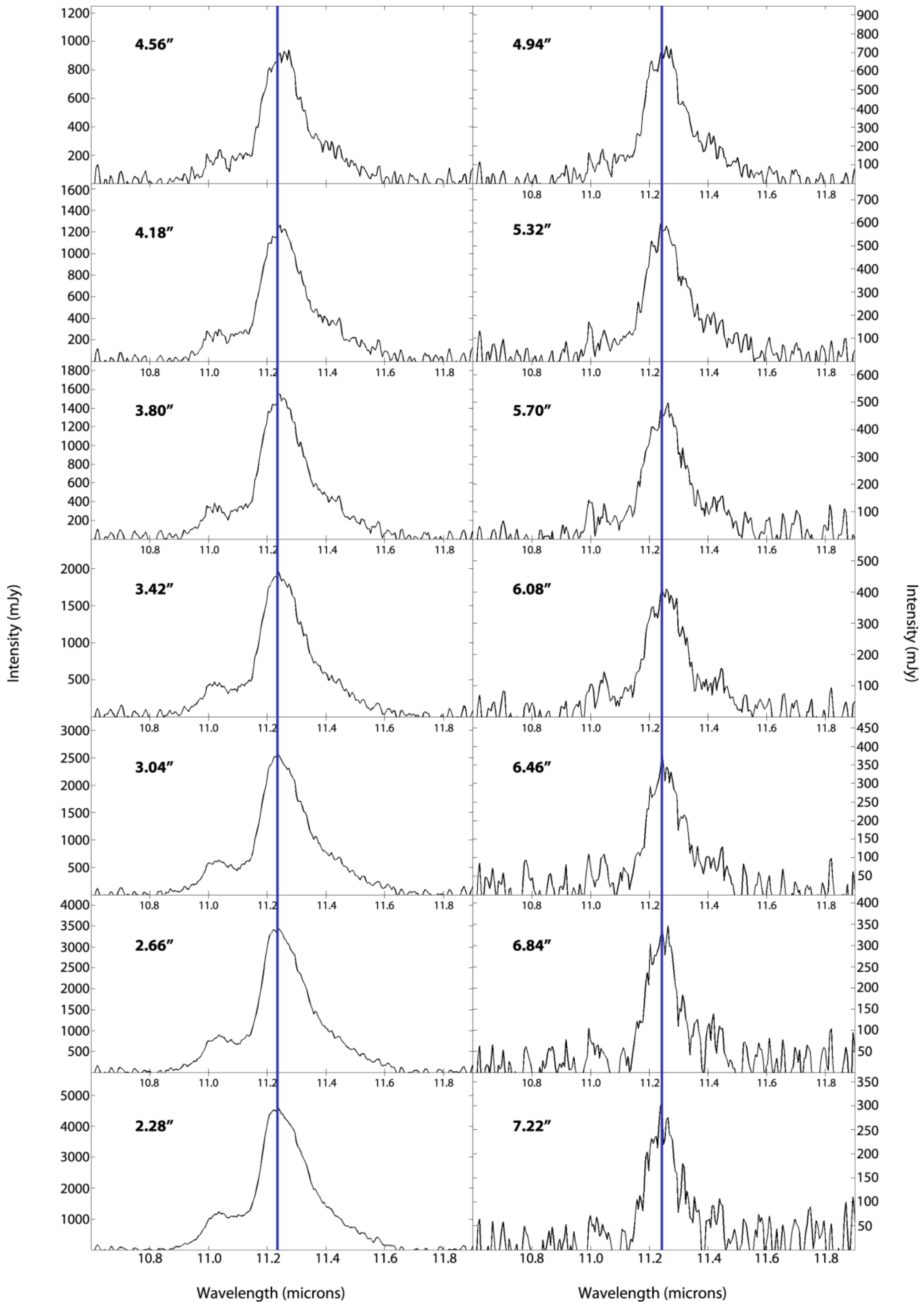

Figure 2.13. Spectra showing the 11.2 μm feature at different offsets along the South East whisker of the Red Rectangle. The blue lines approximately indicate the positions of the peak maxima.

In contrast to the 11.2 μm feature within NGC 7023, which shows variation in the peak position *and* in the shape of the feature, the data for the Red Rectangle shown in Figure 2.12 and Figure 2.13 demonstrates a far larger variation in the band shape than in peak wavelength. While the 11.2 μm feature in NGC 7023 may be thought of as shifting from a Class $A_{11.2}$ profile to a Class $B_{11.2}$ profile with offset, using the van Diedenhoven classification system,[2] that of the Red Rectangle seems to exhibit a shift from Class $A(B)_{11.2}$ to Class $A_{11.2}$ with offset. It has been suggested[12] that objects with a Class $A_{11.2}$ profile are dominated by larger neutral solo-containing PAHs and those with Class $B_{11.2}$ by smaller PAHs, while Class $A(B)_{11.2}$ contains a more even distribution of masses. With this in mind, it is more difficult to interpret the behaviour of the size distribution of PAHs within the Red Rectangle.

It was proposed by Candian & Sarre (2015)[12] that PAHs of (relatively) lower mass give rise to higher wavelength solo C-H OOP emission than higher mass PAHs. The behaviour seen here suggests very little change in the size distribution of the PAHs dominating the population at the various offsets. Following a proposal that the 11.2 μm feature's characteristic steep blue edge originates from a wavelength asymptote that is reached on increased PAH size,[12] it can be predicted that if the origin of the increase in symmetry of the feature with offset is due to a decrease in the steepness of the blue side, this may indicate that fewer high-mass PAHs contribute to the spectrum further away from HD 44179. Alternatively (or additionally), if the increase in the feature's symmetry is caused by an *increase* in the gradient of the red tail, this may correspond to a decline in species that contribute to the red tail component of the peak which, as mentioned earlier, could include species such as smaller PAHs, PAH anions, VSGs, PAH clusters, or hydrogenated PAHs.[27] The former (blue slope) case would be reflected in the outcome of the emission modelling of the band – resulting in a move to a higher proportion of small PAHs with offset – whereas the latter (red slope) would have no effect on the size distribution results as the model does not include the PAH species that are expected to have an effect on the red tail.

2.4.2 Emission modelling results

Figure 2.14 and Figure 2.15 show the emission model (solid line) applied to spectra from the Red Rectangle (dotted line, also shown in Figure 2.12 and Figure 2.13) between offsets of 2.28" and 4.56". The 11.0 μm feature is not included in the fitting. In general, good agreement is found between the model and the data. Agreement is not as close for the data at higher offset, especially along the South East whisker (Figure 2.15), and possible fine structure seen at the top of the peak is not replicated by the model. However, the steep blue side and the major part of the red tail are well fitted for all spectra.

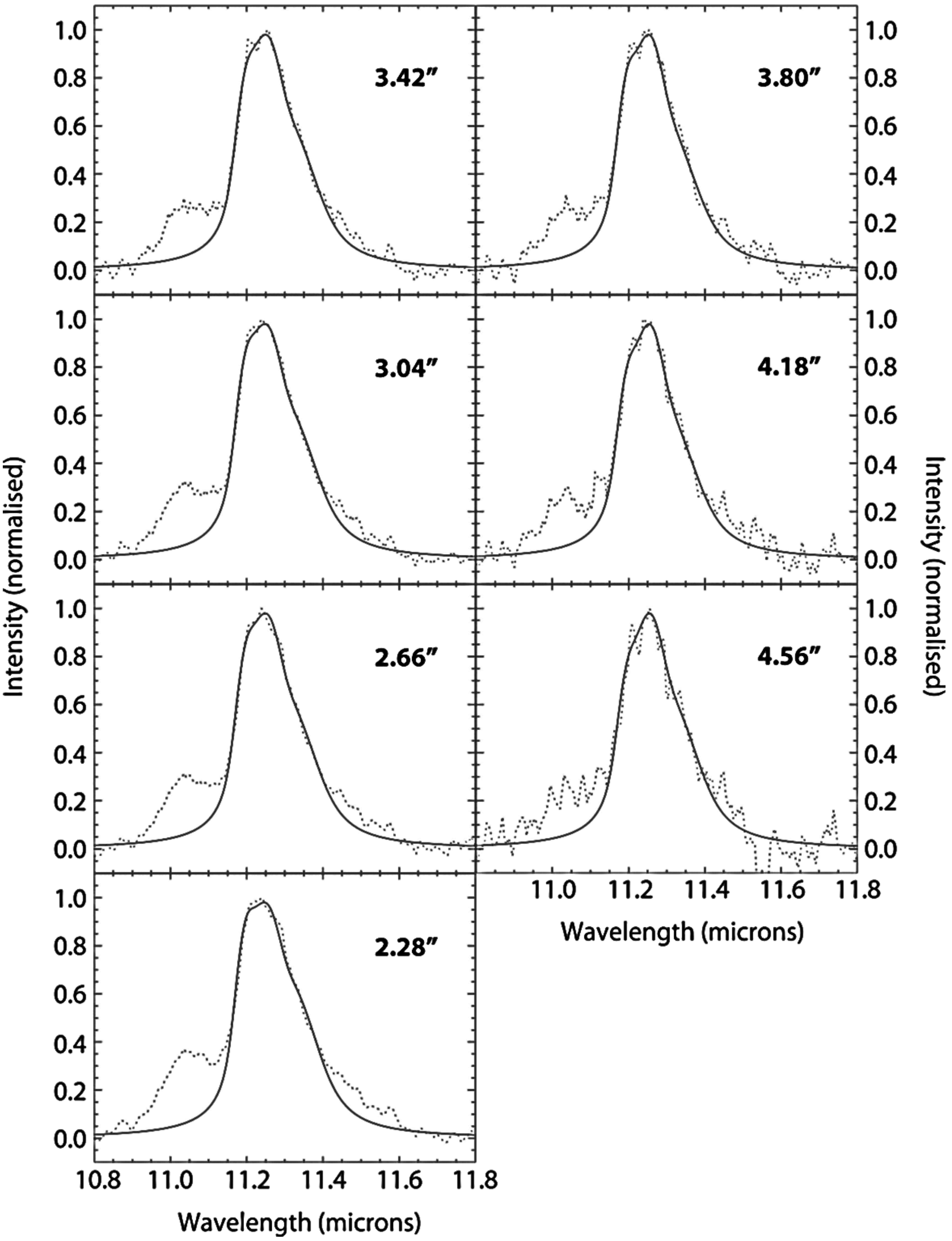

Figure 2.14. Spectra taken along the North West whisker of the Red Rectangle (dotted line) with the fit (solid line) resulting from the emission model.

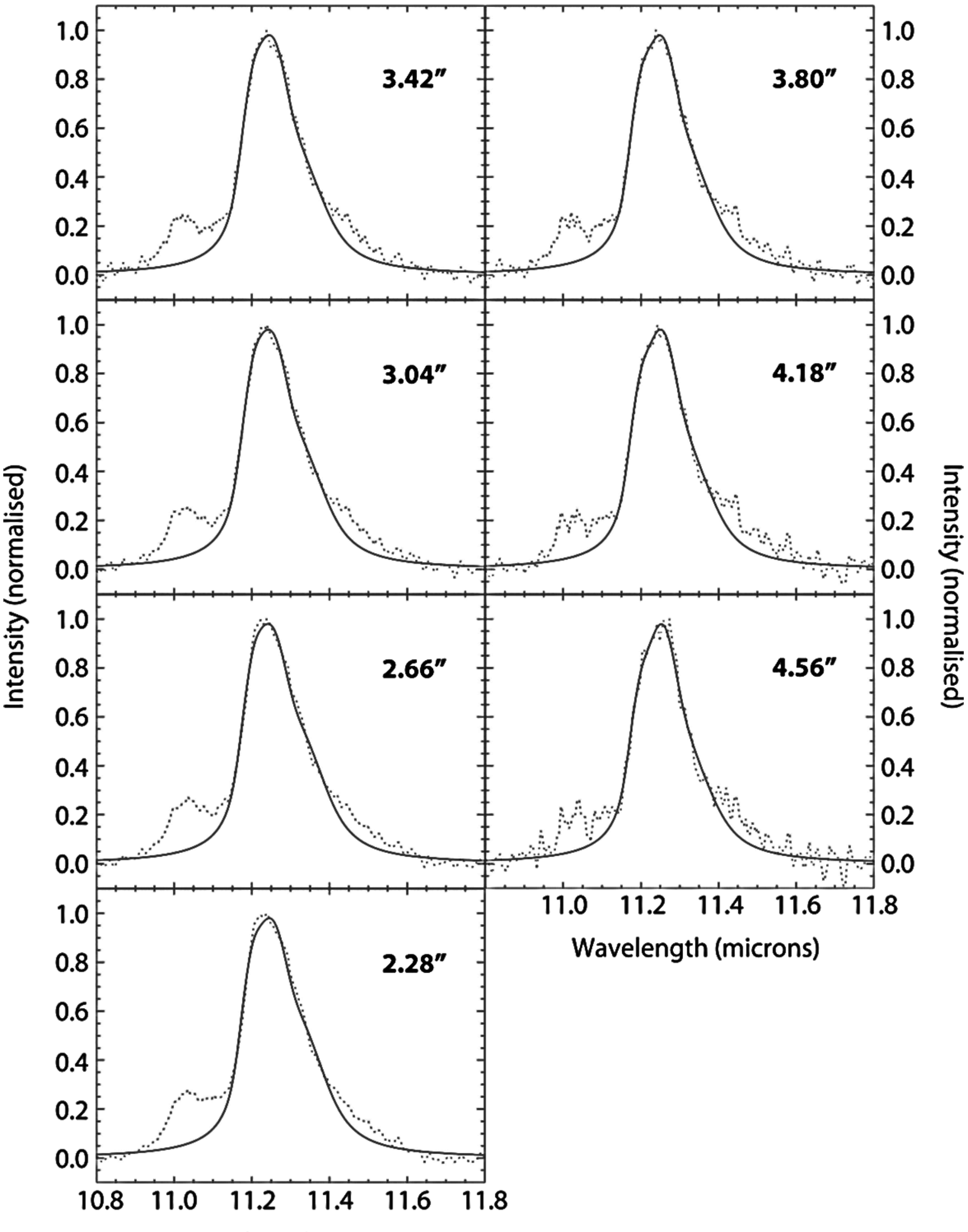

Figure 2.15. Spectra taken along the South East whisker of the Red Rectangle (dotted line) with the fit (solid line) resulting from the emission model.

The ratio of low-mass ($N_C < 50$) to high-mass ($N_C > 50$) PAHs, obtained from the contributions of each PAH according to the fitted results, are given in Table 2.2 and Table 2.3 along with the percentage contributions of low-mass and high-mass PAHs to the overall fit. These values are presented as plots in Figure 2.16 and Figure 2.17. It can be seen that over the range 2.28" – 4.56", there is an increase in the low-mass to high-mass ratio with offset, however this increase is very small. Indeed, the plot of the percentage contributions of low-mass and high-mass PAHs to the overall fit (Figure 2.17) shows these percentages to be almost constant across the range of offset. These results reflect the almost invariant nature of the 11.2 μm feature in the Red Rectangle, in terms of peak position, with the slight increase in the proportion of low-mass PAHs perhaps arising from the slightly decreased gradient of the blue edge of the peak, thus supporting the high-mass PAH asymptote theory of Candian and Sarre.[12]

Table 2.2. Ratio of low-mass to high-mass PAHs (as modelled), and percentage contributions of low-mass and high-mass PAHs, at each offset along the North West whisker of the Red Rectangle nebula.

Offset (arcsec)	Ratio of PAHs (small : large)	% contribution to fit ($N_C < 50$)	% contribution to fit ($N_C > 50$)
2.28	3.39:1	77	23
2.66	3.52:1	78	22
3.04	3.47:1	78	22
3.42	3.60:1	78	22
3.80	3.71:1	79	21
4.18	4.00:1	80	20
4.56	4.45:1	82	18

Table 2.3. Ratio of low-mass to high-mass PAHs (as modelled), and percentage contributions of low-mass and high-mass PAHs, at each offset along the South East whisker of the Red Rectangle nebula.

Offset (arcsec)	Ratio of PAHs (small : large)	% contribution to fit ($N_C < 50$)	% contribution to fit ($N_C > 50$)
2.28	3.27:1	77	23
2.66	3.06:1	75	25
3.04	3.00:1	75	25
3.42	3.06:1	75	25
3.80	3.31:1	77	23
4.18	3.53:1	78	22
4.56	3.81:1	79	21

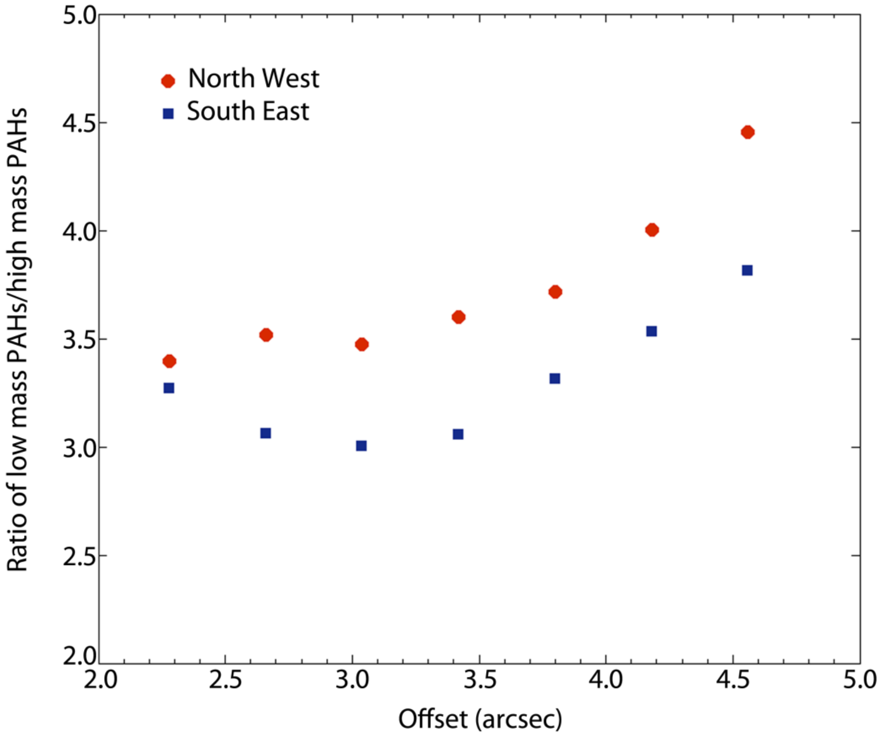

Figure 2.16. Results of the emission model run on the North West (red circles) and South East (blue squares) data of the Red Rectangle. Ratios of low-mass PAHs to high-mass PAHs are presented as a function of offset from the star, in the region 2.28” – 4.56”.

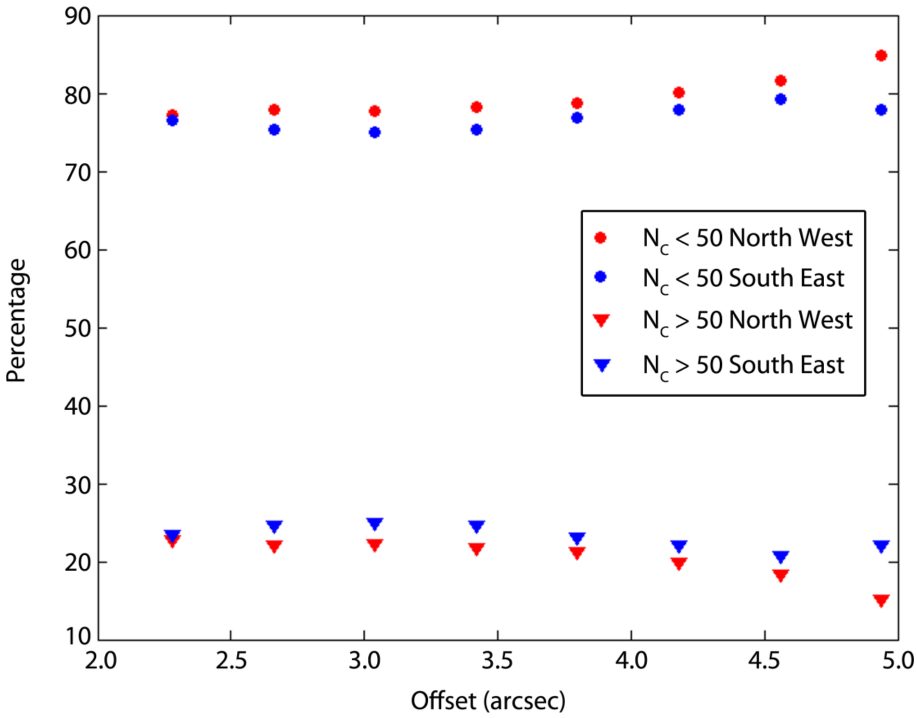

Figure 2.17. The percentage contributions of low-mass ($N_C < 50$) and high-mass ($N_C > 50$) PAHs to the overall fit to the 11.2 μm feature at each offset along the North West and South East whiskers of the Red Rectangle.

2.4.3 Implications for PAH mass distribution

The emission model results reported in Section 2.4.2 suggest very little change in the mass distribution of PAHs with offset in the Red Rectangle, based on the sample of four neutral, solo-containing PAHs used. This Section includes a discussion relating to additional trends seen in the spectra of the Red Rectangle with offset, the limits of the emission model in this case, and implications for the PAH mass distribution in this object.

Within the 3.3 μm C-H stretch feature, the increase in relative intensity of the 3.28 μm component with offset[37] indicates an increase in the number of bay hydrogens within the PAH population further from the star.[15] It was proposed that an increase in the number of bay hydrogens could be achieved by addition of rings to the PAH molecule, this size development being based also on a corresponding increase in the 3.4 μm feature which is generally attributed to the addition of hydrogen and/or methyl groups to the PAH structure. This would then mean that there is either a shift in the type of edge structure of PAHs with increased offset (*i.e.* more duo/bay type H atoms and fewer solos), or a growth in the molecular size of PAHs, or both.

As the 3.3 μm feature concerns all of the hydrogen atoms on a PAH, and the 11.2 μm feature is only associated with solo hydrogens, the ratio of the intensities of these bands ($I_{3.3}/I_{11.2}$) can be used as an indicator of PAH size. To justify this, Figure 2.18 shows a plot of the ratio of the total number of hydrogens a PAH contains (H_{tot}) to the number of solo hydrogen atoms a PAH has (H_{solo}), and how this varies with carbon mass (*i.e.* atomic weight minus the mass of hydrogen atoms) of the PAH. This has been calculated for four ‘families’ of PAHs, given in the lower half of the Figure. A general trend is seen showing an increase in mass can be associated with a lower ratio, *i.e.* a higher number of solo hydrogens. Similarly, Croiset *et al.*[16] show the correlation of the ratio of the intensity of the 11.2 μm feature to the intensity of the 3.3 μm feature, for the calculated spectra of a number of PAH molecules, with the number of C atoms in the PAH. The result of their plot was a strong relationship between the $I_{11.2}/I_{3.3}$ and PAH size.

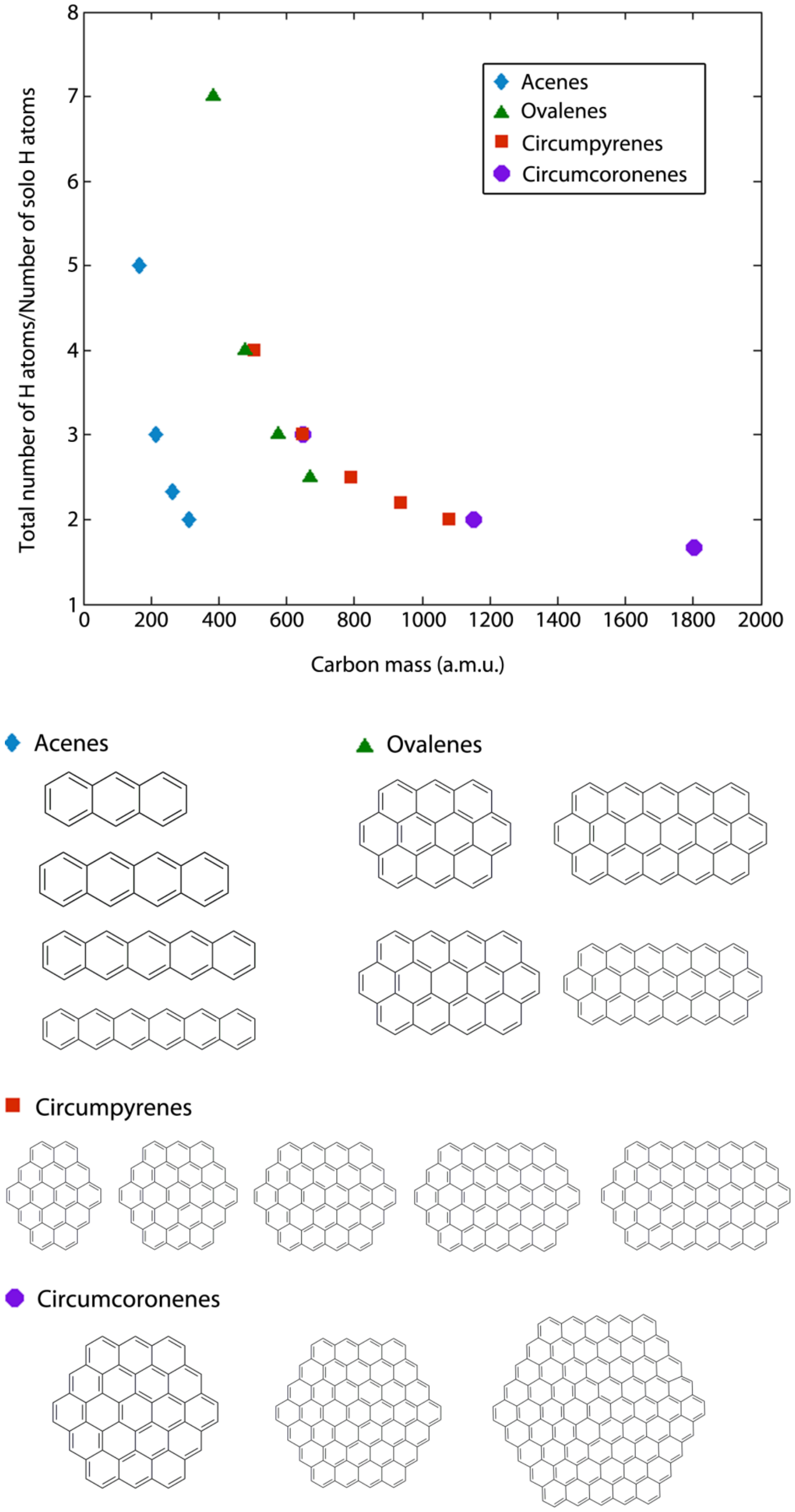

Figure 2.18. The ratio of $H_{tot}(3.3)/H_{solo}(11.2)$ as a function of carbon mass (upper half) for four 'families' of PAHs (lower half).

Using the correlation demonstrated in Figure 2.18, the $I_{3.3}/I_{11.2}$ ratio was measured at different offsets along the North West whisker of the Red

Rectangle, and the resulting plot is given in Figure 2.19. This shows a clear decrease in the $I_{3.3}/I_{11.2}$ ratio with increased offset, indicating an increase in the number of solo hydrogen atoms, and therefore an increase in the molecular size of the PAH population. This result agrees with those mentioned previously, based on the $I_{3.30}/I_{3.28}$ ratio.[37] Interestingly, the trend shown in Figure 2.19 appears to level off from about 3.5" onwards, indicating that while there is an increase in the size of PAHs initially, there is then little variation in their size moving further out to larger offsets.

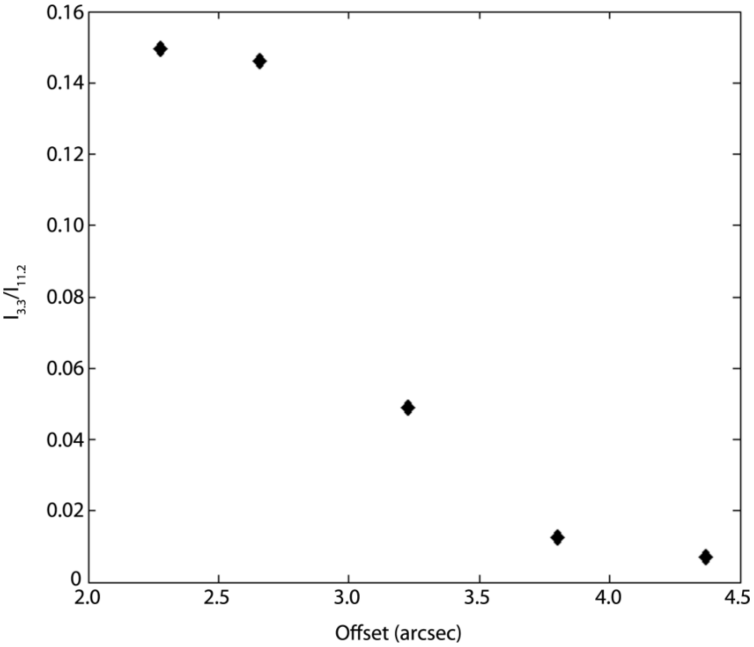

Figure 2.19. The $I_{3.3}/I_{11.2}$ ratio as a function of offset along the North West whisker of the Red Rectangle.

The ratio of the intensities of the 11.2 μm and 12.7 μm features ($I_{12.7}/I_{11.2}$) was calculated at each offset. The 12.7 μm feature is sometimes attributed to the OOP bend of duo hydrogens,[8] and so investigating any changes in this ratio may indicate a change in the proportion of PAHs with certain edge structures, *i.e.* zig-zag (solo-containing) or armchair (duo/bay-containing). The results of this are given in Figure 2.20, which shows very little variation in the $I_{12.7}/I_{11.2}$ ratio with offset, suggesting little to no change in the edge structure of the PAH population. However, there are additional features between 13 and 15 μm that are also attributed to C-H OOP bend modes of duo, trio and quartet hydrogens that are not included in the data here, and so a full analysis of PAH edge structure is not possible.

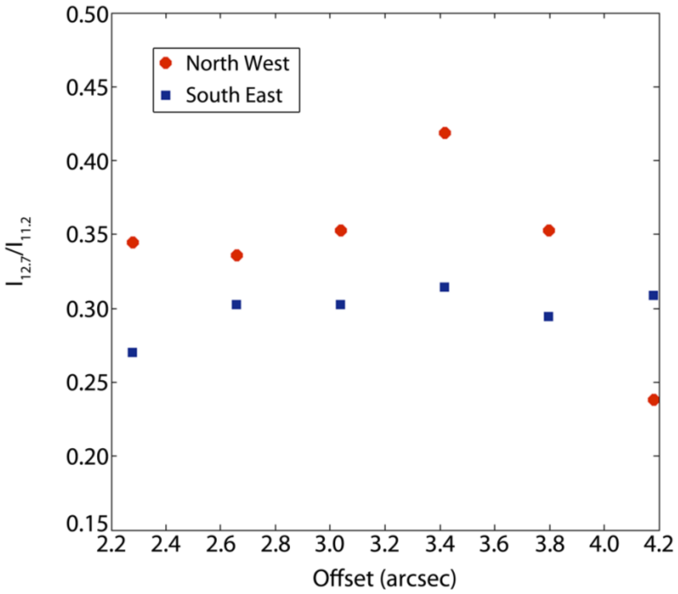

Figure 2.20. The $I_{12.7}/I_{11.2}$ ratio as a function of offset along the North West (red circles) and South East (blue squares) whiskers of the Red Rectangle.

It can be seen from Figure 2.12 and Figure 2.13 that the feature at 11.0 μm, the carrier of which is still somewhat in dispute, is prominent at offsets closer to the star within the Red Rectangle, but decreases in intensity significantly with increasing offset. Candian and Sarre[12] report that for the 11.2 μm feature, the wavelength of the solo C-H OOP bend feature reaches asymptotic values for higher mass PAHs – this accounting for the characteristic steep blue side of the feature. The same phenomenon holds for acenes; the wavelength calculated by Candian and Sarre for anthracene falls at 11.41 μm, however for acenes of higher mass (hexacene, heptacene, for example), the wavelength of this feature converges towards an asymptotic value of about 11.03 μm.[12] It is proposed, therefore, that high-mass acenes contribute to the 11.0 μm emission feature. In the context of the work described here, as the 11.0 μm feature decreases in intensity with increased offset, we can infer that the population of high-mass acenes is decreasing with offset.

It is important also to note that the emission model results track only the population of *solo-containing* PAHs. PAHs that contain very few, or no, solo hydrogens and a higher number of duo, trio or quartet hydrogens are not accounted for in this model, as their contribution to the 11.2 μm feature would be negligible or zero. Because of this, there may be changes in the mass distribution of PAHs that have different non-solo/zig-zag edges, for example PAHs with an armchair-type edge structure (*i.e.* duo/bay hydrogens) that would have no contribution to the 11.2 μm solo OOP feature, which would not be represented within the emission model results presented in this Chapter. Indeed, if there were an increase in the proportion of high-mass armchair-edged PAHs with offset, this would support the increase in the relative intensity of the 3.28 μm feature with offset mentioned previously.

Combining the trends discussed in this Section, all of which indicate an increase in PAH size with offset in the Red Rectangle, and comparing these with the emission model results of Section 2.4.2, which show very little change in the PAH mass distribution, indicates that perhaps in this case the emission model provides slightly misleading results. As mentioned previously, the main variation in the 11.2 μm feature within the Red Rectangle is an increase in the symmetry of the peak with increased offset, due in part to a decline in the red tail. Following the proposal by Candian and Sarre that smaller PAHs contribute to the red tail of the 11.2 μm feature,[12] the decline of this component along with the 11.0 μm feature may in fact indicate a decrease in the proportion of low-mass PAHs, including higher mass acenes, with increasing offset. This idea is in support of the conclusions of the other trends discussed previously, although it is not reflected in the emission model results. This seems, in the case of the Red Rectangle, to be a limitation of the model itself. The main variations in the 11.2 μm feature arise from the 11.0 μm peak and the red tail component, both of which are underrepresented within the current model, and both of which may be distorting the fitted shape, so that for this data set, the use of just four PAHs within the model cannot accurately replicate the variations that are being seen.

2.4.4 Comparing the Red Rectangle and NGC 7023

It is interesting to compare the profiles of the 11.2 μm feature of NGC 7023 and the Red Rectangle. The data closest to HD 44179, without the silicate contaminant, along the South East whisker of the Red Rectangle, closely matches that for 49.5” offset in NGC 7023, in terms of profile (Figure 2.21). With increasing offset, and increasing proportion of high-mass PAHs as proposed previously, it is interesting that the profile of the 11.2 μm feature in the Red Rectangle does not reach the steepest blue side or narrow 11.20 μm feature that is seen for NGC 7023, in the data closer to the star HD 200775, where the PAHs are larger. This suggests that although there may be an increase in the proportion of high-mass PAHs with offset within the Red Rectangle, the PAHs do not reach the high masses as in NGC 7023, resulting in the asymptotic value being more weakly represented.

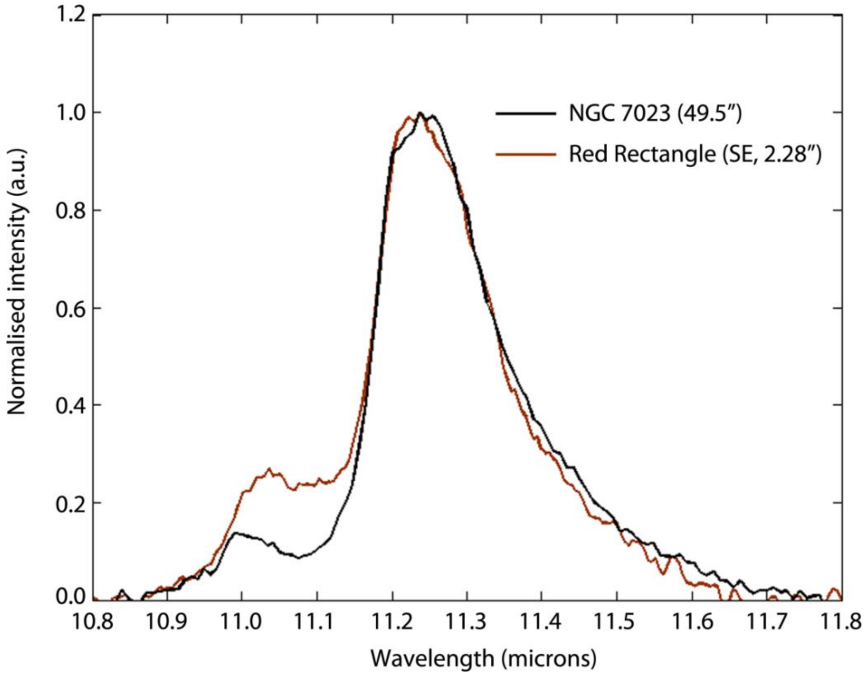

Figure 2.21. Comparison of the 11.2 μm feature of NGC 7023 (at an offset of 49.5”; black line), and the Red Rectangle (South East whisker, offset of 2.28”; red line).

If the PAH population in the Red Rectangle is indeed reaching a point at which the molecules do not get any larger, an idea that is reflected in the trend of the $I_{3.3}/I_{11.2}$ ratio (Figure 2.19), this may have interesting implications for the chemistry within this object. For example, the Red Rectangle is an object which contains very strong PAH features, but no detection of the fullerene C_{60} has been reported. It has been found that top-down mechanisms beginning with PAHs of a size 60 – 66 C atoms may be an important route to fullerene formation[31, 40] (see also Chapter 3 of this Thesis), and so if PAHs within the Red Rectangle are simply not reaching this size then this provides a possible explanation as to the apparent absence of the fullerene molecules from this object.

2.5 Conclusions

This Chapter has presented the results of an emission model used to investigate the varying profile of the 11.2 μm feature in relation to variations in the mass distribution of the PAHs responsible for the band. This work marks the first time that this particular emission model, notable for its inclusion of object-specific parameters and the use of four neutral PAHs, has been used to fit data taken at different positions *within* two astronomical objects. Results of the emission model are interpreted in terms of a ratio of low-mass ($N_C < 50$) PAHs to high-mass ($N_C > 50$) PAHs, and in this way the change in the mass distribution of PAHs in the population within each object could be tracked.

The results of the emission model carried out on data taken at different offsets from the exciting star HD 200775 in NGC-7023-NW showed, according to the ratio of low-mass to high-mass PAHs, that there is an increase in the proportion of low-mass PAHs with increased distance from the star. These results, combined with additional analysis from previous studies,[6, 28-30] have been used to create an overall picture in which the changes in the PAH population are tracked and explained in terms of the changing intensity of the radiation field within NGC-7023-NW. This involves a larger proportion of low-mass PAHs at further positions from the star, where they are expected to be able to survive the lower radiation field. Moving closer to the star, the proportion of low-mass PAHs decreases as the radiation field increases in strength, and, closer still, PAH cations are expected to dominate, followed by the fullerene C_{60} and finally C_{60}^+, which is detected close to the star where the radiation field is the strongest. This trend of stability in an increased radiation field, where C_{60}^{+} > C_{60} > PAH^{+} > high-mass PAHs > low-mass PAHs, has a corresponding trend in the proportion of edge atoms on the molecule. For example, low-mass PAHs have a high proportion of edge atoms relative to the mass of the whole molecule, whereas C_{60} has no reactive edges. This likely contributes to the observed stability of the molecules and results in the evolution that is seen.

The evolution of the PAH population to a higher proportion of low-mass PAHs agrees with the results of Boersma *et al.*, which were achieved using a fitting tool including theoretical spectra of all of the PAHs within the NASA Ames PAH database.[6] This agreement supports the emission model used within this Chapter as a viable tool for exploring the profile of the 11.2 μm feature in terms of the mass distribution of PAHs, using four representative neutral, solo-containing PAHs.

The emission model was applied to fit data obtained at different offsets from the central star of the Red Rectangle nebula, along the North West and South East ‘whiskers’. The results of this showed very little variation in the PAH mass distribution with increased offset. These results were compared with the trends with offset seen in other emission bands: The previously reported $I_{3.28}/I_{3.30}$ ratio increases with offset,[37] showing a growth in the relative proportion of the 3.28 μm component which is attributed to the CH stretch of bay hydrogens, which in turn implies an increase in the size of PAHs with increased offset. Additionally, a decreasing $I_{3.3}/I_{11.2}$ ratio with offset also indicates an overall size increase of the PAHs in the population of the Red Rectangle. While the results of the emission model showed little change in the PAH mass distribution, the main variations in the 11.2 μm profile come from a decline in the 11.0 μm feature and a decline in the red tail – both of these components being thought to be linked to small PAHs or acenes. This suggests that the proportion of high-mass PAHs may indeed be increasing with offset, as indicated by the other emission band trends, and that in this case, the 11.0 μm feature and red tail component may be distorting the fitted peak shape such that the four PAHs used within the model are not sufficient to provide a full picture of a variation in mass distribution with offset.

It is worth considering the apparent limitations of the emission model in its current state, based on the case of the Red Rectangle, in the eventuality of applying the model to a different astronomical object. If this were to occur in future research, then these limitations should drive the choice of object. For example, the model's success in the case of NGC 7023 would indicate that spectra covering a large area or distance within an object, and those that exhibit the largest spectral variation, would be a natural choice for a follow-up study.

A greater understanding of the size, shape, edge structure and ionisation of PAHs that make up an emission spectrum would aid in the analysis of chemical and physical astrophysical conditions. The work presented in this Chapter provides evidence that the profile of the 11.2 μm band can be used to predict the nature of the PAH population in terms of the mass distribution. In particular, a steep blue edge and shorter peak wavelength – Class $A_{11.2}$ in the classification of van Diedenhoven[2] – corresponds to a higher proportion of high-mass solo-containing PAHs, whereas a longer peak wavelength and a more extended red tail – Class $B_{11.2}$ – is assigned to a higher proportion of low-mass PAHs. This marks a significant step forward in utilising specific bands and their variation in profile as a probe of PAH population.

2.6 References

1. A. G. G. M. Tielens, *Ann. Rev. Astron. Astrophys.*, 2008, **46**, 289-337.
2. B. van Diedenhoven, E. Peeters, C. Van Kerckhoven, S. Hony, D. M. Hudgins, L. J. Allamandola and A. G. G. M. Tielens, *ApJ*, 2004, **611**, 928-939.
3. O. Berné, C. Joblin, Y. Deville, J. D. Smith, M. Rapacioli, J. P. Bernard, J. Thomas, W. Reach and A. Abergel, *Astron. Astrophys.*, 2007, **469**, 575-586.
4. M. J. F. Rosenberg, O. Berné, C. Boersma, L. J. Allamandola and A. G. G. M. Tielens, *Astron. Astrophys.*, 2011, **532**, A128.
5. C. Boersma, R. H. Rubin and L. J. Allamandola, *ApJ*, 2012, **753**, 168
6. C. Boersma, J. D. Bregman and L. J. Allamandola, *ApJ*, 2013, **769**, 117.

7. E. Peeters, S. Hony, C. Van Kerckhoven, A. G. G. M. Tielens, L. J. Allamandola, D. M. Hudgins and C. W. Bauschlicher, *Astron. Astrophys.*, 2002, **390**, 1089-1113.

8. S. Hony, C. Van Kerckhoven, E. Peeters, A. G. G. M. Tielens, D. M. Hudgins and L. J. Allamandola, *Astron. Astrophys.*, 2001, **370**, 1030-1043.

9. G. C. Sloan, M. Jura, W. W. Duley, K. E. Kraemer, J. Bernard-Salas, W. J. Forrest, B. Sargent, A. Li, D. J. Barry, C. J. Bohac, D. M. Watson and J. R. Houck, *ApJ*, 2007, **664**, 1144-1153.

10. D. M. Hudgins and L. J. Allamandola, *ApJ*, 1999, **516**, L41-L44.

11. M. Rapacioli, C. Joblin and P. Boissel, *Astron. Astroph.*, 2005, **429**, 193.

12. A. Candian and P. J. Sarre, *MNRAS*, 2015, **448**, 2960-2970.

13. M. J. Shannon, D. J. Stock and E. Peeters, *ApJ*, 2016, **824**.

14. A. Candian, PhD Thesis, The University of Nottingham, 2011.

15. A. Candian, T. H. Kerr, I.-O. Song, J. McCombie and P. J. Sarre, *MNRAS*, 2012, **426**, 389-397.

16. B. A. Croiset, A. Candian, O. Berné and A. G. G. M. Tielens, *Astron. Astrophys.*, 2016, **590**, A26.

17. A. Léger, L. d'Hendecourt and D. Defourneau, *Astron. Astrophys.*, 1989, **216**, 148-164.

18. A. Pathak and S. Rastogi, *Astron. Astrophys.*, 2008, **485**, 735-742.

19. D. J. Cook and R. J. Saykally, *ApJ*, 1998, **493**, 793-802.

20. G. Malloci, C. Joblin and G. Mulas, *Chem. Phys.*, 2007, **332**, 353-359.

21. M. W. Werner, K. I. Uchida, K. Sellgren, M. Marengo, K. D. Gordon, P. W. Morris, J. R. Houck and J. A. Stansberry, *ApJS*, 2004, **154**, 309-314.

22. A. N. Witt, K. D. Gordon, U. P. Vijh, P. H. Sell, T. L. Smith and R. H. Xie, *ApJ*, 2006, **636**, 303-315.

23. B. Fleming, K. France, R. E. Lupu and S. R. McCandliss, *ApJ*, 2010, **725**, 159-172.

24. D. Cesarsky, J. Lequeux, A. Abergel, M. Perault, E. Palazzi, S. Madden and D. Tran, *Astron. Astroph.*, 1996, **315**, L305.

25. M. W. Werner, T. L. Roellig, F. J. Low, G. H. Rieke, M. Rieke, W. F. Hoffmann, E. Young, J. R. Houck, B. Brandl, G. G. Fazio, J. L. Hora, R. D. Gehrz, G. Helou, B. T. Soifer, J. Stauffer, J. Keene, P. Eisenhardt, D. Gallagher, T. N. Gautier, W. Irace, C. R. Lawrence, L. Simmons, J. E. Van Cleve, M. Jura, E. L. Wright and D. P. Cruikshank, *ApJS*, 2004, **154**, 1-9.

26. C. W. Bauschlicher, Jr., C. Boersma, A. Ricca, A. L. Mattioda, J. Cami, E. Peeters, F. S. de Armas, G. P. Saborido, D. M. Hudgins and L. J. Allamandola, *ApJS*, 2010, **189**, 341-351.

27. C. Boersma, J. Bregman and L. J. Allamandola, *ApJ*, 2014, **795**, 110.

28. K. Sellgren, K. I. Uchida and M. W. Werner, *ApJ*, 2007, **659**, 1338-1351.

29. K. Sellgren, M. W. Werner, J. G. Ingalls, J. D. T. Smith, T. M. Carleton and C. Joblin, *ApJ Lett.*, 2010, **722**, L54-L57.

30. O. Berné, G. Mulas and C. Joblin, *Astron. Astrophys.*, 2013, **550**.

31. O. Berné and A. G. G. M. Tielens, *PNAS*, 2012, **109**, 401-406.

32. M. Cohen, C. M. Anderson, A. Cowley, G. V. Coyne, W. M. Fawley, T. R. Gull, E. A. Harlan, G. H. Herbig, F. Holden, H. S. Hudson, R. O. Jakoubek, H. M. Johnson, K. M. Merrill, F. H. Schiffer, B. T. Soifer and B. Zuckerman, *ApJ*, 1975, **196**, 179.

33. L. B. F. M. Waters, C. Waelkens, H. van Winckel, F. J. Molster, A. G. G. M. Tielens, J. T. van Loon, P. W. Morris, J. Cami, J. Bouwman, A. de Koter, T. de Jong and T. de Graauw, *Nature*, 1998, **391**, 868-871.

34. J. D. Bregman, D. Rank, P. Temi, D. Hudgins and L. Kay, *ApJ*, 1993, **411**, 794-796.

35. G. C. Sloan, G. L. Grasdalen and P. D. Levan, *ApJ*, 1993, **409**, 412-416.

36. M. Cohen, H. Van Winckel, H. E. Bond and T. R. Gull, *AJ*, 2004, **127**, 2362-2377.

37. I.-O. Song, J. McCombie, T. H. Kerr and P. J. Sarre, *MNRAS*, 2007, **380**, 979-985.

38. R. Topalovic, PhD Thesis, The University of Nottingham, 2006.

39. T. Miyata, H. Kataza, Y. K. Okamoto, T. Onaka, S. Sako, M. Honda, T. Yamashita and K. Murakawa, *Astron. Astroph.*, 2004, **415**, 179-187.

40. O. Berné, J. Montillaud and C. Joblin, *Astron. Astroph.*, 2015, **577**, A133-A141.

3. Irradiation of PAHs towards the formation of C_{60}

3.1 Background

Ever since the serendipitous discovery of C_{60} in 1985,[1] this stable, cage-like molecule has been expected to exist in the interstellar medium (ISM) due to similarities between the high-energy, low-pressure and carbon-rich environment in which it can be formed in the laboratory and conditions in at least some regions in interstellar space. C_{60}, although thought to be a possible carrier for a small number of astronomical infrared spectral emission features for some time,[2, 3] was only confirmed in a planetary nebula (Tc-1) and in reflection nebulae (NGC 7023 and NGC 2023) for the first time in 2010.[4-6] Since the initial detection, which in the case of Tc-1 was accompanied by the detection of C_{70},[4] the characteristic vibrational bands of C_{60} have been found in a number of objects that range from early[7] to late[8-14] stages of stellar evolution.

Studies on the formation of C_{60} in the laboratory have so far generally focussed on 'bottom-up' mechanisms involving the building up of fullerene cages from smaller carbon clusters, C_2 units or atomic carbon.[15-17] C_{60} has been found to form from the electric arc vaporisation of carbon rods,[18] the combustion of hydrocarbons,[19] and *via* a 12-step synthesis from organic starting materials that yields only C_{60}.[20] While the chemical species, temperatures and gas pressure required for 'bottom-up' synthesis of C_{60} are found in some astrophysical environments, typically the densities in the ISM are so low that fullerene formation in this way would require unreasonably long timescales.[21, 22]

High-resolution transmission electron microscopy (TEM) has revealed that flakes of graphene can transform into C_{60} as a result of high energy electron beam (e-beam) irradiation.[23] This transformation occurs *via* the loss of carbon atoms from the edge of the graphene, resulting in the formation of five-membered rings within the structure. These pentagons introduce curvature which is an essential step in the 'zipping' up of the initially planar structure to form a fullerene cage. This work included calculated energies of the required intermediates and reveals the stability of fullerene molecules, and hence the overall driving force for the formation process. Comparison between the experimental conditions in TEM and the conditions in the ISM have led to a proposed 'top-down' interstellar C_{60} formation mechanism by Berné and Tielens involving UV photo-processing of large polycyclic aromatic hydrocarbons (PAHs).[21]

Following a suggestion that hydrogenated amorphous carbon (HAC) might be a source of fullerenes, *via* photochemical processing,[8, 10] Micelotta *et al.*[22] presented a detailed model involving UV photolysis, and hence dehydrogenation, of HAC particles resulting in so-called arophatic structures - particles containing aromatic clusters linked by aliphatic bridging groups. Through further dehydrogenation five-membered rings are introduced into the arophatic structure resulting in giant fullerenic cages which then shrink down by the ejection of C_2 fragments to form stable C_{60} or C_{70} cages. Micelotta *et al.* contended that terrestrially-based routes for C_{60} formation, including that proposed by Berné and Tielens,[21] are not applicable to objects such as NGC 7023, and suggest that the proposed arophatic structures are the key to fullerene formation. However, it is reported that the aliphatic component in the reflection nebula NGC 7023 is very low, being under 2% of the carbon budget, and so a route for fullerene formation dependent on aliphatic group-containing structures is unlikely to be feasible.[24, 25]

The 'top-down' formation mechanism outlined by Berné and Tielens involves UV-photolysis-initiated dehydrogenation of large PAHs containing approximately 70 C atoms to form graphene flakes.[21] Fullerene formation is then initiated by the loss of a carbon atom and subsequent pentagon formation within the structure. This has recently been explored theoretically by Galué in a study carried out to calculate the infrared spectra of intermediates in the fullerene formation process and to make comparison with the interstellar 'aromatic infrared bands' (AIBs).[26] The results indicate that strained or curved carbon nanostructures, *i.e.* intermediates in the fullerene formation process, may be abundant in the ISM and may even be responsible for certain previously unexplained features in the AIB spectrum. This top-down model is additionally supported by laboratory studies that revealed photofragmentation patterns of large PAHs (> 60 C atoms) which are consistent with the formation of C_{60}.[27] Recent modelling of the top-down conversion of circumovalene ($C_{66}H_{20}$) to C_{60} under the conditions found in NGC 7023 suggests that only PAH molecules containing between 60 and 66 carbon atoms would be of practical significance for the formation of C_{60} in this object.[25] This is due to the extended timescale needed for the loss of C_2 units in the shrinking of larger structures down to C_{60}.

The work described in this Chapter investigates whether there is a link between the formation of the fullerene C_{60} and discrete, small (< 60 C atom) PAH molecules of the shape and size commonly expected to exist in the ISM. Using specific molecular precursors in the laboratory makes it possible to investigate the mechanistic steps involved in the fullerene formation process by this route, which can then be used to develop a more detailed picture of the steps involved in interstellar fullerene formation. The fact that fullerenes are closed cages with no reactive edges means that they are likely to correspond to a very thermodynamically stable form of carbon under interstellar conditions. As such, it is expected that fullerene formation will be favoured when exposing PAHs, with their many edge C-H bonds that may be susceptible to dissociation under certain conditions, to various forms of photo- and particle irradiation.

Experiments are detailed that were designed and carried out with the intention of replicating conditions similar to those found in interstellar environments. Four separate PAHs, anthracene, pyrene, perylene and coronene (structures shown in Figure 3.1), were exposed, under vacuum, to irradiation in the form of the electron beam of TEM (Section 3.3) or the UV laser of matrix-assisted laser desorption/ionisation time-of-flight mass spectrometry (MALDI-TOF MS) (Section 3.4), in order to initiate transformations within the samples and to determine the nature of the products formed as a result of such transformations. In addition, a new experimental methodology was designed and implemented to utilise both of the aforementioned experimental techniques to enable characterisation of species and initiation of transformations within a specific physical area of a sample, so that the transformation processes and molecular species can be observed at each step of the experiment (Section 3.5).

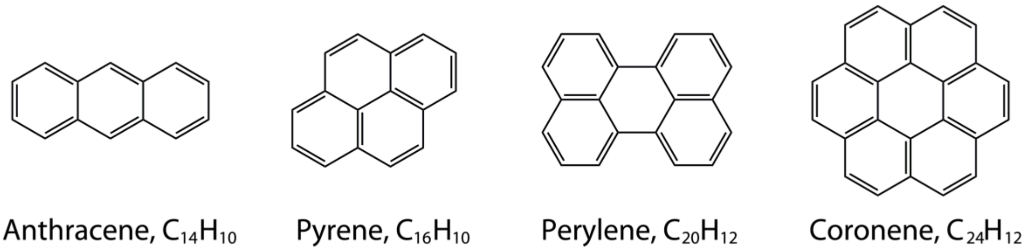

Figure 3.1. Structures of the four PAHs used in experiments described in this Chapter.

3.2 Experimental details

The PAH samples (coronene, perylene, pyrene and anthracene) were obtained from Sigma-Aldrich and used as received. For the TEM samples, graphite flakes (~ 1 mg, Fisher Scientific: Graphite powder, Supplier: Fisher Scientific, Code: G/0900/60, Batch: 0438775, Cas No.: 7782-42-5) were dispersed in HPLC-grade isopropyl alcohol (IPA) (4 mL) using an ultrasonic bath, drop-cast (25 drops) onto lacey carbon-coated copper TEM grids (AGAR) and allowed to dry. The PAH sample (~ 0.5 mg) was dispersed in HPLC-grade IPA (4 mL) using an ultrasonic bath and drop-cast (25 drops) on top of the graphite flakes. The grid was then dried under a flow of N_2 for 1 min. For the MALDI-TOF mass spectrometry experiments, the PAH sample (~ 1 mg) was dispersed in acetonitrile (2 mL) using an ultrasonic bath, and was drop-cast (1 drop) onto a stainless steel Multiprobe Adapter MALDI target. No matrix solutions were deposited with the sample. For the combined methodology experiments (Section 3.5), a holey carbon TEM finder grid (Agar Scientific) was used for sample preparation. The grid was then secured to a stainless steel Multiprobe Adapter MALDI target using adhesive tape for laser irradiation. Finally, the grid was removed from the MALDI target plate and TEM imaging performed on the resultant sample.

TEM imaging of the samples was carried out using a JEOL-2100F TEM at an accelerating voltage of 100 kV. When using TEM as a probe the e-beam was spread in order to keep the total dose of electrons as low as possible to avoid inducing changes in the sample.

UV laser irradiation experiments were carried out using a Bruker Ultraflex III MALDI-TOF mass spectrometer in positive reflection mode. This was equipped with a pulsed Nd:YAG 355 nm laser with 5 ns-duration pulses of ~ 500 µJ pulse^{-1}. Each spectrum was acquired from an average of 200 shots.

DFT calculations were run using QChem[28] using the B3LYP functional with the 6-31G* basis set. Optimised geometries of structures were viewed using the Gabedit software package.

3.3 Transmission Electron Microscopy of PAHs

TEM is a useful tool for probing transformations of carbon species, due to the ability to watch and record images of the resultant species in real time. Of particular relevance to the aim of the work described here is the fact that TEM experiments are carried out using conditions comparable to those found in the ISM; the microscope has a vacuum chamber pressure of about 10^{-12} mbar and, rather than UV photons, high energy electrons can be used to initiate transformations. As previously stated, it has been shown by Chuvilin *et al.* that under these conditions graphene flakes can undergo transformations that ultimately result in the formation of fullerene molecules.[23] In this study irradiation by the e-beam of TEM was carried out on discrete PAH molecules rather than non-uniform flakes of graphene in order to initiate and monitor transformations of these astrochemically relevant molecules, and hence reveal processes, including fullerene formation, that occur. In these experiments, the energy of electrons in the e-beam was 100 keV, which is sufficient to remove hydrogen atoms from PAHs[29] and promote rearrangement of carbon atoms, while monitoring these induced transformations as they are occurring.

3.3.1 E-beam irradiation-induced transformations of PAHs

TEM was carried out on four separate PAH molecules: anthracene, pyrene, perylene and coronene. These molecules were supported on graphite flakes in order to dissipate any ionisation and heating effects caused by the e-beam. Samples were irradiated by the e-beam in TEM for approximately 30 minutes and images taken periodically at intervals of 1.5 minutes so as to view the transformations that occur within the sample over time. Under these conditions, chemical transformations are driven by the kinetic energy of the e-beam transferred directly to the atoms within the molecules.

All experiments were performed using an accelerating voltage of 100 kV, at which incident electrons hitting the sample have a kinetic energy of 100 keV. At this energy and dose rate (~ 10^9 e^- nm^{-2} s^{-1}), the knock-on damage experienced by the PAH sample leads predominantly to the ejection of all of the hydrogen atoms from the molecule.[29] The result of the ejection of H atoms is that the PAH molecules are left with very reactive carbon radical sites at their edges; these dehydrogenated PAH structures react very quickly with each other, *via* dimerisation or cross-coupling reactions, to create new C-C bonds culminating in the formation of PAH aggregates and 'oligomers'. These can be thought of as larger PAH molecules, or as small graphene-like flakes. The formation of these oligomeric species is seen to occur for all four PAH samples, as can be seen in Figure 3.2, Figure 3.3, Figure 3.4 and Figure 3.5. In each of these figures, the initial frame of the time series shows no defined structures, whereas in the final frame well-defined shapes with dark, high-contrast edges can be seen, indicating discrete molecular species. These species increase in size over the duration of the experiment (Table 3.1), suggesting addition to, rather than fragmentation of, the original molecule; hence, this supports the idea of growth and formation of PAH 'oligomers'.

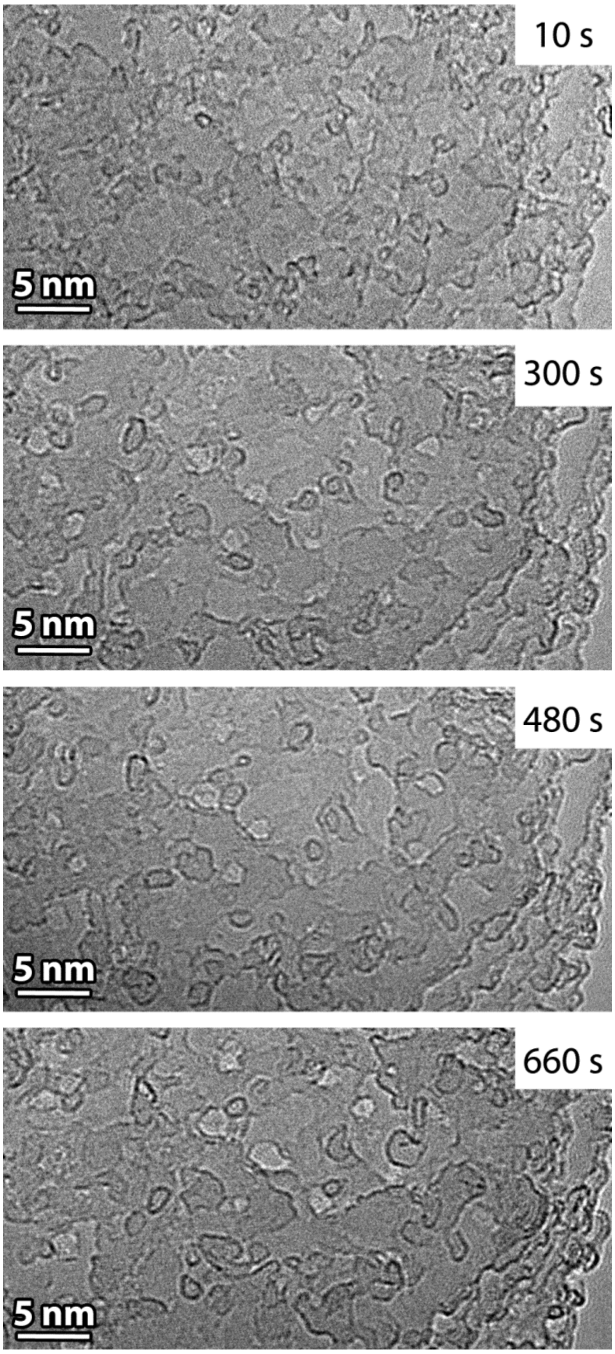

Figure 3.2. TEM micrographs showing the evolution of PAH oligomers during the irradiation of anthracene with a 100 keV e-beam.

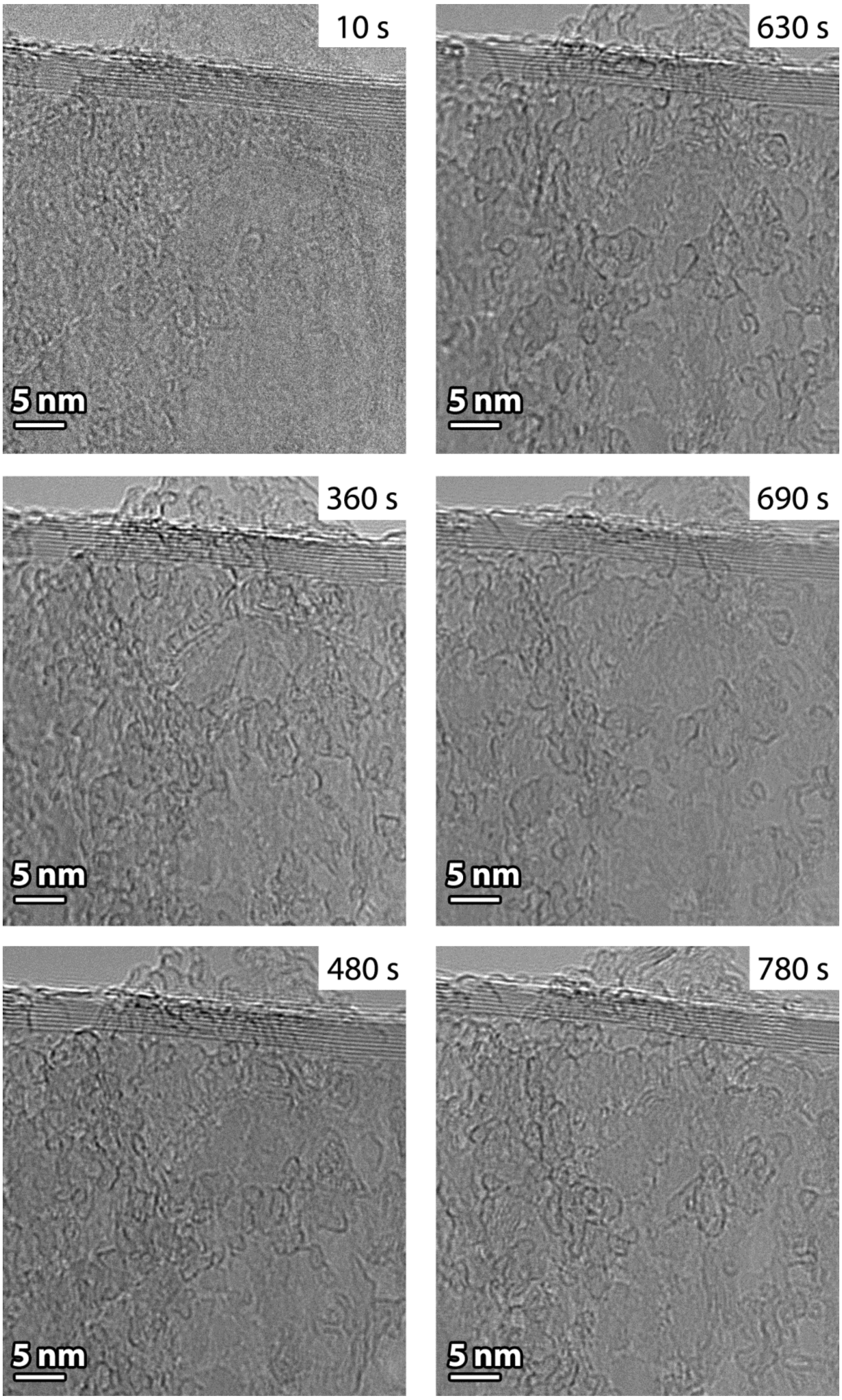

Figure 3.3. TEM micrographs showing the evolution of PAH oligomers during the irradiation of pyrene with a 100 keV e-beam.

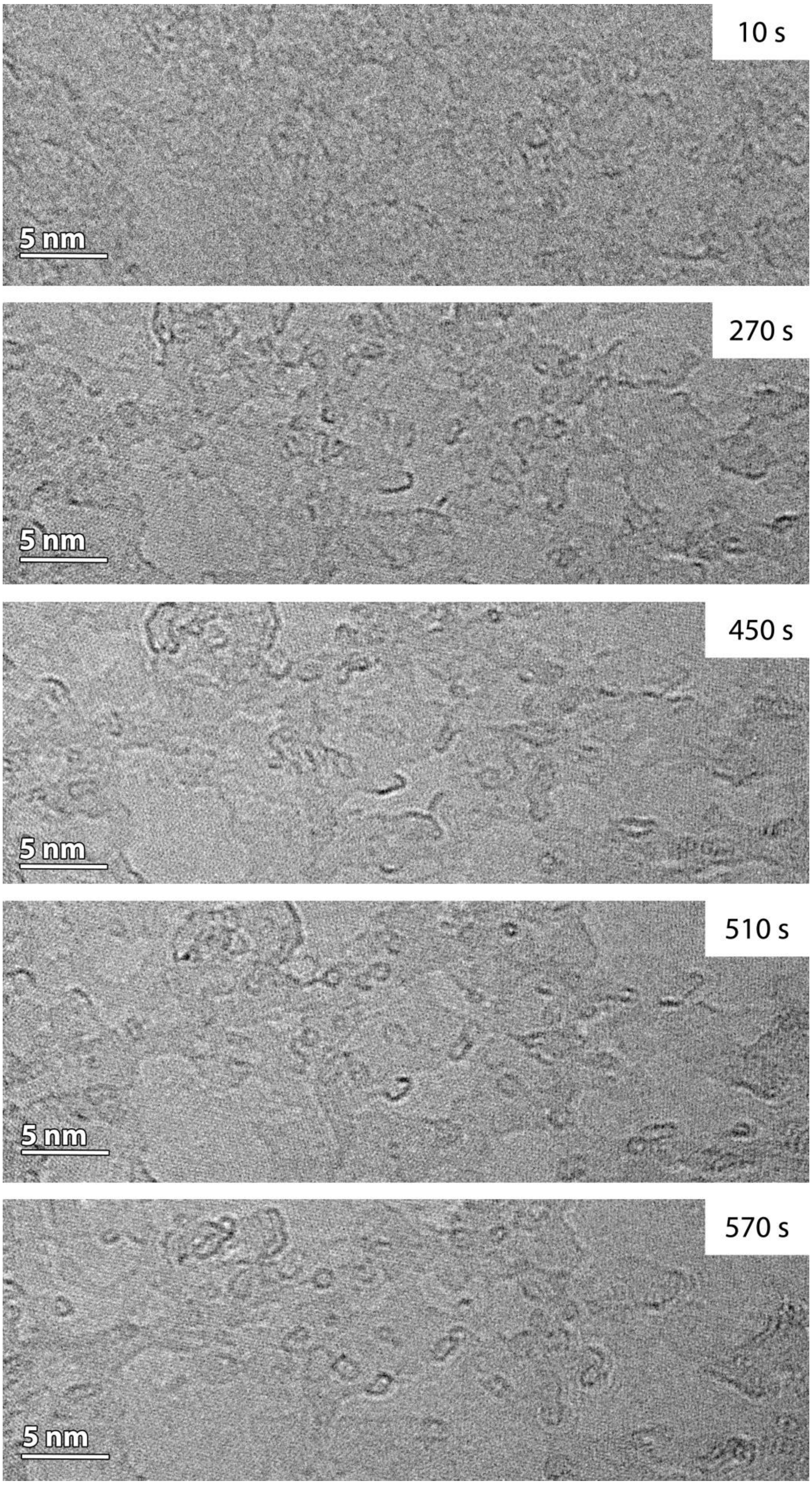

Figure 3.4. TEM micrographs showing the evolution of PAH oligomers during the irradiation of perylene with a 100 keV e-beam.

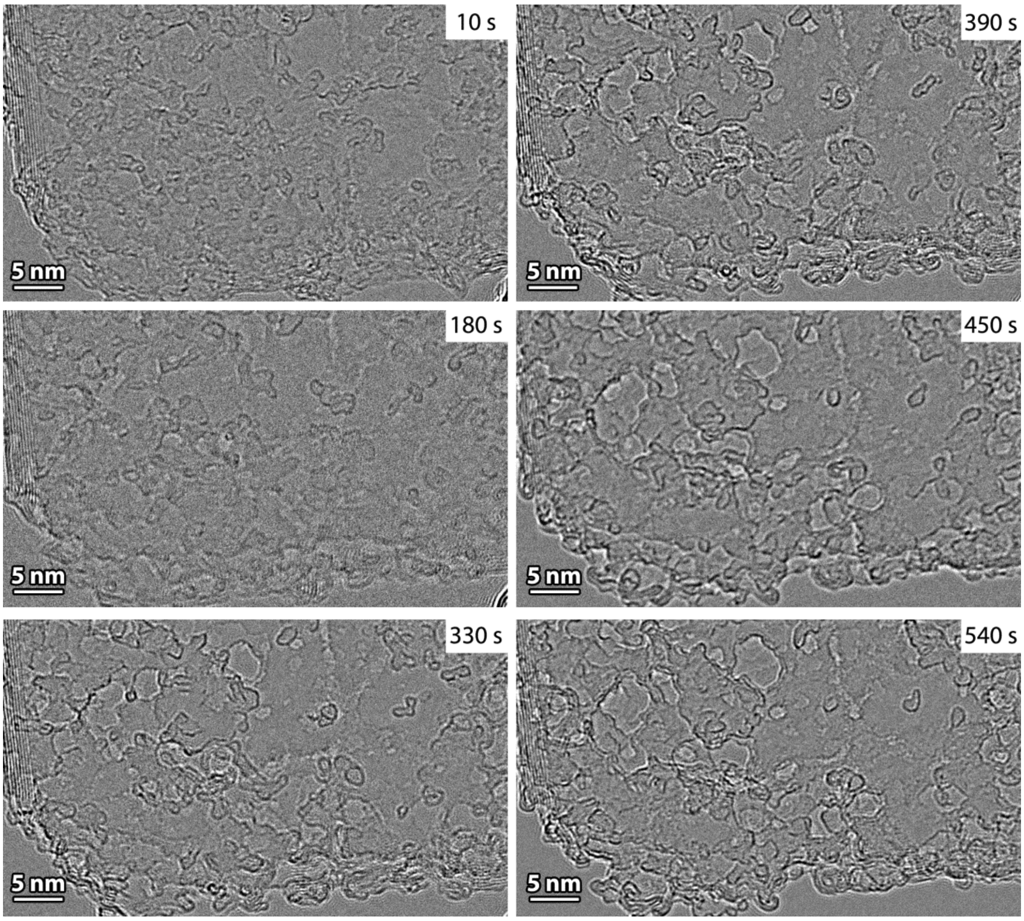

Figure 3.5. TEM micrographs showing the evolution of PAH oligomers during the irradiation of coronene with a 100 keV e-beam.

Table 3.1 shows the average sizes of a representative sample of oligomers at the beginning and end of each time series. These were calculated by selecting a number of shapes from the first and final frames of each series, measuring the largest distance across each, and calculating the mean of the values measured. It is notable that while there is an increase in size in each case, supporting the idea of growth and formation of oligomeric species, the increase is not always as large as might be expected. If a PAH ‘oligomer’ has formed from two individual molecules, for example, an increase in size of 100 % would be expected and this is clearly not seen. There are two possible explanations for this result. Firstly, the initial frame captured from the time series is not likely to be entirely representative of a sample of individual PAH molecules as the sample is exposed to the e-beam for a short period of time during the focussing of the beam and before the first image is recorded. During this time the PAH molecules are likely to have started to undergo transformations. Indeed, the average size measured in the first frame in the case of pyrene is measured as ~ 1.8 nm whereas the size of a single molecule of pyrene is closer to ~ 0.7 nm, suggesting that the species observed had already begun to 'grow' under the e-beam exposure. Starting from a larger size than that of the individual PAH molecule would account for a smaller overall increase in size over time. Additionally, the smaller-than-expected size increase could be explained if the oligomer structures, once formed, 'curled' at their edges. This would happen if, for example, one or more five-membered rings formed at the edge of the structure causing a curvature at those positions and lifting the edges out-of-plane; the projected image obtained of one of these molecules would then appear smaller than the molecule actually is, suggesting, therefore, that the formed species are only marginally larger than the original PAH molecules. A similar effect is seen in the experimental and theoretical investigations into the formation of fullerenes from graphene flakes,[23, 30] in which intermediate species with curved edges can be seen as shapes that are smaller than the original graphene flake, before finally forming the fullerene molecule.

Table 3.1. Average sizes of PAH 'oligomer' shapes in the first and final frames taken during e-beam exposure and the corresponding percentage increase.

	Average size (nm)		
Molecule	First frame	Final frame	Percentage increase
Anthracene	1.06	1.44	36 %
Pyrene	1.76	1.81	3 %
Perylene	1.01	1.11	10 %
Coronene	1.21	1.92	59 %

During the course of e-beam exposure, the influence of the e-beam on the molecules and oligomers is evident due to the constant changes in the shapes of the species that are observed. This is seen in Figure 3.2 – Figure 3.5, where the evolution of shapes can be seen over time for all PAHs. As a specific example, Figure 3.6 shows the change in shape of one of the observed structures, resulting from the irradiation of coronene, over time. For illustrative purposes the structures of a number of coronene molecules are depicted over the TEM micrograph in order to visualise shapes seen in the micrograph as individual molecules and oligomers.

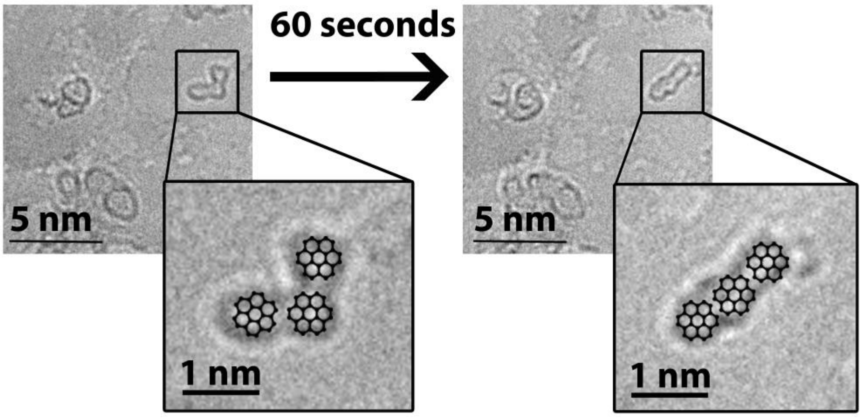

Figure 3.6. HRTEM micrographs showing the evolution of PAH oligomers, resulting from the irradiation of coronene, over a time period of ~ 60 s. As a guide, coronene structures are depicted over the micrographs in the zoomed-in inserts.

Towards the end of the e-beam exposure period, PAH oligomers formed as a result of transformations within the sample are seen to be stable, demonstrated by their long lifetime under the e-beam. This stability of the final structures likely contributes to the apparent ease with which oligomer formation occurs. There are a number of published examples in which PAH molecules are seen to polymerise in this way under the electron beam in TEM experiments,[31-33] and the reason for such transformations may be due to the atomic structure of this class of molecules. For example, the transformation of coronene to dicoronylene (structures given in Figure 3.7) may happen on the coming together of two coronene molecules, having ejected one or more hydrogen atoms and so containing one or more edge carbon radicals – the driving force being the formation of a new stable, 6-membered ring between the two entities (shown in red in Figure 3.7), and the overall conservation of planarity and aromaticity in the final molecule. In this way, it can be seen how the bottom-up construction of larger PAHs, or PAH oligomers, may be a facile process under these irradiative conditions, similar to those found in the ISM.

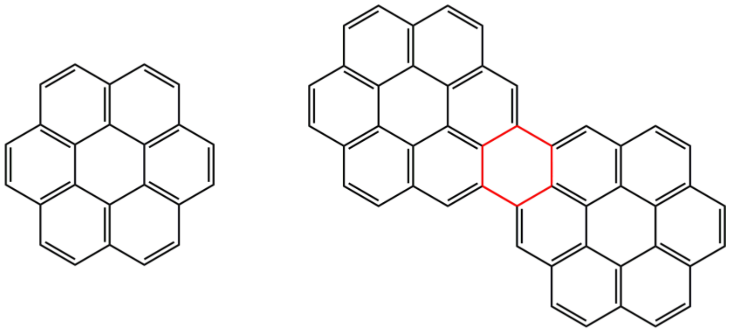

Coronene, $C_{24}H_{12}$

Dicoronylene, $C_{48}H_{20}$

Figure 3.7. Structures of coronene and dicoronylene. The new 6-membered ring linkage, formed if two molecules of coronene came together to form dicoronylene, is shown in red.

Following prolonged e-beam exposure, a number of examples are seen in which PAH oligomers appear to have ‘rolled’ up to form fullerene type structures, similar to the process operating in the work by Chuvilin *et al.*[23] Fullerenes are seen in TEM as high-contrast, well-defined circles; they are stable to e-beam exposure but are seen to move or ‘roll’ on the graphene-like surface. This is due to the smaller surface area of the fullerene in contact with the substrate on which it resides, when compared with a planar PAH molecule or oligomer, resulting in weaker van der Waals interaction between the fullerene and the surface. Figure 3.8 shows an example of a fullerene structure formed during the e-beam irradiation of coronene. When measured, the structure is seen to have a diameter of ~ 0.8 nm, which is comparable to the diameter of C_{60}. This demonstrates formation of C_{60} that begins with discrete, individual PAH molecules each containing fewer than 60 carbon atoms, representing a mechanism that must include, at least in part, an initial build-up or growth of molecules. It is important to note that e-beam irradiation of control samples containing only blank graphite flake substrates showed no evidence of the formation of oligomers or C_{60} (Figure 3.9), providing additional support for PAHs as the sole precursors to fullerene formation in these experiments.

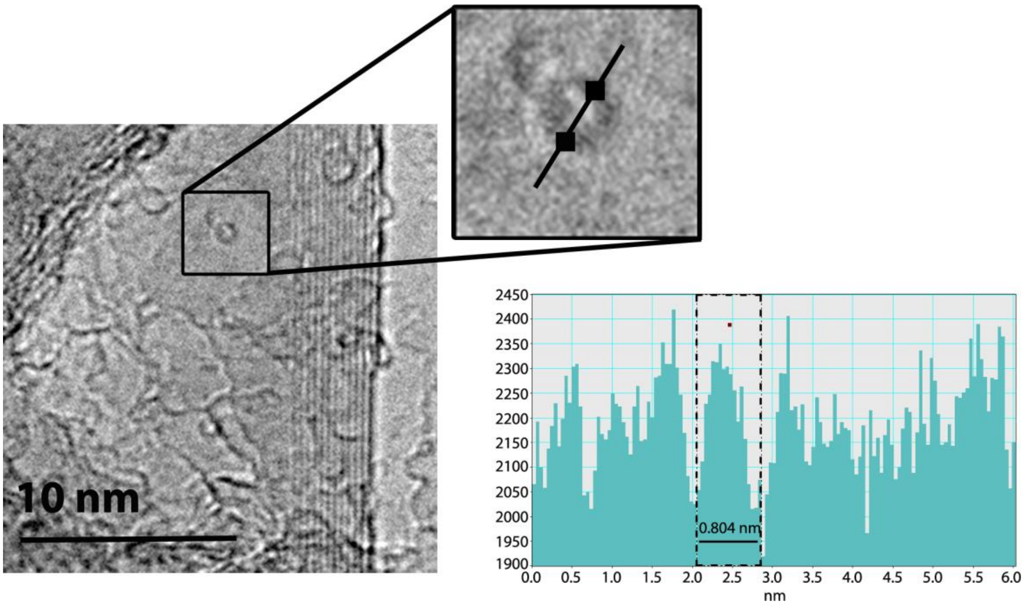

Figure 3.8. HRTEM micrograph (left) showing an example of a fullerene structure (see zoomed-in region), formed as a result of prolonged e-beam irradiation of coronene. Line profile plot (right) showing the structure to have a diameter comparable to that of C_{60} (0.8 ± 0.1 nm).

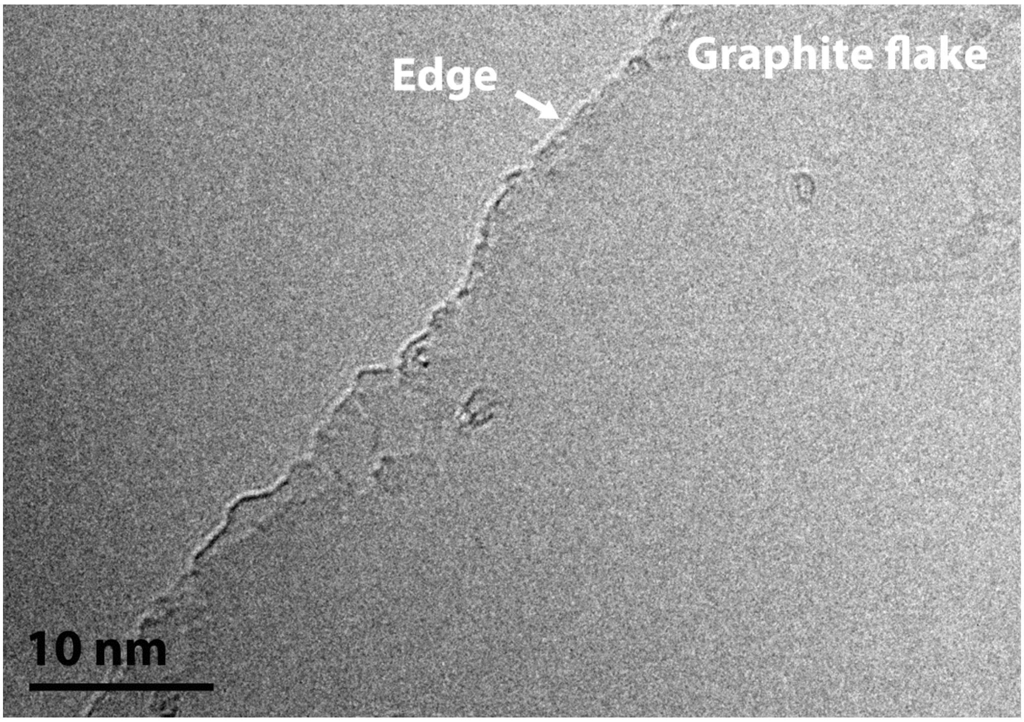

Figure 3.9. TEM micrograph of blank graphite flake substrate.

It should be noted that in theoretical studies carried out by Santana *et al*.[30] calculations of the time evolution of a graphene flake under a 200 kV electron beam show the complete decomposition of the flake within approximately 10 minutes (see their Figure 2). This suggests that under the conditions specified in this study, the species being observed may also be decomposing within their time under the e-beam. The time series included in Figure 3.2 - Figure 3.5 only include micrographs from the first 10 – 15 minutes of the irradiation period, and so the first few images of each time series may show species that have not yet decomposed, and that have undergone oligomerisation/aggregation. However, due to the ease with which these species may decompose under the e-beam, caution must be taken not to over-interpret the images obtained.

3.4 UV laser irradiation of PAHs using MALDI-TOF MS

Many processes expected to occur in space are initiated by the absorption, by molecular species, of UV photons, usually from a nearby star. Hence, to continue the investigation into the transformative processes of PAHs that may result in fullerene formation, experiments using a source of UV photons were undertaken. MALDI-TOF MS is a technique which is traditionally used to characterise molecules and identify the mass of molecular structures, and causes little damage to the sample as it uses a low UV laser fluence to ionise the molecular species. However, if the fluence of the UV laser is increased, it can be used as a source of UV photons capable of initiating transformations within the sample. To illustrate this, Figure 3.10 shows mass spectra resulting from the irradiation of a sample of pyrene at different values of laser fluence; at low fluence the mass peak for pyrene is seen (m/z = 202), whereas at higher laser fluence higher mass species form and are detected. This technique was therefore used to irradiate and initiate transformations within the PAH samples, in a similar way to the previously discussed TEM experiments, and to identify the resultant species which were ionised and detected using the TOF detector.

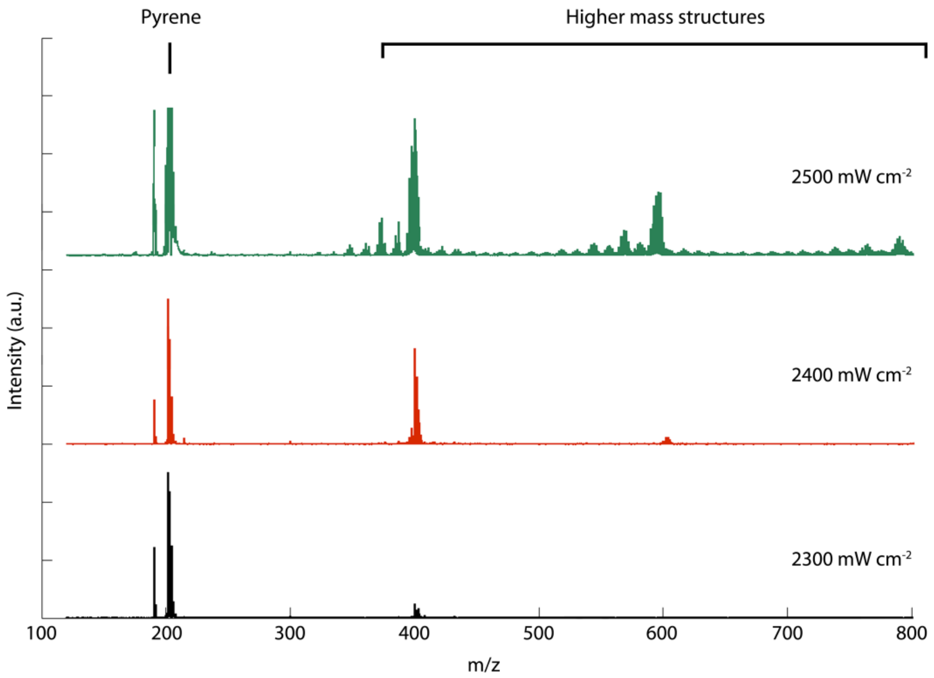

Figure 3.10. Mass spectra resulting from irradiation of pyrene using the UV laser of MALDI-TOF MS at different values of laser fluence; 2300 mW cm^{-2} (bottom), 2400 mW cm^{-2} (middle) and 2500 mW cm^{-2} (top). Increasing the laser fluence results in the detection of higher mass species, indicating their formation *via* laser-induced transformations within the initial sample.

3.4.1 Products detected

A control experiment was carried out in which the UV laser of the MALDI-TOF instrument was fired at high laser fluence (~ 2600 mW cm^{-2}) at the MALDI target plate containing no sample. This was for the purpose of ruling out C_{60} or any other formed species originating from the plate that supports the sample, rather than from the sample itself. The resultant mass spectrum is given in Figure 3.11, which shows a low-intensity spectrum containing one major peak at *m/z* = 360. The exact identity of this peak is unclear; however, the cause of the peak does not appear to be carbon-based due to the absence of a C^{13} isotope pattern. This means that when experiments are carried out on PAH samples, the products detected can confidently be attributed to structures originating from the sample and not from the target plate.

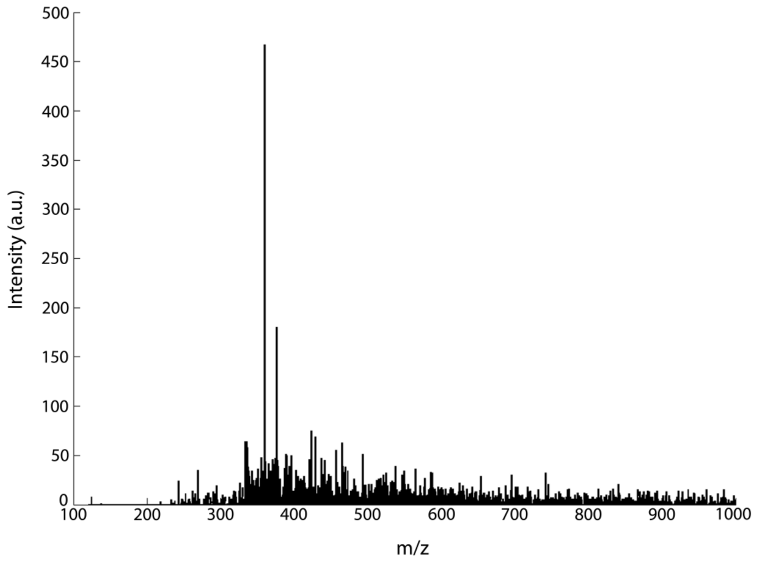

Figure 3.11. Mass spectrum from the MALDI-TOF MS of a blank MALDI target plate. There is a low-intensity peak at *m/z* = 360, and no C_{60} (*m/z* = 720) is detected.

A thin layer of each of the four PAH samples was drop-cast onto a stainless steel sample holder, inserted into the vacuum chamber (10^{-7} mbar) and irradiated using the Nd:YAG laser (355 nm, 5 ns) of the MALDI-TOF mass spectrometer. The laser fluence was varied between ~ 2000 and ~ 2600 mW cm^{-2}, and in all cases experiments carried out at low laser fluence showed the presence of the corresponding molecular ion peaks only (as illustrated in Figure 3.10) indicating simply that the PAH molecules were ionised and that the sample contained no additional PAHs or contaminants. At higher laser fluence, the mass spectra revealed formation of higher mass structures. These are proposed to have formed as a result of hydrogen atom loss achieved through the increased energy supplied by the laser, followed by the formation of new C-C bonds, driven by the minimisation of carbon radical sites in the positions of the absent hydrogen atoms. Specifically, major peaks are seen at two or three times the mass of the individual PAH, minus a small number of mass units (4, 8, 12, or 18). These peaks are assigned to PAH oligomer structures which are thought to have formed through C-C bond formation following the loss of a number of hydrogen atoms – this hydrogen atom loss accounting for the mass unit deficit that is observed. Similar irradiation-induced formation of PAH oligomers, specifically those of coronene, has been reported,[34] supporting the assignment of peaks in these experiments. Figure 3.12, Figure 3.13, Figure 3.14 and Figure 3.15 show the resultant mass spectra following high laser fluence (~ 2600 mW cm^{-2}) irradiation of anthracene, pyrene, perylene and coronene, respectively, and include the proposed structures of the oligomers formed, above their corresponding mass peaks. Descriptions and *m/z* values of the PAH molecules and oligomers are given in Table 3.2.

Table 3.2. *m/z* values and assignments of the main peaks seen in Figure 3.12 – Figure 3.15 along with descriptions of the predicted structures, shown pictorially in the aforementioned figures.

PAH	*m/z* of peak	Assignment	Description
Anthracene	178	$C_{14}H_{10}$	Molecular ion.
	352	$C_{28}H_{16}$	‘Dimer’ structure containing two anthracene units each having lost two hydrogen atoms.
Pyrene	202	$C_{16}H_{10}$	Molecular ion.
	400	$C_{32}H_{16}$	‘Dimer’ structure containing two pyrene units each having lost two hydrogen atoms.
	598	$C_{48}H_{22}$	‘Trimer’ structure containing three pyrene units with an overall loss of eight hydrogen atoms.
	790	$C_{64}H_{22}$	Condensed ‘tetramer’ structure containing four pyrene units with an overall loss of eighteen hydrogen atoms.
Perylene	252	$C_{20}H_{12}$	Molecular ion.
	500	$C_{40}H_{20}$	‘Dimer’ structure containing two perylene units each having lost two hydrogen atoms.
	720	C_{60}	C_{60} fullerene.
	744	$C_{60}H_{24}$	Condensed ‘trimer’ structure containing three perylene units with an overall loss of twelve hydrogen atoms.
Coronene	300	$C_{24}H_{12}$	Molecular ion.
	596	$C_{48}H_{20}$	‘Dimer’ structure containing two coronene units each having lost two hydrogen atoms.
	720	C_{60}	C_{60} fullerene.
	888	$C_{72}H_{24}$	Condensed ‘trimer’ structure containing three coronene units with an overall loss of twelve hydrogen atoms.

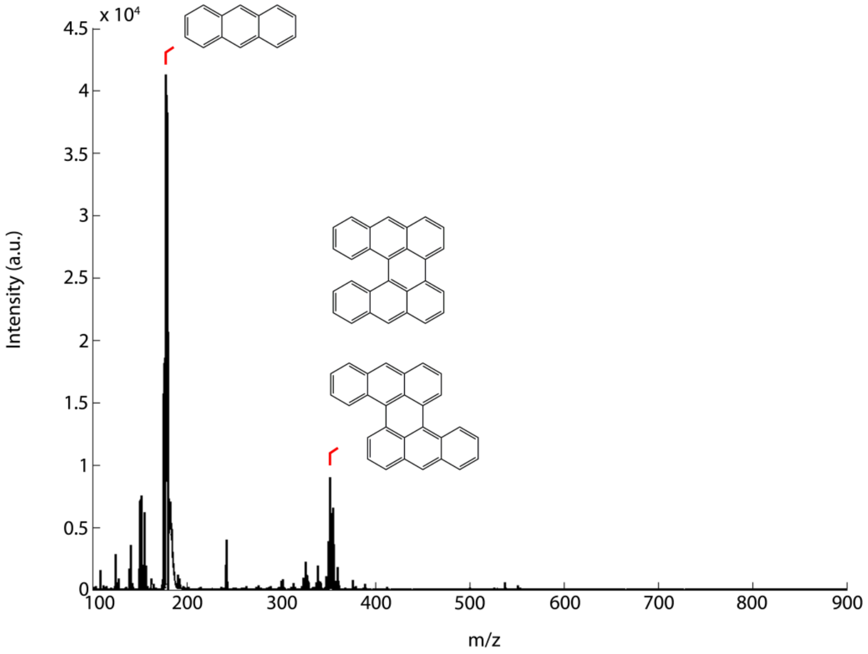

Figure 3.12. Mass spectrum resulting from UV irradiation of anthracene at a laser fluence of ~ 2600 mW cm^{-2}. Proposed structures of the species formed are given above the corresponding mass peaks.

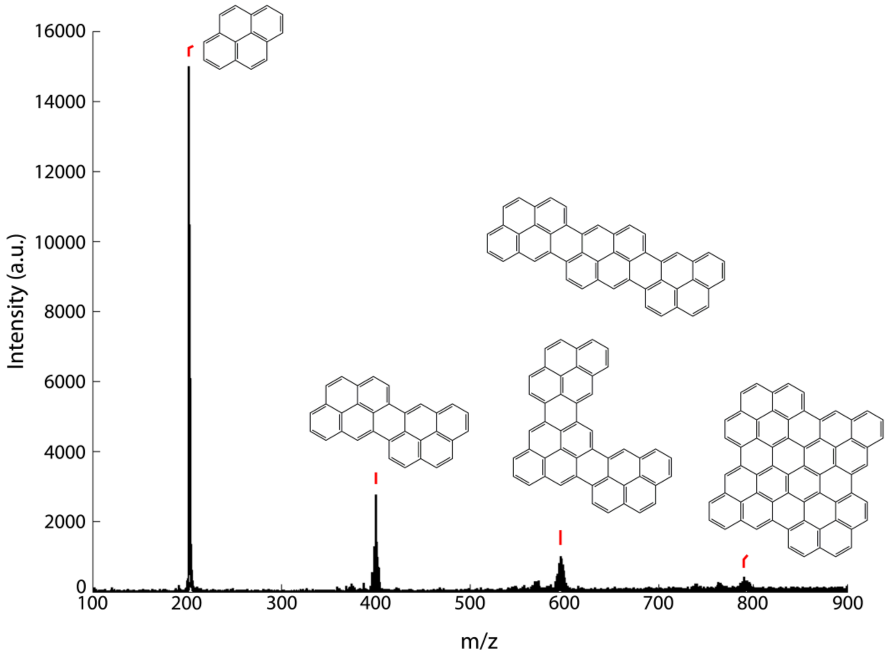

Figure 3.13. Mass spectrum resulting from UV irradiation of pyrene at a laser fluence of ~ 2600 mW cm^{-2}. Proposed structures of the species formed are given above the corresponding mass peaks.

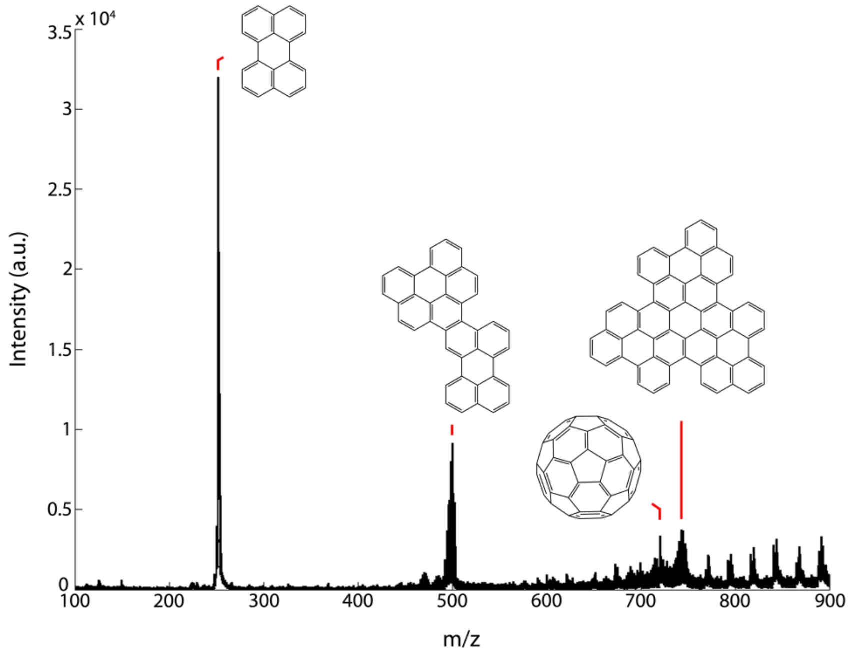

Figure 3.14. Mass spectrum resulting from UV irradiation of perylene at a laser fluence of ~ 2600 mW cm^{-2}. Proposed structures of the species formed are given above the corresponding mass peaks.

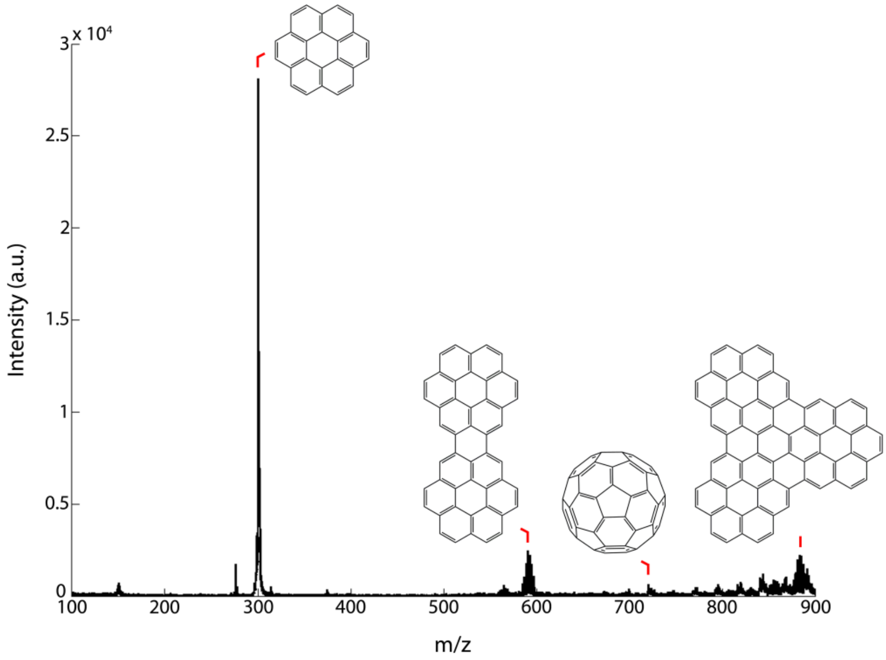

Figure 3.15. Mass spectrum resulting from UV irradiation of coronene at a laser fluence of ~ 2600 mW cm^{-2}. Proposed structures of the species formed are given above the corresponding mass peaks.

In addition to the formation of PAH oligomers, a peak can be seen at *m/z* = 720 in Figure 3.14 and Figure 3.15, corresponding to the detection of a molecule with the formula C_{60}. Figure 3.16 shows the mass spectrum resulting from the irradiation of coronene magnified to show only this peak, with comparison to an isotope pattern of C_{60}, calculated using ChemCalc;[35] good agreement is seen between the two. While there is no way to distinguish whether this peak arises from a flat C_{60} molecule or a fullerene cage, the latter is assumed due to its stability and formation under similar conditions during its discovery. This assumption having been made, these experiments demonstrate that C_{60} is being formed as a result of the irradiation of the sample PAH molecules.

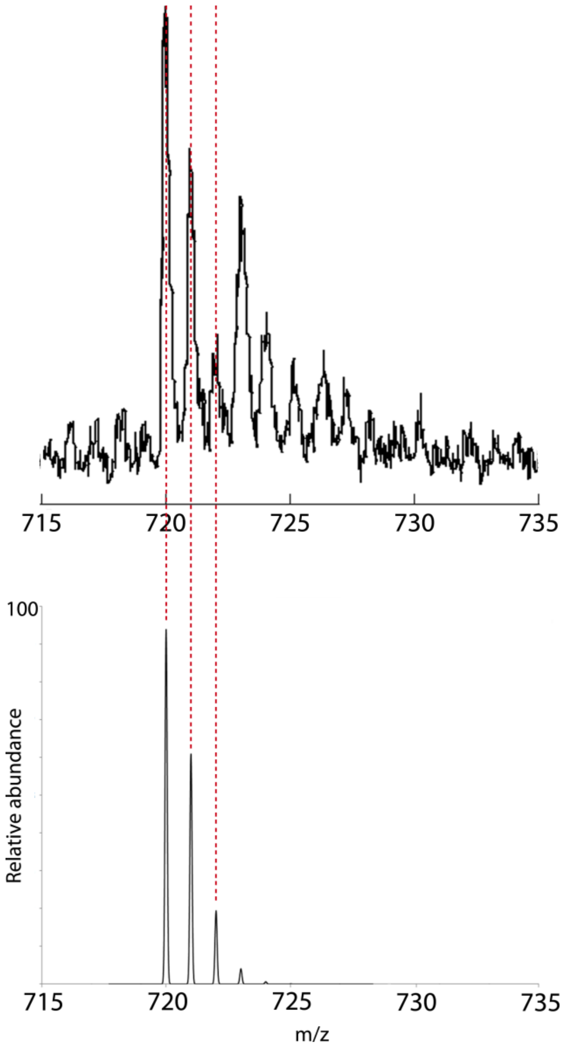

Figure 3.16. Experimental MS peaks near *m/z* = 720 resulting from the UV irradiation of coronene in MALDI-TOF MS (upper figure) compared with a calculated isotope pattern for C_{60} (lower figure), obtained using ChemCalc.[35]

Since the PAHs used contain fewer carbon atoms than the fullerene, and considering the seemingly facile formation of PAH oligomers in these experiments, it is probable that C_{60} formation occurs as a result of the shrinking of one of these oligomers containing sixty carbon atoms or more. This 'shrinking' can occur *via* the ejection of C_2 units and hydrogen atoms.[17] In this way, a mechanism can be proposed that can be thought of as 'bottom-up' followed by 'top-down', *i.e.* the building up of the initial PAH molecule to form oligomers, or larger PAHs, followed by the ejection of a number of atoms and the rearrangement of bonds to finalise the fullerene structure. This is in agreement with the results from Section 3.3.1, in which the formation of C_{60} from PAHs in TEM also suggested the necessity for the building up, or growth, of larger molecules as part of the overall mechanism.

It is noteworthy that C_{60} is only seen in the cases when starting from perylene and coronene, and that there is no evidence for C_{60} formation from anthracene or pyrene precursors. This suggests that there is a dependence of fullerene formation on the size or shape of the initial PAH molecule and/or the oligomers that are formed. It may be thought that C_{60} formation would not occur if oligomers of sixty carbon atoms or more were not formed, and this appears to be the case for anthracene; the largest molecule detected in the mass spectrum resulting from the irradiation of anthracene corresponds to $C_{28}H_{16}$. It would be logical to infer that if no larger species are formed then they cannot 'shrink' down to form the fullerene structure. However, this does not seem to hold for the case of pyrene, in which a molecule is detected at m/z = 790, corresponding to $C_{64}H_{22}$ (pyrene 'tetramer', Figure 3.13). If C_{60} formation were solely dependent on oligomers having more than sixty carbon atoms, then detection of the C_{60} would be expected in the case of pyrene also. To see if there are any clues in the structural features of the oligomers as to this apparent selectivity, Figure 3.17 shows the trimers of perylene and coronene together with the tetramer of pyrene. Comparing the three molecules, it is not immediately obvious whether there are any features for the two trimers, which do go on to form C_{60}, that distinguish them from the pyrene tetramer, which shows no evidence of leading to fullerene formation. However, it may be noted that, considering the symmetry of the molecules, both of the PAH trimers have a C_3 axis of rotation perpendicular to the plane of the molecule, whereas the pyrene tetramer has a C_2 axis of rotation in this position (Figure 3.17 a). It is interesting that in other examples of C_{60} synthesis,[20, 36] the molecular precursors used also have a C_3 axis of rotation, although the possible significance of symmetry is not commented on. The importance of this symmetry element is not clear, but it is notable as a feature that connects the two PAHs that are seen to form C_{60}.

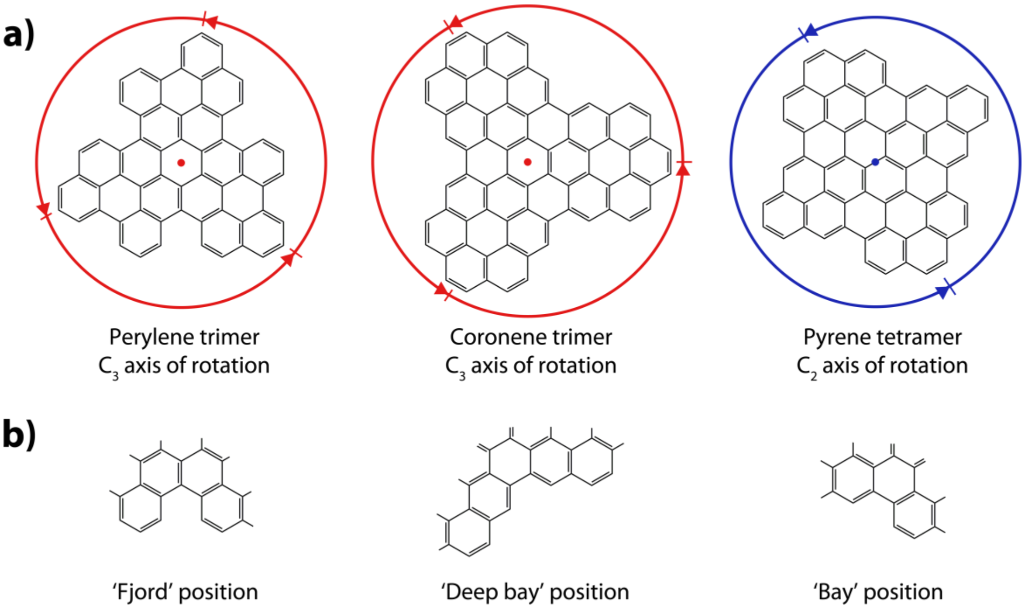

Figure 3.17. Structures of the trimers of perylene and coronene and the tetramer of pyrene. a) A red dot indicates a C_3 axis of rotation perpendicular to the plane of the molecule, the red arrows demonstrating the three associated rotations. The blue dot indicates a C_2 axis of rotation perpendicular to the plane of the molecule and the blue arrows indicate the two associated rotations. b) Types of edge structure seen in each molecule are isolated and labelled as 'fjord', 'deep bay' or 'bay'.

At a more intuitive level, when comparing the three structures in Figure 3.17 it is seen that the pyrene tetramer is more 'compact' in its structure, and has a stronger similarity to a stereotypical graphene sheet. Its edges are straighter and are closer to single rows of six-membered rings. This is demonstrated in Figure 3.17 b), which shows edge structures for each molecule – namely 'fjord' positions seen in the perylene trimer, 'deep bay' positions in the coronene trimer, and 'bay' positions in the pyrene tetramer. With this in mind, it may be that it is simply more difficult to introduce curvature into the pyrene tetramer than for the other two molecules; for example, temporary bending or even bond formation at the fjord or deep bay positions would bring distant portions of the PAH close together, which could lead to the formation of additional bonds and impose curvature. It is not as easy to imagine this process occurring in the more compact, rectangular, pyrene tetramer.

3.4.2 Mechanism of fullerene formation

Following the hypothesis that the C_{60} detected in the UV irradiation of coronene or perylene is formed as a result of the shrinking of oligomers containing sixty carbon atoms or more, the mass spectra corresponding to these oligomers were examined more closely in order to determine the exact masses and therefore structures of these molecules; in doing so, detailed mechanistic steps linking the oligomers with the final fullerene structure could be explored.

Figure 3.18 shows the mass spectrum resulting from the irradiation of perylene using MALDI-TOF MS, along with proposed steps involved in the formation of C_{60}. The mass spectrum shown is for the region m/z = 700 – 760, which includes a peak at m/z = 720, corresponding to C_{60}, in addition to a range of other peaks, with the most intense falling at m/z = 744. This peak is assigned to the perylene trimer structure, labelled ① in Figure 3.18, which has an m/z value of 744 and is proposed to form as detailed in Section 3.4.1, *via* H loss and C-C bond formation. Additional peaks that are seen and labelled in the mass spectrum occur at m/z = 742, 740 and 738. Each of these is two mass units less than the previous one, which can be interpreted as a difference of two hydrogen atoms between each of the structures. The molecules that are proposed to correspond to these peaks are shown in Figure 3.18 and are labelled ②, ③ and ④, respectively. It can be seen in the figure that these structures result from the loss of two hydrogen atoms, at so-called ‘fjord’ positions, followed by the formation of a new C-C bond, where this is driven by the instability of the carbon radicals that result from the initial hydrogen loss. It can be seen that losing these particular H atoms leaves the molecule predisposed to form a five-membered ring at that position. The formation of pentagons within the structure is significant as fullerene molecules contain twelve pentagons in total. Indeed, the fullerene formation from a graphene flake reported by Chuvilin *et al.*[23] showed that it was the formation of five-membered rings at the edge of the flake that was key in initiating the ‘zipping’ of the flake to form the 3D fullerene cage, due to its introduction of curvature in the previously planar species. Recently, it was reported that DFT calculations of fully dehydrogenated PAHs showed that, when removing the hydrogen atoms of a PAH containing a fjord region, the fjord region would close up and form a five-membered ring.[37] This provides significant support for the first stages of the mechanism given in Figure 3.18.

In order to continue from structure ④, in Figure 3.18, to the fullerene cage, steps are required that involve the loss of hydrogen atoms, the formation of new C-C bonds, and the rearrangement of a number of bonds to achieve the formation and migration of pentagons. The final mechanistic steps in Figure 3.18 show examples of the processes suggested to be occurring to generate the fullerene. Once molecule ④ has been reached, there are no remaining ‘fjord’ positions in the structure. However, if H atom loss occurred at the ‘bay’ positions indicated in the figure, subsequent C-C bond formation would result in a strained four-membered ring. To stabilise this, a C-C bond has been highlighted that could undergo a Stone-Wales rearrangement[38] to yield the structure labelled ⑤. In this structure, there are two additional positions at which the sequence of H-loss, C-C bond formation and Stone-Wales rearrangement can occur. The result of completing these steps at both positions is structure ⑥.

The structure ⑥ in Figure 3.18, following the previous steps, contains three seven-membered rings which are not present in a C_{60} fullerene molecule. Three bonds are highlighted within the structure that could undergo Stone-Wales rearrangements in order to yield a structure containing only five- and six-membered rings, ⑦. Structure ⑦ is shown in side profile also, and is seen to have a curved, bowl-like shape which can then ‘zip up’ to form the C_{60} detected in the mass spectrum (⑧).

It is not yet fully established that the steps given in Figure 3.18 constitute the exact route between the perylene trimer and C_{60} that are detected in the MALDI-TOF MS experiments; nor can the exact order of the steps be determined, especially when considering the suggested sequence of H-loss, C-C bond formation and Stone-Wales rearrangement that occurs a number of times between ④ and ⑦. However, C_{60} is an extremely stable molecule due to its lack of edges and it is feasible that the loss of one or more hydrogen atoms from the edge of a PAH oligomer, and the subsequent C-C bond formation and rearrangements, would initiate a thermodynamically-driven process the end result of which is formation of the very stable molecule, C_{60}.

It is worth noting that the fullerenes that are formed and are detected may not adhere perfectly to the 'isolated pentagon rule' (IPR) – that is, no two adjacent pentagons within the fullerene structure, all pentagons are surrounded by five hexagons. Due to the necessity for movement of pentagons within a structure to achieve an 'IPR perfect' fullerene, the energy cost may simply be too high and hence the probability of their formation is quite low. If fullerenes are being formed, but not in their most stable (*i.e.* IPR perfect) form, this could account for the relatively low intensity of the C_{60} peaks that are seen in the mass spectra (Figure 3.14 and Figure 3.15), compared with what might be expected based on the intensity of the C_{60} peak seen in the experiments that prompted the fullerene's discovery.[1]

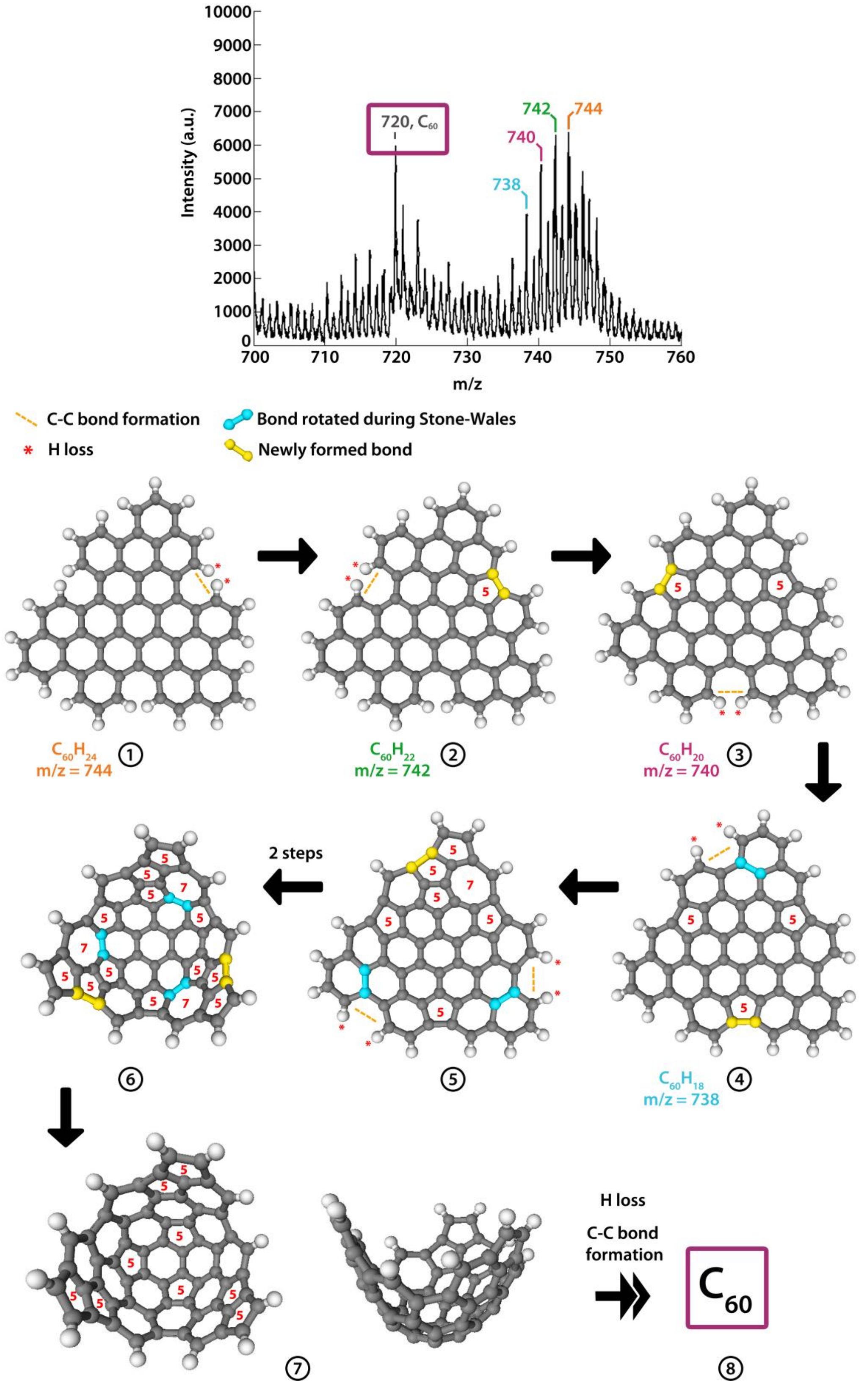

Figure 3.18. Section of the mass spectrum resulting from UV irradiation of perylene (top) and suggested mechanistic steps showing the transformation from the perylene trimer to C_{60}.

Figure 3.19 shows the mass spectrum and proposed mechanistic steps involved in the formation of C_{60}, following UV irradiation of coronene. The mass spectrum in this instance is of the region *m/z* = 700 – 900, in which the C_{60} peak at *m/z* = 720 can be seen. The coronene trimer, labelled ①, has an *m/z* value of 888 which is detected in the mass spectrum in addition to peaks at *m/z* = 886, 884 and 882. There are other seemingly significant peaks labelled that fall at *m/z* = 856 and *m/z* = 840. The fullerene C_{70} has an *m/z* value of 840, and so its detection in the mass spectrum indicates that this is the initial fullerene that is being formed from the coronene trimer, which is then going on to form C_{60} by ‘shrinking’ *via* the loss of C_2 fragments. This is supported by the detection of intermediate fullerenes from this process: C_{68}, C_{66}, C_{64} and C_{62}.

The structure of the coronene trimer differs from oligomers formed from perylene in that it has no ‘fjord’ hydrogen sites. However, peaks in the mass spectrum are again seen that are separated by two mass units, suggesting a difference of two hydrogen atoms between each of the responsible structures. It is proposed, as shown in Figure 3.19 structure ①, that the loss of hydrogen atoms in the bay positions of the trimer, followed by subsequent C-C bond formation and a Stone-Wales rearrangement, will result in structure ② which is assigned to the peak at *m/z* = 886. Structures ②, ③ and ④ demonstrate this process occurring three times in total, and can account for the peaks seen in the mass spectrum at *m/z* = 886, 884 and 882 respectively. The next prominent peak in the mass spectrum is seen at *m/z* = 856, which corresponds to a molecule with the chemical formula $C_{70}H_{16}$. This differs from structure ④ in Figure 3.19 by a C_2H_2 group. It is proposed that if dissociation to form a C_2H_2 fragment were to occur in the position indicated in structure ⑤, it would result in a pseudo-bay area in which, as before, C-C bond formation to minimise the C radical sites would result in a four-membered ring that could be stabilised through Stone-Wales rearrangement at the indicated position. The result of this sequence is structure ⑥, which is a candidate isomer for the mass spectrum peak seen at *m/z* = 856.

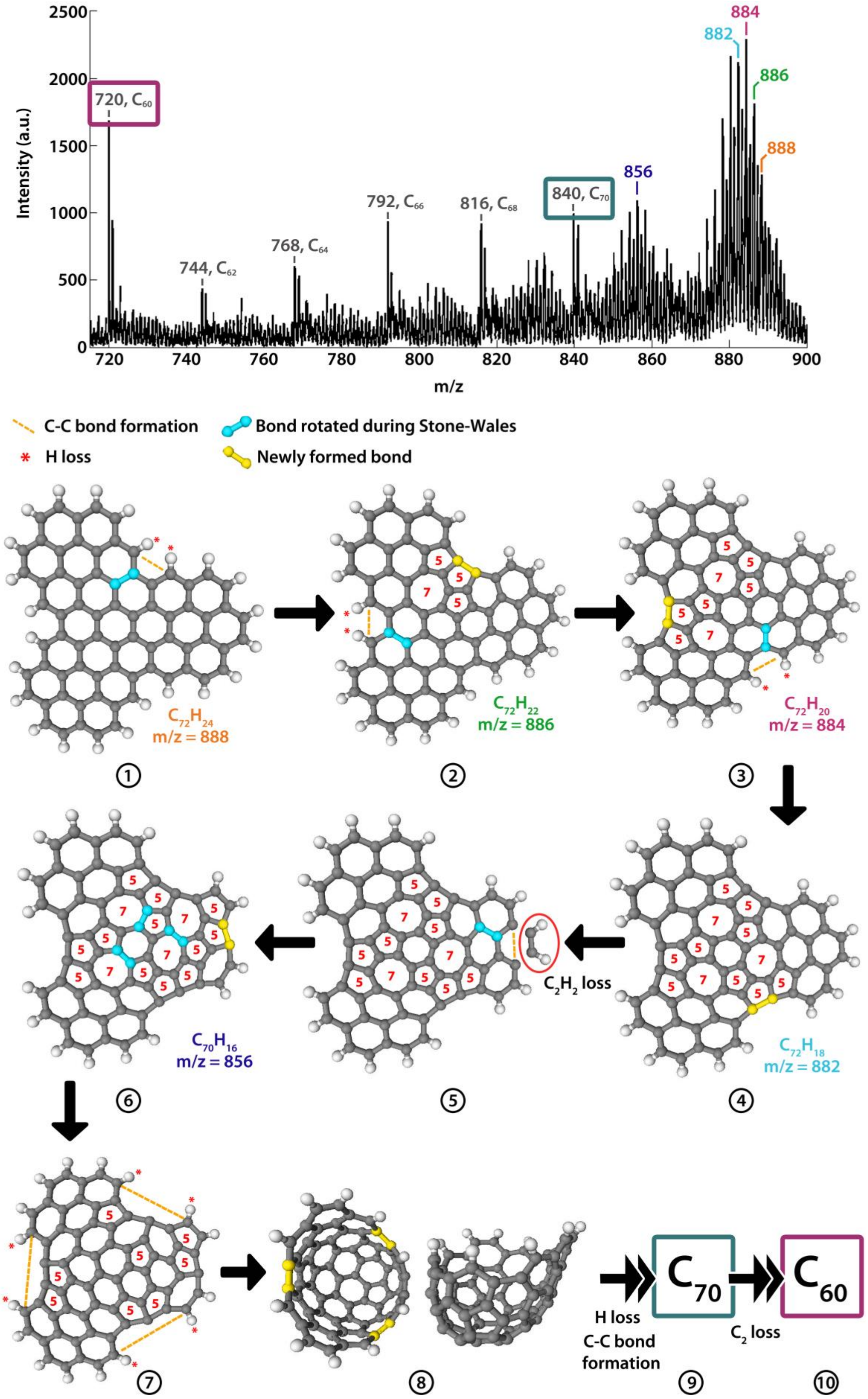

Figure 3.19. Section of the mass spectrum resulting from UV irradiation of coronene (top) and suggested mechanistic steps showing the transformation from the coronene trimer to C_{60}.

Highlighted in structure ⑥ are three bonds that if rearranged *via* a Stone-Wales mechanism would result in a molecule containing only five- and six-membered rings, labelled structure ⑦. Structure ⑦ contains 70 carbon atoms and in order to achieve the C_{70} fullerene structure, steps involving H atom loss, C-C bond formation and bond rearrangements would be required. One example of steps that could occur is shown in Figure 3.19 from structure ⑦ to ⑧, in which H-loss and C-C bond formation result in the formation of three new six-membered rings and the resultant structure ⑧ can be seen from its side profile to be curved in shape. It is expected that, driven by the formation of a low-energy fullerene molecule, structure ⑧ or similar will then continue to ‘zip’ up to form C_{70}, which could then go on to form C_{60}.

The suggested mechanisms given in Figure 3.18 and Figure 3.19 contain a number of steps that would require a high energy input. The Stone-Wales rearrangement – a process that involves the breaking and reforming of C-C bonds – is thought to have an activation barrier of approximately 9 eV in a graphite sheet[39] although this may vary depending on factors such as the position of the bonds undergoing the transformation and the strain or curvature in the structures. The laser used in the MALDI-TOF MS setup has a wavelength of 355 nm, meaning that photons have energy of approx. 3.7 eV. Clearly this value is lower than that required for Stone-Wales rearrangement; however, with the number of photons per laser pulse being of the order of 10^{14}, and with 200 pulses per experiment, it is feasible that a build-up of energy can occur such that these transformations take place readily as is evidenced by the detection of PAH oligomers and fullerenes seen in the mass spectra.

An experiment was carried out in which the number of laser pulses was reduced in the irradiation of coronene and of perylene, while the laser fluence was kept the same as for the main UV irradiation experiments (~ 2600 mW cm^{-2}). The resultant mass spectra were compared with those from experiments in which two hundred pulses were used, and the comparisons are given in Figure 3.20. In both cases, the mass spectra resulting from one laser pulse were less intense than those resulting from two hundred laser pulses, by about two orders of magnitude. In order to compare these results, the mass spectra seen in Figure 3.20 have been scaled to the same intensity of the main molecular ion peak of the 200-pulse mass spectra.

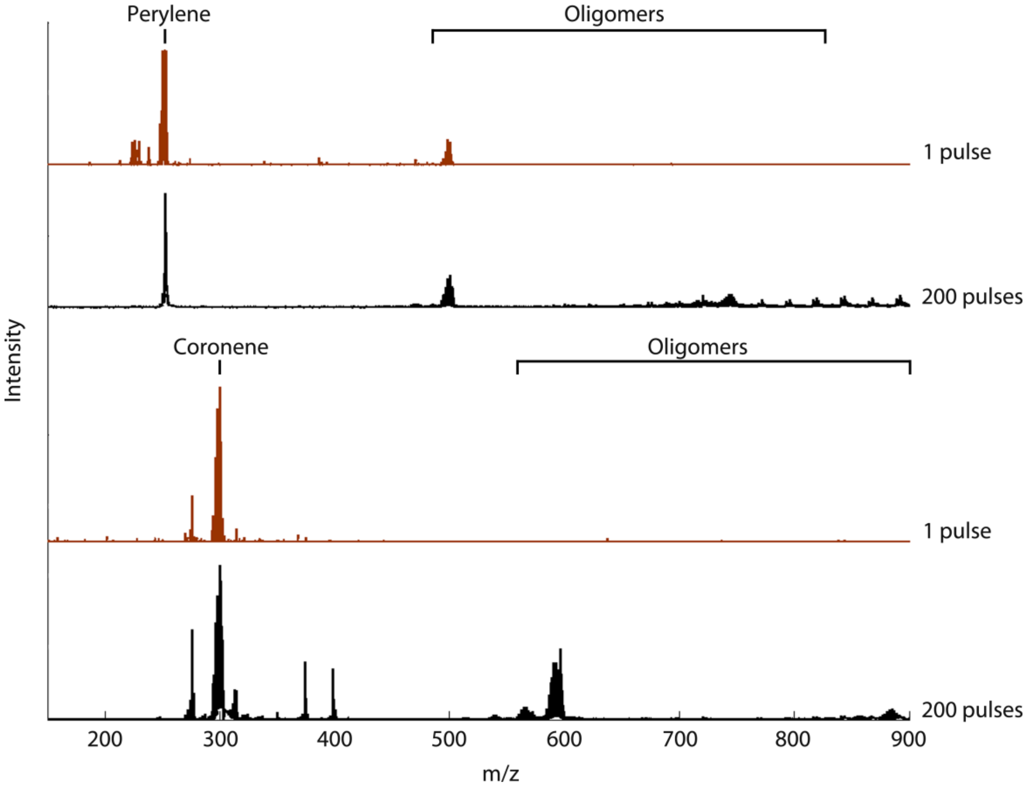

Figure 3.20. Mass spectra resulting from MALDI-TOF MS experiments on perylene (top) and coronene (bottom), comparing the results of one laser pulse with two hundred successive pulses, revealing the absence of formation of PAH oligomers with only one laser pulse. The molecular ion peak for each of the ‘1 pulse’ spectra has been normalised to that of the ‘200 pulse’ spectra by multiplying by a factor of approximately 100.

It can be seen that experiments carried out using two hundred laser pulses result in the formation of higher mass structures, as reported earlier in this Section. When the number of pulses was reduced to one, coronene is seen to no longer form any higher mass structures – only the coronene molecular ion peak was observed. In the case of perylene, the mass spectrum resulting from one laser pulse was found to include a small peak corresponding to the perylene dimer, but no further higher mass structures. These results confirm that the types of transformation suggested in this Section do require a high amount of energy, but that the cumulative energy supplied when more than one laser pulse is applied is sufficient to cause the necessary transformations for the structures to form that are then detected so abundantly in the mass spectra.

In an astrophysical context, the probability of a second photon hitting a molecule is incredibly low, although it is possible, given a large amount of time. The issue in determining the way in which a molecule will transform lies with the competing processes that may occur in the time between interactions with photons. For example, the loss of a hydrogen atom from a fjord position, resulting from the absorption of a photon, would likely lead to the formation of a pentagon, as described in the mechanisms presented in this Section, driven by the minimisation of the resultant carbon radical site. This structure would then remain in such form until a subsequent interaction with a photon. It is possible, however, that the absorption of a photon by a PAH molecule may result in the loss of a hydrogen atom, or the breaking of a C-C bond, which would then, rather than go on to transform the structure to a new stable form, recombine within the time between photon absorptions. This would reduce the likelihood of the molecule undergoing any major transformations that could result in the forming of a fullerene molecule. For this reason, direct comparison to processes in the ISM is made very difficult, and while the experiments described provide insight into mechanistic details, improvements to experiments are needed to bridge the gap between laboratory and astrophysical conditions.

3.4.2.1 Fjord and bay hydrogens

Notably, the mechanisms outlined in Section 3.4.2 and shown in Figure 3.18 and Figure 3.19 do not require an initial ejection of a C atom to form a pentagonal ring, as is the case for the initiation of the fullerene formation process in zig-zag-edged graphene.[23] Instead, it is the bay- (armchair) and fjord-type positions that are of importance. On the loss of bay hydrogens from the edge of a PAH molecule, rearrangement can be initiated that leads to the formation of a five-membered ring at that position (as seen in Figure 3.18 and Figure 3.19). For a molecule containing fjord hydrogens, the loss of these atoms leads to the formation of a new C-C bond to result in a new five-membered ring – a process that would require even less energy than the one described for bay hydrogens, in which a Stone-Wales rearrangement is needed. As such, fjord hydrogens may be an important structural feature of the astrophysical PAH population when considering the formation of curved structures such as fullerenes. To date, there has been little focus on PAHs containing fjord regions in the context of astrophysical chemistry. The NASA Ames PAH IR Spectroscopic Database (www.astrochem.org/pahdb),[40] which contains the theoretical vibrational spectra of approximately 700 different PAHs, holds very few results for fjord-containing PAHs. Mackie *et al.*[37] note the behaviour of PAHs containing fjord regions when fully dehydrogenated, *i.e.* the joining of the fjord to form a pentagonal ring, and there is only one published gas-phase IR spectrum of a fjord-containing PAH – benzo[c]phenanthrene.[41] The structure of benzo[c]phenanthrene is shown in Figure 3.21, alongside two other molecules: tetracene and benz[a]anthracene. All three of the molecules depicted have the same chemical formula – $C_{18}H_{12}$ – but contain different structural features; while tetracene contains neither bay nor fjord regions, benz[a]anthracene can be seen to have a bay region, and benzo[c]phenanthrene contains a fjord region.

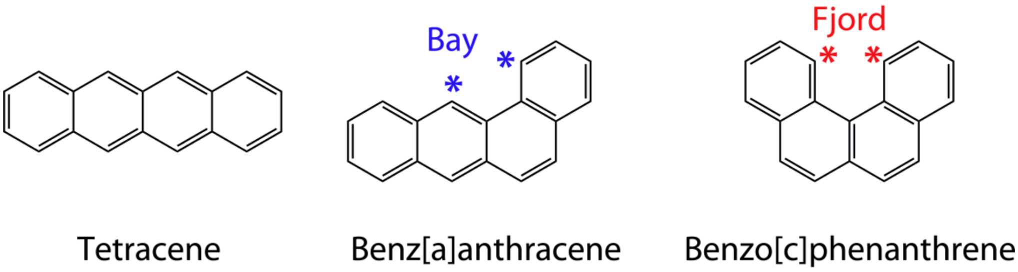

Figure 3.21. The structures of three PAH molecules: Tetracene, which contains neither bay nor fjord regions; benz[a]anthracene, containing a bay region; and benzo[c]phenanthrene, which contains a fjord region.

Considering the potential importance and energy efficiency of PAHs with fjord regions in the formation of fullerenes, DFT calculations were carried out to calculate the vibrational spectra of the three molecules shown in Figure 3.21. This was for the purpose of identifying the effect of bay- and fjord-type structures on the spectra of 'normal' PAHs, *i.e.* those that contain neither bay nor fjord regions, and to confirm that fjord-containing PAHs exhibit no spectral features that would discount their existence in space.

Vibrational frequencies and intensities of the three molecules were calculated using the B3LYP functional and the 6-31G* basis set, and a scaling factor of 0.98 was applied to the results – as is common practice when comparing DFT with laboratory results. The calculated spectra are presented in Figure 3.22, and the main result that can be seen is that the spectrum of benzo[c]phenanthrene does not contain any large peaks that are not found in the astronomical AIBs. As such, the spectrum of benzo[c]phenanthrene could feasibly be incorporated with those of other PAH molecules to form a typical AIB spectrum, meaning that PAH molecules containing fjord region could well exist in interstellar environments.

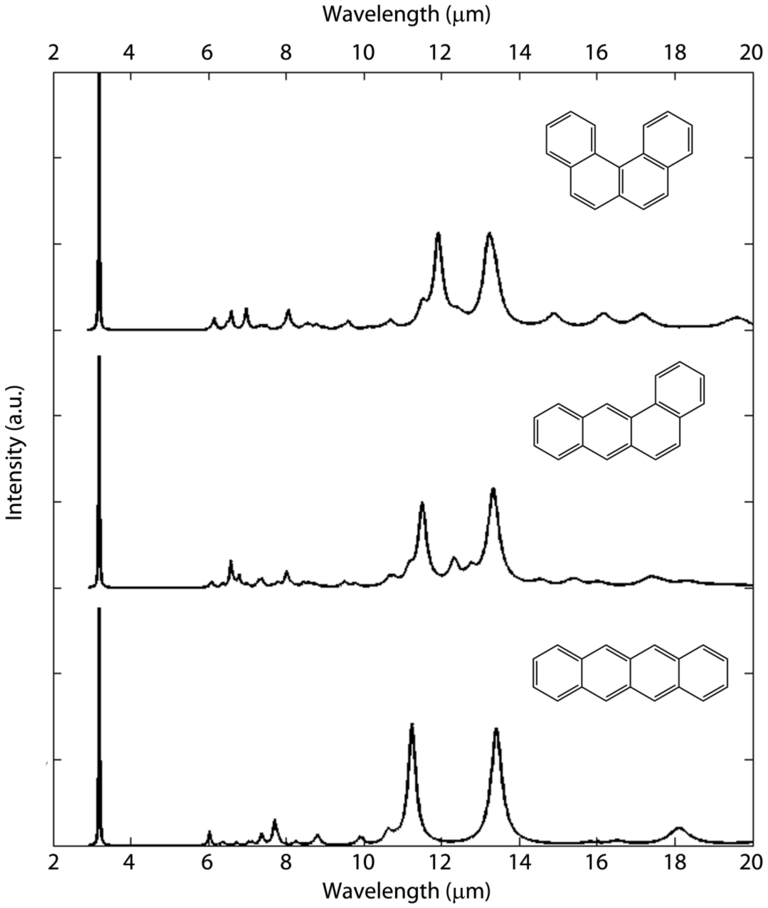

Figure 3.22. DFT calculated vibrational spectra of tetracene (lower spectrum), benz[a]anthracene (middle spectrum) and benzo[c]phenanthrene (upper spectrum). The calculated vibrational frequencies have been scaled using a scaling factor of 0.98.

The largest change in the spectra between the three molecules occurs in the 10 – 15 μm region, wherein lie the peaks assigned to the C-H out-of-plane (OOP) bend modes of the PAH molecules. The positions of peaks in this region are dependent on the number of adjacent hydrogen atoms on the same six-membered ring,[42] and the shifts in this region of the spectra in Figure 3.22 can be explained accordingly. In the spectrum of tetracene, two peaks can be seen between 10 and 15 μm, at 11.24 μm and 13.41 μm, which correspond to the OOP bend of 'solo' C-H bonds (*i.e.* C-H bonds with no adjacent C-H bonds on the same ring), and 'quartet' C-H bonds, respectively. Each of the three molecules contains eight quartet hydrogens, and so the quartet OOP bend peak varies very little between each spectrum. The main shift is seen in the second major peak within the 10 – 15 μm range; benz[a]anthracene, which contains two solo hydrogens and two duo hydrogens, has a peak which falls at 11.50 μm and benzo[c]phenanthrene, containing four duo hydrogens, has a peak that falls at 11.91 μm. In terms of corresponding astronomical emission bands, the 11.50 μm peak of benz[a]anthracene could contribute to the red tail of the 11.2 μm emission band (discussed in Chapter 2 of this Thesis). The 11.91 μm peak of benzo[c]phenanthrene could be responsible for an astronomical emission band at ~ 12 μm, seen in the spectra of some objects (examples include NGC 7027 and HD 44179, presented in Figure 9 of Candian and Sarre).[43]

The shifts and differences of the three calculated spectra demonstrate the diversity of the possible spectra of different PAH molecules, and show that fjord regions, that have not received much attention within the context of astronomical PAH populations, can be incorporated without causing significant changes to the spectrum so as to discount their existence.

Interestingly, it is known from studies of graphene that zig-zag edges that are not hydrogen-terminated will reconstruct to form armchair-type edges that contain alternate 7- and 5-membered rings.[44, 45] This is so that the free radicals terminating the graphene are placed in a way such that two adjacent radicals can overlap, which they are unable to do in a zig-zag edge, and form a pseudo C≡C bond, stabilising the graphene edge. This is significant in the context of top-down fullerene formation mechanisms that have been proposed previously in which the first step is the complete dehydrogenation of a PAH.[21, 25] Due to the low energy barrier of the edge reconstruction, this is a process that the dehydrogenated PAHs may easily undergo, thereby introducing pentagons into the structure and potentially removing the necessity for C atom loss to initiate transformation into a fullerene.

3.5 Combined TEM and MALDI-TOF MS methodology

An experimental methodology was designed and implemented to initiate and characterise PAH transformations sequentially in order to confirm resultant products using both microscopy and spectrometry. A schematic detailing the steps involved is shown in Figure 3.23. This illustrates a 'probe – stimulus – probe' experimental arrangement in which low dose TEM (~ 10^6 e^- nm^{-2} s^{-1}) is used to view and characterise a PAH sample without causing any damage, and MALDI-TOF MS at high laser fluence is then used to initiate transformations and detect products formed. Low dose TEM is used as a final step to image the irradiated area and to view the products using direct space imaging.

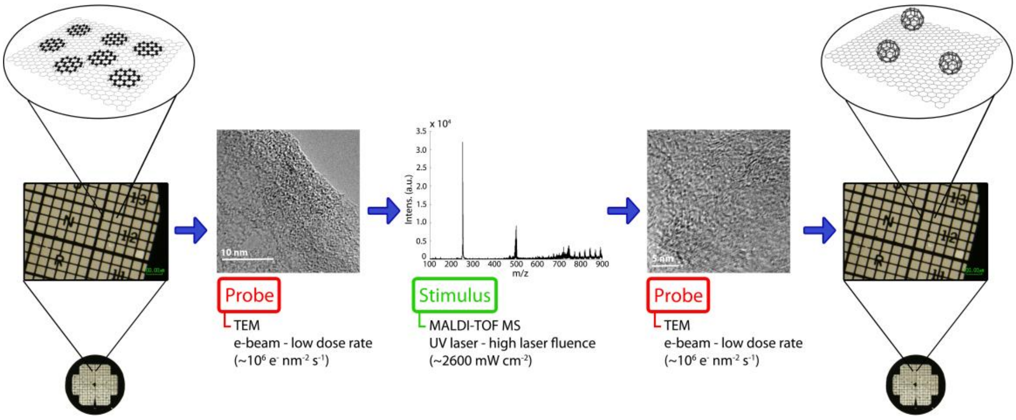

Figure 3.23. Schematic illustration of the 'probe-stimulus-probe' format of experiments carried out in this Section, in which an area of coronene, deposited on a carbon-coated TEM grid, is characterised using low-dose TEM, and then irradiated using the UV laser of MALDI-TOF MS to initiate transformations within the sample. Finally, the irradiated area is characterised again, using the locators on a TEM finder grid, to view the results of the induced transformations and to determine the nature of any products formed.

It is worth noting that this experimental sequence can in theory be reversed, so that low laser fluence MALDI-TOF MS is used as the 'probe', to characterise the sample before and after irradiation, and high dose TEM is used to initiate transformations within the sample. Experiments of this type are not detailed here, however, due to difficulties in matching the size of the irradiated area in TEM and MALDI-TOF MS; the irradiated area in MALDI-TOF MS (~ 0.02 cm^2) is much bigger than that in TEM (~ 1500 nm^2), so using MALDI-TOF MS as the 'probe' would not give an accurate representation of the products formed in the TEM irradiated area; it would in fact include a large part of the surrounding area of sample that had not been irradiated.

An initial control experiment was carried out in which graphite flakes were deposited onto a MALDI target plate and irradiated using the UV laser at the same laser fluence (~ 2600 mW cm^{-2}) as was used in the main experiment. This was to eliminate the possibility that C_{60}, or indeed any peaks falling where PAH oligomers are expected, might be formed from graphite flakes in these conditions. The resultant mass spectrum is given in Figure 3.24, and it is seen that there is no C_{60} detected.

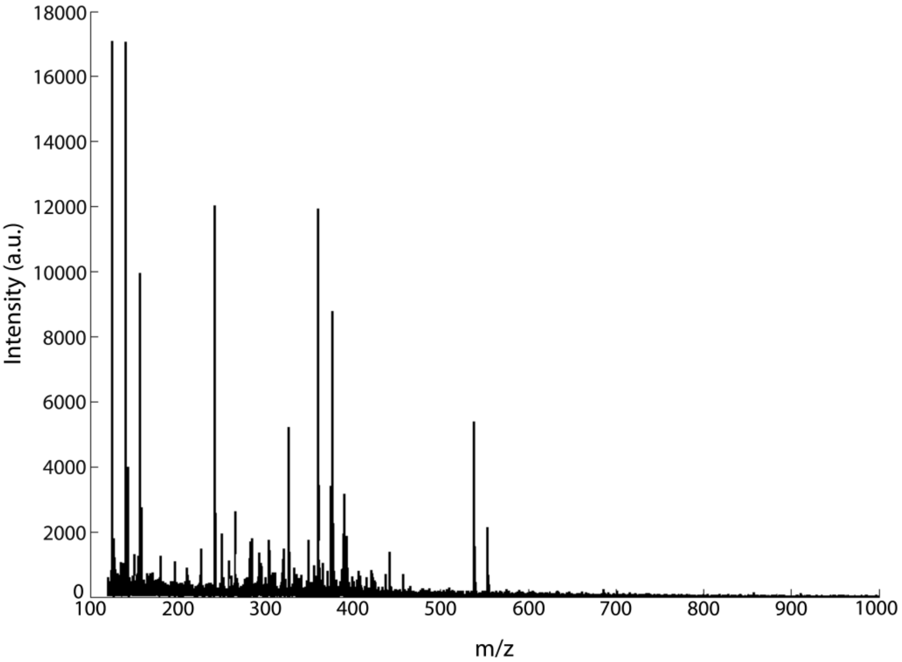

Figure 3.24. Mass spectrum from the MALDI-TOF MS of graphite flakes. No C_{60} is detected in this experiment and peaks fall at *m/z* values different to those of significant PAH oligomers.

Additionally, no peaks are seen in the spectrum shown in Figure 3.24 that fall at *m/z* values of the PAH oligomers that have been discussed in Section 3.4. As such, PAH oligomers and fullerenes detected in the combined TEM and MALDI-TOF MS experiment can be attributed with confidence to structures formed from the PAH molecules themselves.

A sample of coronene was supported on graphite flakes, deposited onto a TEM finder grid and imaged by TEM using a low dose (~ 10^6 e^- nm^{-2} s^{-1}) of electrons and minimal exposure time to avoid transformations caused by the e-beam. The PAH sample was then irradiated, in the same area on the grid, using MALDI-TOF MS at high laser fluence (~ 2600 mW cm^{-2}) and the resultant mass spectrum revealed the detection of coronene oligomers and C_{60}, in agreement with the results presented in Section 3.4.1. Finally, the irradiated area of the sample was reanalysed using TEM to assess the effect of the UV laser irradiation. This final characterisation, carried out within the UV irradiated area, revealed the formation of a number of fullerene structures not previously observed prior to irradiation. Figure 3.25 shows the results of this experiment, and includes the TEM micrographs obtained before and after the high laser fluence irradiation of the coronene sample, along with the mass spectrum acquired as a result of the MALDI-TOF MS experiment. In addition to the visible fullerene-type structures that can be seen in the micrograph, the sample showed far greater stability under the e-beam following UV irradiation; structures appeared to be almost static and less susceptible to e-beam induced transformations. This indicates that these structures are in fact fullerene cages, and not PAH molecules of the same diameter, for if this was the case then the sequence of peripheral hydrogen loss leading to formation of higher mass oligomers, as detailed in Section 3.3.1, would be observed.

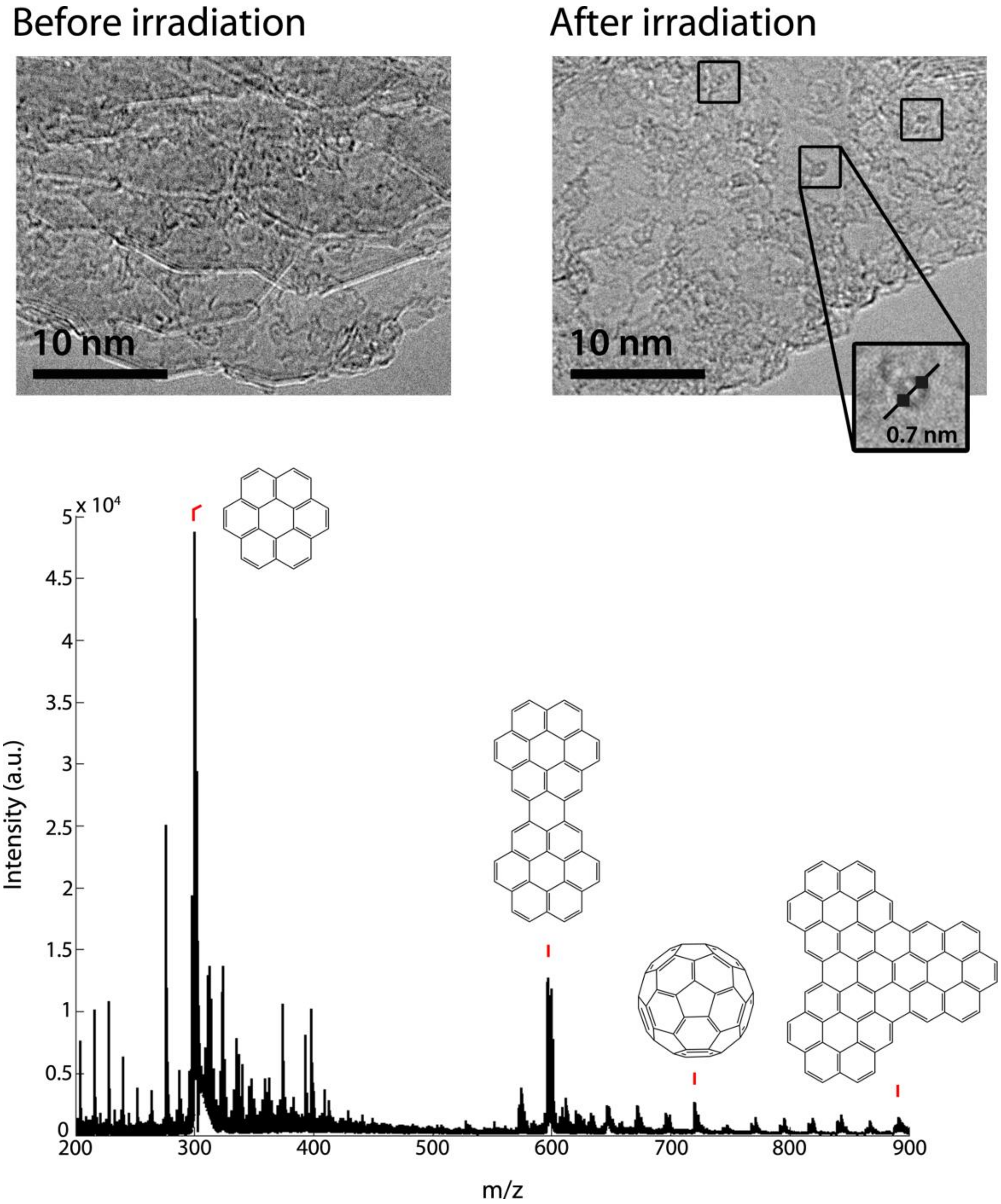

Figure 3.25. TEM micrographs (top) of a sample of coronene before and after irradiation using MALDI-TOF MS. Boxes highlight fullerene structures seen following irradiation along with a magnified example illustrating the diameter of the structure (0.7 ± 0.1 nm). The mass spectrum resulting from the UV irradiation of the sample (bottom) shows the oligomer structures assigned to major peaks, along with the detection of the fullerene C_{60}.

3.6 Mixtures of PAHs

In astrophysical environments, the population of PAHs would include many different PAH molecules – not just a single type of structure. For this reason, TEM and MALDI-TOF MS irradiation experiments were carried out on mixtures of PAHs in order to determine whether there are any significant changes in the behaviour of the molecules, or in the products formed.

3.6.1 TEM of a mixture of PAH molecules

A 1:1 mixture of pyrene and coronene was dispersed and deposited onto a TEM grid, following the same procedure that was used for individual PAH experiments. As for the experiments outlined in Section 3.3, PAHs were supported on graphite flakes, the experiment was run for approximately 30 mins, and images were taken periodically to view the changes to the sample over time. Once again, the TEM experiment was carried out at an accelerating voltage of 100 kV, at which the ejection of the hydrogen atoms from the PAH molecules will occur. As such, it was expected that a similar behaviour would be observed as in the experiments carried out on each individual PAH sample, *i.e.* the growth of PAH aggregates and oligomers.

The time-series of images acquired from this experiment is given in Figure 3.26, in which it can be seen that a very similar behaviour to that of a sample of a single type of PAH is indeed observed. The first image of the time series in Figure 3.26 shows the sample containing no well-defined structures which, as time goes on, becomes clearer and contains many defined, discrete species. This suggests that the aggregation of PAHs and the formation of larger oligomers is not exclusive to a sample containing one type of PAH.

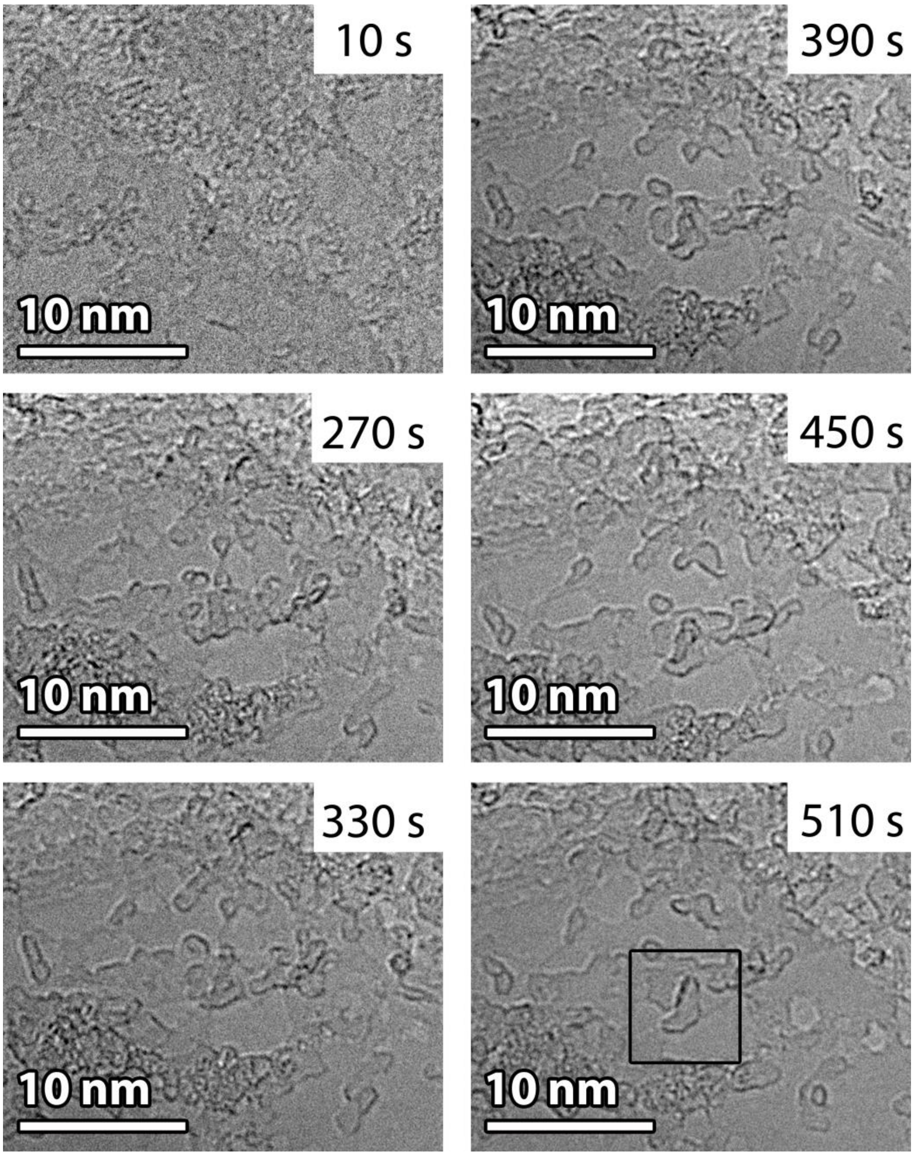

Figure 3.26. TEM micrographs showing the evolution of PAH oligomers during the irradiation of a mixture of pyrene and coronene with a 100 keV e-beam. The black box in the final image of the time series indicates the shape that is shown in Figure 3.27.

In the final image of Figure 3.26 (at 510 s), an example of a PAH oligomer is highlighted in the black box. This shape is presented at a higher magnification in Figure 3.27, and is labelled with some of its measurements. From the measurements taken of this particular shape in the TEM image, a structure containing coronene and pyrene units was constructed which closely matched its size, and which is shown also in Figure 3.27. While the structure given in Figure 3.27 may not be the exact molecule that is seen in the TEM micrograph, it provides an example to guide the eye and to understand how the PAH molecules can interact with each other following loss of their hydrogen atoms.

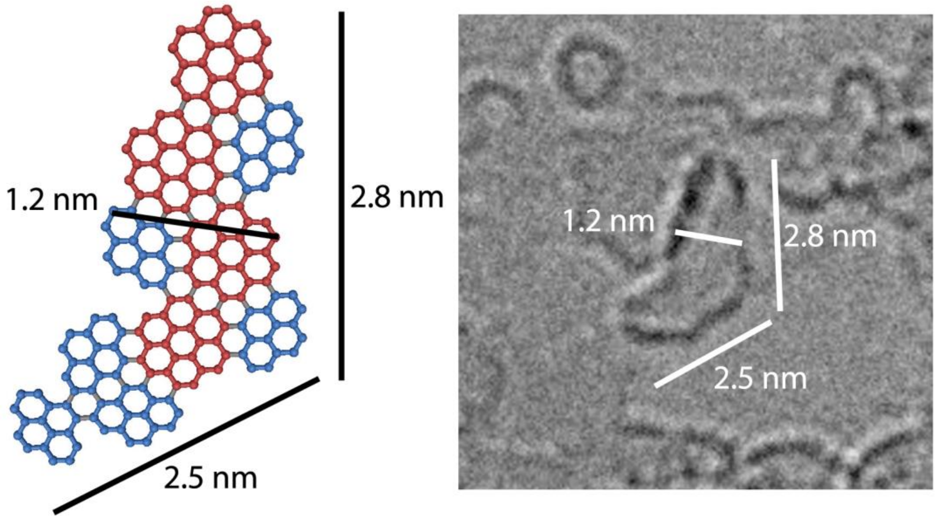

Figure 3.27. Example of a PAH oligomer or aggregate seen in the TEM irradiation of a mixture of coronene and pyrene. The TEM image used (right) is that which is outlined in the black box in Figure 3.26. The measurements of the oligomer are shown, and a corresponding structure is given with the same measurements (left), which is made up of coronene units (red) and pyrene units (blue).

3.6.2 MALDI-TOF MS of a mixture of PAH molecules

A thin layer of a mixture of coronene and perylene was deposited onto the MALDI-TOF MS target plate, and a UV irradiation experiment was carried out as detailed in Section 3.4.1. The mass spectrum resulting from the UV irradiation of this mixture, at a laser fluence of ~ 2600 mW cm^{-2}, is shown in Figure 3.28. Included in the figure are structures assigned to the major peaks. The mass spectrum shown in Figure 3.28 seems, for the most part, to be a superposition of the mass spectra of the individual PAHs, reported in Section 3.4.1; there are seen the molecular ion peaks of both perylene (m/z = 252) and coronene (m/z = 300), along with each of their ‘dimer’ molecules (perylene dimer m/z = 500, coronene dimer m/z = 596). One additional peak is seen in the mass spectrum that falls at m/z = 548, which can be assigned to a molecule with one coronene and one perylene unit, each having lost two hydrogen atoms. Two possible structures for this mixed-dimer molecule are shown in the grey box in Figure 3.28, one of which contains two fjord regions. It cannot be determined which of these mixed-dimer structures is the one being detected – or if it is in fact both – but there are additional peaks that fall at *m/z* = 546 and 544, which may well arise from the loss of two and four fjord hydrogen atoms, respectively. In addition, it can be seen in Figure 3.28 that C_{60} is detected, indicating that its formation under these conditions is not exclusive to samples containing only one type of PAH as a precursor; this is of significance in an astrophysical context as the ISM clearly contains a wide variety of PAHs.

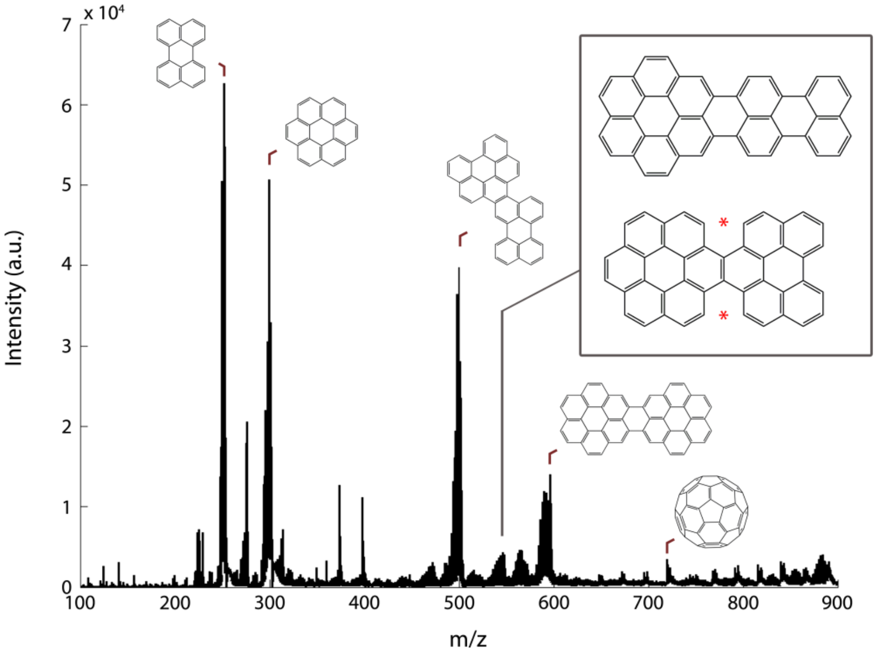

Figure 3.28. Mass spectrum resulting from UV irradiation of a mixture of coronene and perylene, at a laser fluence of ~ 2600 mW cm^{-2}. Proposed structures of the species formed are given above the corresponding mass peaks, including new possible hybrid structures in the grey box. Red asterisks indicate fjord positions.

It was seen in Section 3.4.1 that both coronene and perylene individually exhibit fullerene formation under UV irradiation, and, as shown in Figure 3.28, the same is seen when a mixture of the two is used. The same MALDI-TOF MS irradiation experiment was carried out on a mixture of coronene and pyrene, the latter being a PAH molecule that does not form C_{60} on its own, and the resultant mass spectrum is given in Figure 3.29.

It can be seen in Figure 3.29 that similar results to the coronene/perylene mixture are obtained. Peaks are seen that correspond to pyrene (*m/z* = 202), coronene (*m/z* = 300), and the ‘dimers’ of each (pyrene dimer *m/z* = 400, coronene dimer *m/z* = 596). Additionally, there is a peak at *m/z* = 498 that corresponds to a mixed-dimer structure, and C_{60} is detected at *m/z* = 720.

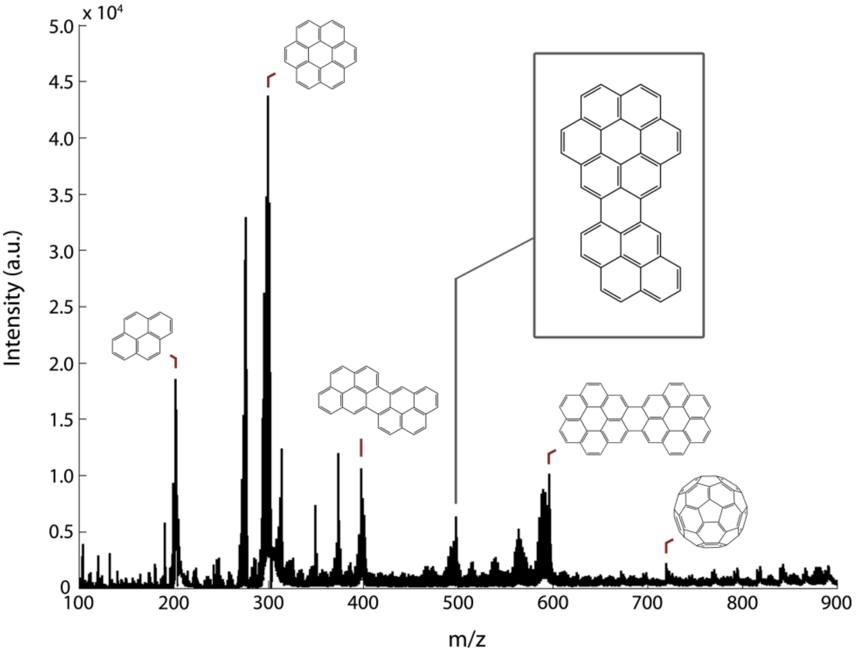

Figure 3.29. Mass spectrum resulting from UV irradiation of a mixture of coronene and pyrene, at a laser fluence of ~ 2600 mW cm^{-2}. Proposed structures of the species formed are given above the corresponding mass peaks, including a new possible hybrid structure in the grey box.

The results of the TEM and MALDI-TOF MS experiments carried out on mixtures of PAHs confirm that in a population of PAHs containing many structures, the behaviour of these molecules is likely to be very similar to that seen for individual samples of different molecules. Upon dehydrogenation, or loss of individual hydrogen atoms, these molecules will react with others close by to form new C-C bonds and in doing so will build up to form larger PAH structures. The results of UV irradiation of mixtures of PAHs using MALDI-TOF MS particularly demonstrate that while, individually, certain PAH molecules do not undergo transformations that result in the formation of C_{60}, the inclusion of these PAHs in mixtures does not negatively impact on fullerene formation. This is a positive result in the context of astrophysical fullerene formation, as it is a slightly closer representation of astrophysical PAH populations, which would contain more than one type of PAH.

3.7 A comparison of e-beam and UV irradiation

A large proportion of this Chapter utilises TEM and MALDI-TOF MS as sources of energy, which are relied upon and seen to induce transformations within PAH samples; a comparison is made here of the significant numbers that are involved and the energetics of the processes that were found to occur.

C-H bond dissociation is considered to be a critical step in the transformations of PAHs, in both the photo-activated processes (MALDI-TOF MS measurements and in astrophysical environments) and e-beam induced processes (TEM imaging). The dissociation of this bond leads to reactive intermediates – aryl radicals – responsible for the oligomerisation of PAHs and the formation of fullerenes. It is important to appreciate the differences and similarities of the conditions that the molecules experience in MALDI-TOF MS and in TEM, and attempt to rationalise why they lead to similar chemical transformations. A key difference is that under the e-beam of TEM, C-H bond dissociation is directly triggered by the kinetic energy transferred from a fast electron to a hydrogen atom, while under the light-activated conditions in MALDI-TOF MS the molecule absorbs the photon and C-H dissociation occurs as a result of the relaxation of the photo-excited state of a PAH.

The important steps required for the mechanisms proposed in Figure 3.18 and Figure 3.19, and that are therefore likely to be important in the transformations seen in TEM also, are the breaking of C-H bonds and C-C bonds, and the Stone-Wales rearrangement process. The bond enthalpies for C-H and C-C bonds are given in Table 3.3, along with the activation energy of the Stone-Wales rearrangement.

Although the kinetic energy of the electrons in the e-beam used in these experiments is 100 keV, not all of this energy is transferred to an atom in a collision. The maximum amount of transferrable energy (T_{max}) depends on the element of interest, and can be calculated using the following equation:

$$T_{max} = \frac{2 \cdot M \cdot E\ (E + 2m_e \cdot c^2)}{(M + m_e)^2 \cdot c^2 + 2M \cdot E}$$

where M is the atomic weight of the element, E is the energy of incident electrons, m_e is the mass of an electron, and c is the speed of light. Notably, T_{max} is inversely proportional to the atomic weight of the element, so that lighter elements, under the same TEM conditions, receive significantly more energy from the e-beam than do the heavier elements. T_{max} values for both carbon and hydrogen – the elements of significance in this study – are given in Table 3.3.

The dose rate in TEM can be altered manually, and the 'low-dose' and 'high-dose' values – used for imaging without causing transformations and used for initiating transformations, respectively – are given in Table 3.3. These are not absolute values, but give an approximate rate of electrons impacting per nm^2 per second. A corresponding 'dose rate' of photons per nm^2 per second was calculated, using the number of photons per pulse, the pulse energy and duration, and the area of irradiation. The value is shown in Table 3.3.

Table 3.3. Significant values for the studies described in this Chapter, including the energies of important chemical processes, energies supplied by the 100 keV electrons in TEM and single photons (355 nm) in MALDI-TOF MS, and the respective dose rates of TEM and MALDI-TOF MS.

	kJ mol^{-1}	eV
C-H bond enthalpy	400 – 500	4 – 5
C-C bond enthalpy	~ 720	~ 7.5
Stone-Wales activation energy[39]	~ 870	~ 9
T_{max} of e^- to carbon in TEM	1930	20
T_{max} of e^- to hydrogen in TEM	23060	239
$h\nu$ energy in MALDI-TOF MS	336.7	3.5
Low-dose TEM dose rate	10^6 e^- nm^{-2} s^{-1}	
High-dose TEM dose rate	10^9 e^- nm^{-2} s^{-1}	
High laser fluence 'dose rate'	43797 $h\nu$ nm^{-2} s^{-1}	

When considering the irradiation of molecules, the term cross-section (σ) is used to express the probability of a particular interaction occurring. In TEM, the interaction cross-section is the chance of an incident electron interacting in some way with an atom; of particular relevance to the study in this Chapter is the cross-section for H atom ejection, *i.e.* the probability that an H atom on the edge of a PAH will be knocked out by an electron. When irradiating with UV photons, the analogous term is the cross-section for photon absorption – the probability of a photon being absorbed by a molecule – which can be used, in conjunction with the quantum yield of decomposition of a given molecule, to obtain a value for the cross-section for decomposition upon photon absorption. For the transformations of interest in these studies, the term 'decomposition' is taken to represent C-H bond dissociation. The cross-sections for each technique can in turn be used to work out lifetimes of the molecules under each form of irradiation. This has been done, and the results are presented in Table 3.4. The steps taken to obtain the values given in Table 3.4 are outlined below.

For UV irradiation, the values of cross-section of photon absorption for each of the four PAH molecules discussed in this Chapter were obtained from the French-Italian database,[46] and were found to be 7.06, 27.8, 8.52 and 112.26 megabarn (Mb)[†] for anthracene, pyrene, perylene and coronene, respectively. These values were then used to obtain a cross-section of decomposition following photon absorption (σ_d) for each molecule by multiplying with the quantum yield of decomposition – a unitless value between 0 and 1 that describes the efficiency of decomposition of a molecule following the absorption of a photon. The quantum yield of decomposition of a molecule depends heavily on the environment of the molecule and as such it can be difficult to determine. For the purpose of this Section, the quantum yield of decomposition was assumed to be 1, *i.e.* the molecule decomposes upon absorption of the first photon, to act as an upper limit of the system.

$$\sigma_d = crosssection\ of\ photon\ absorption \\ \times quantum\ yield\ of\ decomposition\ (taken\ as\ 1)$$

It should be noted that the term 'decomposition' could apply to a number of processes that result in the breaking down of the molecule. For this study, the loss of an H atom, *i.e.* CH bond dissociation, is the first stage of the process that leads to the formation of oligomers and, in some cases, fullerenes. As these species are detected in MS, it is clear that to some degree this is the 'decomposition' that is occurring, and hence the values of lifetime under UV

[†] 1 barn = 10^{-28} m^2

irradiation are taken to be the time it takes for a PAH molecule to undergo a transformation, most likely *via* the route of H loss.

To compare the cross-section values for each molecule with each other, they must be normalised to take into account the area of the molecule (calculated using the DS ViewerPro software package). This was achieved by multiplying σ_d for each molecule by its area (in barn), to obtain a unitless normalised cross-section (σ):

$$\sigma = \sigma_d \times area\ of\ molecule$$

To calculate the lifetimes of each of the PAHs under the conditions used, the 'dose rate' value for the UV laser in MALDI-TOF MS (given in Table 3.3 above) was converted to hν barn^{-1} s^{-1}. The following equation was then used:

$$Lifetime\ (s) = \frac{1}{(\sigma_d(barn) \times dose\ rate\ (h\nu\ barn^{-1}s^{-1}))}$$

For e-beam irradiation, a similar process was carried out. The value of cross-section (σ_d), per atom, of H atom ejection from a coronene molecule was taken from Chamberlain *et al.*[29] to be 71.8 barn, and applied to all PAHs. This was then multiplied by the number of H atoms in each PAH, to obtain σ_d per molecule.

$$\sigma_d = \sigma_d(per\ atom) \times numberof\ H\ atoms$$

As before, a unitless normalised cross-section (σ) value for each molecule was obtained by multiplying σ_d by the area of the molecule, in barn. To calculate the lifetime of each PAH under the e-beam, the dose rate of the e-beam (Table 3.3) was converted to e$^-$ barn^{-1} s^{-1}, and the equation for lifetime shown previously was applied. The values obtained as a result of all of these calculations are presented in Table 3.4.

Table 3.4. Values of cross-section for decomposition (*i.e.* ejection of an H atom) and lifetimes of each PAH under the UV irradiation in MALDI-TOF MS and e-beam irradiation in TEM.

UV irradiation PAH molecule	Area of molecule Å^2	 barn	Cross-section (σ_d)* barn	Normalised cross-section (σ)	Dose rate hν barn^{-1} s^{-1}	Lifetime s
Anthracene	42.81	4.281×10^9	7.06×10^6	0.001649	4.3797×10^{-6}	0.03234
Pyrene	53.44	5.344×10^9	2.78×10^7	0.005202	4.3797×10^{-6}	0.00822
Perylene	58.62	5.862×10^9	8.52×10^6	0.001453	4.3797×10^{-6}	0.02681
Coronene	80.15	8.015×10^9	1.12×10^8	0.014006	4.3797×10^{-6}	0.00204

e-beam irradiation PAH molecule	Area of molecule Å^2	 barn	Cross-section (σ_d)† barn	Normalised cross-section (σ)	Dose rate e$^-$ barn^{-1} s^{-1}	Lifetime s
Anthracene	42.81	4.281×10^9	718.0	1.677×10^{-7}	0.1	0.01393
Pyrene	53.44	5.344×10^9	718.0	1.344×10^{-7}	0.1	0.01393
Perylene	58.62	5.862×10^9	861.6	1.470×10^{-7}	0.1	0.01161
Coronene	80.15	8.015×10^9	861.6	1.075×10^{-7}	0.1	0.01161

* σ_d = cross-section of decomposition following photon absorption

† σ_d = cross-section of H atom ejection

It is important to note that some of the values given in Table 3.4 are available only as estimates. As mentioned previously, the calculations involving UV irradiation begin by assuming the quantum yield for decomposition to be 1. This provides an upper limit for the damage caused when a photon is absorbed, and hence the resultant lifetimes will be a lower limit, *i.e.* the shortest amount of time a PAH will survive under UV irradiation for before decomposition.

Similarly, the σ_d value for the ejection of an H atom from a PAH in e-beam irradiation that was used in these calculations was originally calculated for coronene molecules standing 'edge-on' (*i.e.* parallel) to the e-beam.[29] In the experiments described in this Chapter, the PAH molecules are deposited on graphite flakes and are expected to be lying flat on the surface, *i.e.* perpendicular to the e-beam. The cross-section of H atom ejection in TEM has some dependence on the threshold energy – that is, the energy that the e-beam needs to transfer for atom ejection to occur. The threshold energy for molecules perpendicular to the e-beam will be slightly higher than for those positioned parallel to the beam, and hence the value of the cross-section (σ_d) is likely to be lower than that used in these calculations. In addition, the threshold energy will be marginally different for each PAH molecule, resulting in different cross-section values. However, differences in the threshold energies, and cross-sections, are larger between different elements than between the same element in different environments, *i.e.* on the edges of different PAHs. Finally, the calculated σ_d value that was used in this Section does not take into account inelastic interactions of electrons with the sample, and the cross-section therefore acts as a lower limit, indicating that the calculated lifetimes are an upper limit – the longest amount of time a molecule will survive under the e-beam before decomposition *via* C-H bond dissociation. Despite the approximate nature of this comparative analysis and the significant uncertainty of some experimental parameters, the expected timescales of photon and e-beam activated transformations in PAHs under our experimental conditions are remarkably similar (e.g. the lifetimes of PAHs molecules are within an order of magnitude, Table 3.4). This supports the methodological validity of the combined TEM and MALDI-TOF MS experimental approach developed for studying transformations of PAHs in this Chapter.

3.8 Conclusions

The investigation detailed in this Chapter has demonstrated that under harsh laboratory conditions (UV laser or e-beam irradiation), modest-sized PAHs can lose hydrogen atoms and form reactive radical species which combine to form larger aromatic molecules (e.g. PAH oligomers) with ≥ 60 C atoms. These oligomeric PAHs undergo transformations leading to closed carbon cages – fullerenes – which are thermodynamically the most stable form of carbon at the nanoscale. Fullerenes are seen to form from PAHs under both UV and e-beam irradiation, as demonstrated by mass spectrometric measurements and direct-space imaging respectively.

The formation of C_{60} following the initial irradiation of modest-sized PAHs is significant in relation to the question of C_{60} formation in astrophysical environments; this work shows a clear transformation from PAH precursors of known initial structure with no excess carbon as in some laboratory experiments, for example in the form of graphite or graphene sheets.

Irradiation of PAHs using the e-beam of TEM yields oligomeric species following the loss of all peripheral hydrogen atoms. In some cases, fullerene cage structures are also seen to form under the e-beam. The formation of PAH oligomers is a result shared with the irradiation of PAHs using the UV laser of MALDI-TOF MS, which also shows the positive detection of formed fullerene molecules. The MALDI-TOF MS experiments appear to involve the loss of individual or pairs of hydrogen atoms, and *m/z* values of the detected species allow determination of potential structures of the oligomers that are formed. It has been shown that coronene and perylene can undergo major transformations leading to the formation of C_{60} fullerenes while pyrene and anthracene under the same conditions form large oligomers but no fullerenes.

Cross correlation of the data obtained from both of the experimental methods used, involving detailed study of the molecular species in MS and determination of the molecular size/shape in real-space TEM images of the key intermediates in fullerene formation, sheds light on possible mechanisms of PAH conversion to C_{60} in the ISM. Mechanistic steps are revealed that involve the initial irradiation-induced loss of hydrogen atoms which lead, *via* carbon radical-containing species which react with neighbouring molecules, to the formation of large planar oligomers. A subsequent ‘top down’ step involves hydrogen-loss, C-C bond formation, and Stone-Wales rearrangements within the planar oligomers. Pentagons that are formed within the structure as a result of these steps introduce curvature into the molecules, which ultimately leads to the ‘zipping’ of the structure to form fullerene cages. Key aspects of the mechanisms discussed are the role of bay- and fjord-type hydrogens, the latter of which have so far been discussed very little in an astrophysical context. DFT calculations carried out on PAHs containing bay and fjord hydrogens showed that these structural features may be feasibly incorporated into astrophysical PAH populations without significantly altering the AIB emission spectrum.

An innovative experimental strategy was developed which enabled the use of MALDI-TOF MS and TEM as triggers of PAH transformations at high fluence or dose rates of UV laser or e-beam, or as analytical tools - monitoring molecular weights in MS or molecular size in TEM imagery, respectively. An example given in this Chapter follows the route of 1) low dose TEM, 2) high laser fluence MALDI-TOF MS, 3) low dose TEM, to provide evidence, using both experimental techniques, for the formation of fullerenes resulting from the irradiation of coronene. This new methodology has proved successful in this format and may be useful for other applications in similar experiments.

Irradiation experiments using TEM and MALDI-TOF MS were repeated on samples containing mixtures of two PAHs, to move a step closer to representing astrophysical PAH populations. The e-beam irradiation of a mixture of coronene and perylene demonstrated behaviour very similar to that of a sample of an individual PAH, in which shapes were seen to increase in size over time and discrete species were formed that were made up of a number of PAH molecules. UV irradiation of two mixtures of PAHs –

coronene/perylene and coronene/pyrene – showed the detection by mass spectrometry of 'dimer' molecules made up of one of each of different PAHs used in the mixture. Mass spectrometry also displayed the detection of C_{60} for both mixtures, indicating its formation despite, in one case, the presence of pyrene – a PAH that did not form C_{60} when used in experiments on its own. The results of these experiments indicate that the behaviour of PAHs under e-beam and UV irradiation seems to be consistent and invariant, even when more than one type of PAH molecule is present.

The use of TEM and MALDI-TOF MS in similar ways, as sources of energy to induce transformations within molecules, prompted the calculation of a number of parameters that are significant when thinking about the energetics of the processes occurring. Values for cross-sections, *i.e.* the chance of decomposition of a PAH upon absorption of a photon or interaction with an electron, were calculated for both TEM and MALDI-TOF MS. These were used in conjunction with the dose rate of electrons and photons in each technique to deduce a lifetime for each molecule under each type of irradiation. While the numbers produced are not exact, they provide an approximate but useful comparison of the two techniques. In the particular case of MALDI-TOF MS, the values obtained allow for the process of decomposition and H atom loss to be expressed in a way similar to that used for TEM, which is not commonly used for UV irradiation.

The fullerene C_{60} has been detected in a number of different astronomical environments, and it is expected that its formation depends strongly on the conditions in each of those environments. In addition, it is certainly the case that the interstellar PAH population will be made up of a range of different PAH molecules, and therefore PAH oligomers would be made up of more than one type of smaller PAH. The results of this work provide significant support for the hypothesis that PAH molecules are precursors to fullerene formation, and the mechanistic steps that have been elucidated may be applied to other PAHs or PAH oligomers to form fullerenes. Consequently, the results reported here provide insight into a detailed potential route to fullerene formation in space.

3.9 References

1. H. W. Kroto, J. R. Heath, S. C. O'Brien, R. F. Curl and R. E. Smalley, *Nature*, 1985, **318**, 162-163.

2. M. W. Werner, K. I. Uchida, K. Sellgren, M. Marengo, K. D. Gordon, P. W. Morris, J. R. Houck and J. A. Stansberry, *ApJS*, 2004, **154**, 309-314.

3. K. Sellgren, K. I. Uchida and M. W. Werner, *ApJ*, 2007, **659**, 1338-1351.

4. J. Cami, J. Bernard-Salas, E. Peeters and S. E. Malek, *Science*, 2010, **329**, 1180-1182.

5. K. Sellgren, M. W. Werner, J. G. Ingalls, J. D. T. Smith, T. M. Carleton and C. Joblin, *ApJ Lett.*, 2010, **722**, L54-L57.

6. K. Sellgren, M. W. Werner, J. G. Ingalls, J. D. T. Smith, T. M. Carleton and C. Joblin, in *PAHs and the Universe: A Symposium to Celebrate the 25th Anniversary of the PAH Hypothesis*, eds. C. Joblin and A. G. G. M. Tielens, E D P SCIENCES, 2011, vol. 46, pp. 209-214.

7. K. R. G. Roberts, K. T. Smith and P. J. Sarre, *MNRAS*, 2012, **421**, 3277-3285.

8. D. A. García-Hernández, A. Manchado, P. García-Lario, L. Stanghellini, E. Villaver, R. A. Shaw, R. Szczerba and J. V. Perea-Calderón, *ApJ Lett*, 2010, **724**, L39-L43.

9. D. A. García-Hernández, S. Iglesias-Groth, J. A. Acosta-Pulido, A. Manchado, P. García-Lario, L. Stanghellini, E. Villaver, R. A. Shaw and F. Cataldo, *ApJ Lett*, 2011, **737**, L30.

10. D. A. García-Hernández , N. K. Rao and D. L. Lambert, *ApJ*, 2011, **729**, 126.

11. Y. Zhang and S. Kwok, *ApJ*, 2011, **730**, 126.

12. R. H. Rubin, J. P. Simpson, C. R. O'Dell, I. A. McNabb, S. W. J. Colgan, S. Y. Zhuge, G. J. Ferland and S. A. Hidalgo, *MNRAS*, 2011, **410**, 1320-1348.

13. C. Gielen, J. Bouwman, H. Van Winckel, T. L. Evans, P. M. Woods, F. Kemper, M. Marengo, M. Meixner, G. C. Sloan and A. G. G. M. Tielens, *Astron. Astroph.*, 2011, **533**, A99.

14. C. Gielen, J. Cami, J. Bouwman, E. Peeters and M. Min, *Astron. Astroph.*, 2011, **536**, A54.

15. R. E. Smalley, *Acc. Chem. Res.*, 1992, **25**, 98-105.

16. N. S. Goroff, *Acc. Chem. Res.*, 1996, **29**, 77-83.

17. S. Irle, G. S. Zheng, Z. Wang and K. Morokuma, *J. Phys. Chem. B*, 2006, **110**, 14531-14545.

18. W. Krätschmer, L. D. Lamb, K. Fostiropoulos and D. R. Huffman, *Nature*, 1990, **347**, 354-358.

19. J. B. Howard, J. T. McKinnon, Y. Makarovsky, A. L. Lafleur and M. E. Johnson, *Nature*, 1991, **352**, 139-141.

20. L. T. Scott, M. M. Boorum, B. J. McMahon, S. Hagen, J. Mack, J. Blank, H. Wegner and A. de Meijere, *Science*, 2002, **295**, 1500-1503.

21. O. Berné and A. G. G. M. Tielens, *PNAS*, 2012, **109**, 401-406.

22. E. R. Micelotta, A. P. Jones, J. Cami, E. Peeters, J. Bernard-Salas and G. Fanchini, *ApJ*, 2012, **761**, 35.

23. A. Chuvilin, U. Kaiser, E. Bichoutskaia, N. A. Besley and A. N. Khlobystov, *Nat. Chem.*, 2010, **2**, 450-453.

24. A. G. G. M. Tielens, *Rev. Mod. Phys.*, 2013, **85**, 1021-1081.

25. O. Berné, J. Montillaud and C. Joblin, *Astron. Astroph.*, 2015, **577**, A133-A141.

26. H. Á. Galué, *Chem. Sci.*, 2014, **5**, 2667-2676.

27. J. Zhen, P. Castellanos, D. M. Paardekooper, H. Linnartz and A. G. G. M. Tielens, *ApJ Lett.*, 2014, **797**, L30 - L34.

28. J. Kong, C. A. White, A. I. Krylov, D. Sherrill, R. D. Adamson, T. R. Furlani, M. S. Lee, A. M. Lee, S. R. Gwaltney, T. R. Adams, C. Ochsenfeld, A. T. B. Gilbert, G. S. Kedziora, V. A. Rassolov, D. R. Maurice, N. Nair, Y. H. Shao, N. A. Besley, P. E. Maslen, J. P. Dombroski, H. Daschel, W. M. Zhang, P. P. Korambath, J. Baker, E. F. C. Byrd, T. Van Voorhis, M. Oumi, S. Hirata, C. P. Hsu, N. Ishikawa, J. Florian, A. Warshel, B. G. Johnson, P. M. W. Gill, M. Head-Gordon and J. A. Pople, *J. Comput. Chem.*, 2000, **21**, 1532-1548.

29. T. W. Chamberlain, J. Biskupek, S. T. Skowron, P. A. Bayliss, E. Bichoutskaia, U. Kaiser and A. N. Khlobystov, *Small*, 2015, **11**, 622-629.

30. A. Santana, A. Zobelli, J. Kotakoski, A. Chuvilin and E. Bichoutskaia, *Phys. Rev. B*, 2013, **87**, 094110.

31. A. V. Talyzin, I. V. Anoshkin, A. V. Krasheninnikov, R. M. Nieminen, A. G. Nasibulin, H. Jiang and E. I. Kauppinen, *Nano Lett.*, 2011, **11**, 4352-4356.

32. M. Fujihara, Y. Miyata, R. Kitaura, Y. Nishimura, C. Camacho, S. Irle, Y. Iizumi, T. Okazaki and H. Shinohara, *J. Phys. Chem. C*, 2012, **116**, 15141-15145.

33. B. Botka, M. E. Fustos, H. M. Tohati, K. Nemeth, G. Klupp, Z. Szekrenyes, D. Kocsis, M. Utczas, E. Szekely, T. Vaczi, G. Tarczay, R. Hackl, T. W. Chamberlain, A. N. Khlobystov and K. Kamaras, *Small*, 2014, **10**, 1369-1378.

34. C. Joblin, C. Masselon, P. Boissel, P. de Parseval, S. Martinovic and J.-F. Muller, *Rapid Commun. Mass Spectrum.*, 1997, **11**, 1619-1623.

35. L. Patiny and A. Borel, *J. Chem. Inf. Model.*, 2013, **53**, 1223-1228.

36. M. M. Boorum, Y. V. Vasil'ev, T. Drewello and L. T. Scott, *Science*, 2001, **294**, 828-831.

37. C. J. Mackie, E. Peeters, C. W. Bauschlicher and J. Cami, *ApJ*, 2015, **799**, 131 - 141.

38. A. J. Stone and D. J. Wales, *Chemical Physics Letters*, 1986, **128**, 501-503.

39. L. Li, S. Reich and J. Robertson, *Phys. Rev. B*, 2005, **72**, 184109.

40. C. W. Bauschlicher, Jr., C. Boersma, A. Ricca, A. L. Mattioda, J. Cami, E. Peeters, F. S. de Armas, G. P. Saborido, D. M. Hudgins and L. J. Allamandola, *ApJS*, 2010, **189**, 341-351.

41. J. Semmler, P. W. Yang and G. E. Crawford, *Vibrational Spectroscopy*, 1991, **2**, 189-203.

42. S. Hony, C. Van Kerckhoven, E. Peeters, A. G. G. M. Tielens, D. M. Hudgins and L. J. Allamandola, *Astron. Astrophys.*, 2001, **370**, 1030-1043.

43. A. Candian and P. J. Sarre, *MNRAS*, 2015, **448**, 2960-2970.

44. P. Koskinen, S. Malola and H. Häkkinen, *Phys. Rev. Lett.*, 2008, **101**.

45. P. Koskinen, S. Malola and H. Häkkinen, *Phys. Rev. B*, 2009, **80**, 073401.

46. G. Malloci, C. Joblin and G. Mulas, *Chem. Phys.*, 2007, **332**, 353-359.

4. Catalytic reactions of astrophysical interest

4.1 Background

Cosmic dust is mainly divided into two categories: 'bare' dust grains, and those with icy mantles. Of the bare grains, a majority are thought to be either carbonaceous in nature, *i.e.* graphitic or amorphous carbon, or silicate structures.[1] Silicate grains are characterised in astronomical spectra by two broad IR bands at about 10 and 18 μm, which were first observed and assigned in 1969,[2] and which can appear in absorption or emission.[3] These broad features are attributed to amorphous silicates, and it is the amorphous state in which most of cosmic silicates are found, particularly within the interstellar medium (ISM).[4] However, crystalline silicates, in particular in the forms of pyroxenes and olivines, have also been detected, for example in the circumstellar environments of oxygen-rich stars,[5, 6] and in the oxygen-rich disk surrounding the central binary star of the Red Rectangle nebula.[7]

The silicate grains that are the focus of most of this Chapter are olivines, which have the general formula ($(Mg_xFe_{1-x})_2SiO_4$), in which the relative amounts of Mg and Fe can vary and the two endmembers of the group are forsterite (Mg_2SiO_4) and fayalite (Fe_2SiO_4). These minerals belong to a class of silicates called neosilicates, and are among the structures most often discussed in an astrophysical context. Olivines, along with other cosmic dust analogues, have been investigated as surfaces on which reactions can occur. In particular, the formation of H_2, the most abundant molecule in the Universe, has been found to occur on the surfaces of olivines.[8-10] More recently, the catalytic role of olivines was extended to the formation of more complex molecules, in experiments that have demonstrated the formation of polycyclic aromatic hydrocarbons (PAHs) from acetylene over a heated olivine sample.[11]

Around carbon-rich stars, in circumstellar envelopes, amorphous and graphitic carbon grains are expected. In addition to these, grains of silicon carbide (SiC) are detected, by means of an infrared emission peak at ~ 11 μm.[12] SiC has also been found in meteorites and comet material,[13] but there is no evidence so far for its existence in the ISM; it is thought that this may be due to oxidation of the grains.[14] A general overview of SiC grains in astrophysical environments has been given by Speck *et al*.[15] While the role of SiC in astrophysical catalytic processes has not been explored in great detail, a recent study proposed their involvement in the formation of PAH molecules.[16] It was reported that the annealing of SiC at high temperatures (~ 1200 °C) creates a layer of graphene on its surface, which, through etching by H atoms, would be modified and, it was suggested, fragment to yield PAHs. However, the experimental design means that any PAHs formed could not be detected to confirm the proposed process.

Detailed in this Chapter are experiments carried out to investigate further aspects of analogues of cosmic dust grains, *i.e.* olivine silicates and SiC, with a focus on processes in which they may play catalytic roles. Possible reactions of H_2 and CO over heated olivine-type silicates under vacuum were examined and are described in Section 4.3, in which the astrophysical implications of the reaction products are also discussed. Building on previous work in which PAHs were seen to form from acetylene over silicate grains, pyroxenes and alumina,[11, 17] experiments were carried out to investigate the potential formation of PAHs from acetylene over SiC grains, thereby extending the investigation to carbon-rich objects (Section 4.4). Finally, Section 4.5 details experiments in which the behaviour of olivines under the electron beam (e-beam) in transmission electron microscopy (TEM) was examined, and describes the effects of e-beam irradiation on both 'bare' olivines, and olivines coated with a layer of PAH molecules.

4.2 Experimental details

4.2.1 Experimental apparatus

The experiments carried out for the investigations described in Sections 4.3 and 4.4 made use of apparatus that had been used previously for research into the formation of PAHs from acetylene over silicate grains.[11, 17] A schematic illustration of the experimental apparatus is given in Figure 4.1. The setup consists of a source chamber, in which is housed the reactor – a quartz tube containing a catalyst that is held in place using quartz wool plugs – and which is held at a pressure of ~ 4 × 10^{-6} mbar. Beyond this is an ionisation chamber, kept at ~ 2.6 × 10^{-6} mbar, and a time-of-flight (TOF) tube. Following heating of the catalyst under a flow of argon, the reactant gas of interest is introduced into the apparatus using an electronically controlled pulsed valve. It then passes through the reactor and on exit, along with any gaseous products formed from reactions on the catalyst surface, is passed into the ionisation chamber through a skimmer and in the form of a molecular beam. The beam is then ionised using a laser and finally products are detected using TOF mass spectrometry (TOF MS).

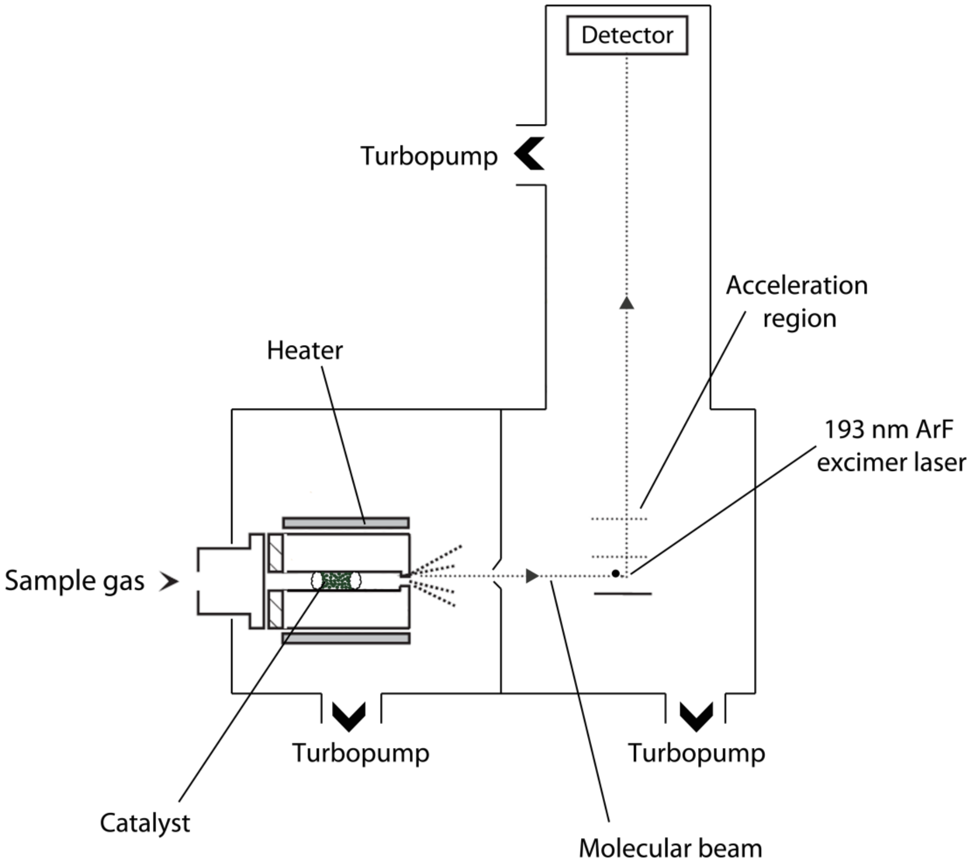

Figure 4.1. Schematic illustration of the experimental apparatus used for work described in Sections 4.3 and 4.4 of this Chapter.

For Section 4.3, the reactant gas used was initially a mixture of H_2 and CO, followed by studies using CO only. Two olivine samples were used as catalytic grain analogues, and the temperature of the sample was varied in the range 400 – 700 °C.

A separate experiment was also carried out which involved a continuous flow of the precursor gas, passed through the reactor at atmospheric pressure. The product-containing gas was then collected by directing it into liquid nitrogen-cooled dichloromethane. The catalyst was removed following the reaction and analysed using TEM. Section 4.4 describes experiments in which acetylene (C_2H_2) was used as the reactant gas and SiC was used as the catalyst. These experiments were carried out at a temperature of 600 °C.

4.2.2 Sample characterisation

TEM imaging for the studies described in Section 4.3.4 was carried out using a TECNAI G2 F20 TEM at an accelerating voltage of 200 kV. Samples were dispersed in ethanol and drop-cast onto lacey carbon coated copper TEM grids (AGAR), before being dried under a flow of N_2 for 1 min. Elemental analysis was conducted using energy dispersive X-ray spectroscopy (EDX). XRD measurements were undertaken using a PANalytical X’Pert PRO diffractometer equipped with Cu-$K\alpha$ radiation (λ = 0.15406 nm, 20 kV, 30 mA). Matrix-assisted laser desorption/ionisation time-of-flight mass spectrometry (MALDI-TOF MS) was carried out using a Bruker Ultraflex III MALDI-TOF mass spectrometer in positive reflection mode. This was equipped with a pulsed Nd:YAG 355 nm laser with 5 ns-duration pulses of ~ 500 µJ pulse^{-1}. Each spectrum was acquired from an average of 200 pulses, and samples were supported on a stainless steel Multiprobe Adapter MALDI target plate. The Raman spectra were recorded on a Horiba–Jobin–Yvon LabRAM HR confocal Raman Microscope equipped with a Synapse CCD detector. The Raman measurements were performed at room temperature using an excitation laser wavelength of 532 nm operating at a power of ca. 10 mW (25%) and a 600 lines/mm grating. The Raman shift was calibrated using the Raleigh peak and the 520.7 cm^{-1} silicon line from a Si(100) reference sample.

4.2.3 TEM experiments

The experiments outlined in Section 4.5 were carried out using a JEOL-2100F TEM at an accelerating voltage of 100 kV. For sample preparation, graphite flakes (~ 1 mg, Fisher Scientific: Graphite powder, Supplier: Fisher Scientific, Code: G/0900/60, Batch: 0438775, Cas No.: 7782-42-5) were dispersed in HPLC-grade isopropyl alcohol (IPA) (4 mL) using an ultrasonic bath, drop-cast (25 drops) onto lacey carbon-coated copper TEM grids (AGAR) and allowed to dry. An olivine sample (~ 0.5 mg) was then dispersed in HPLC-grade IPA (4 mL) using an ultrasonic bath and drop-cast (25 drops) on top of the graphite flakes, before drying the grid under a flow of N_2 gas for 1 min.

For the carbon-coated olivines experiment (Section 4.5.2), the TEM grid preparation method detailed above was repeated, before sealing the grid under vacuum in a pyrex tube, along with a small amount (~ 1 mg) of perylene (obtained from Sigma-Aldrich). The sealed pyrex tube was heated at 500 °C for 1 hour, and then allowed to cool before the grid was collected and used for TEM.

4.3 Reactions of CO and H_2 over silicate grains

The chemical importance of olivine-type silicate grains in space has been demonstrated by their catalytic role in the formation of PAH molecules from acetylene gas.[11] Prior to this, these grains were already thought to play a significant part in the catalytic formation of CO and H_2,[8-10] the two most abundant molecules in the Universe. In this Section, an investigation is carried out in which the catalytic capability of olivine grains is explored further to determine whether these two abundant molecules – CO and H_2 – would themselves undergo any catalytic reactions, as a mixture or on their own, when in the presence of heated olivines.

4.3.1 Characterisation of olivine samples

For the purpose of comparison, two different olivine samples were used as catalytic grains in the experiments reported here. These were provided by the

Geological Museum of the University of Hong Kong and shall be referred to as Olivine A and Olivine B. The two samples were characterised using XRD and EDX. The wide-angle XRD patterns of the two samples indicated that both Olivine A and B have a structure that is typical of magnesium silicates, when compared with the powder diffraction files within the ICDD PDF database. The results of EDX analysis (Figure 4.2) indicated that Olivine A contains 1.75 atomic % Fe, while Olivine B contains 2.62 atomic % Fe. In addition, there are trace amounts of Ca, Zn, Zr and Ni, which are considered to be unimportant.

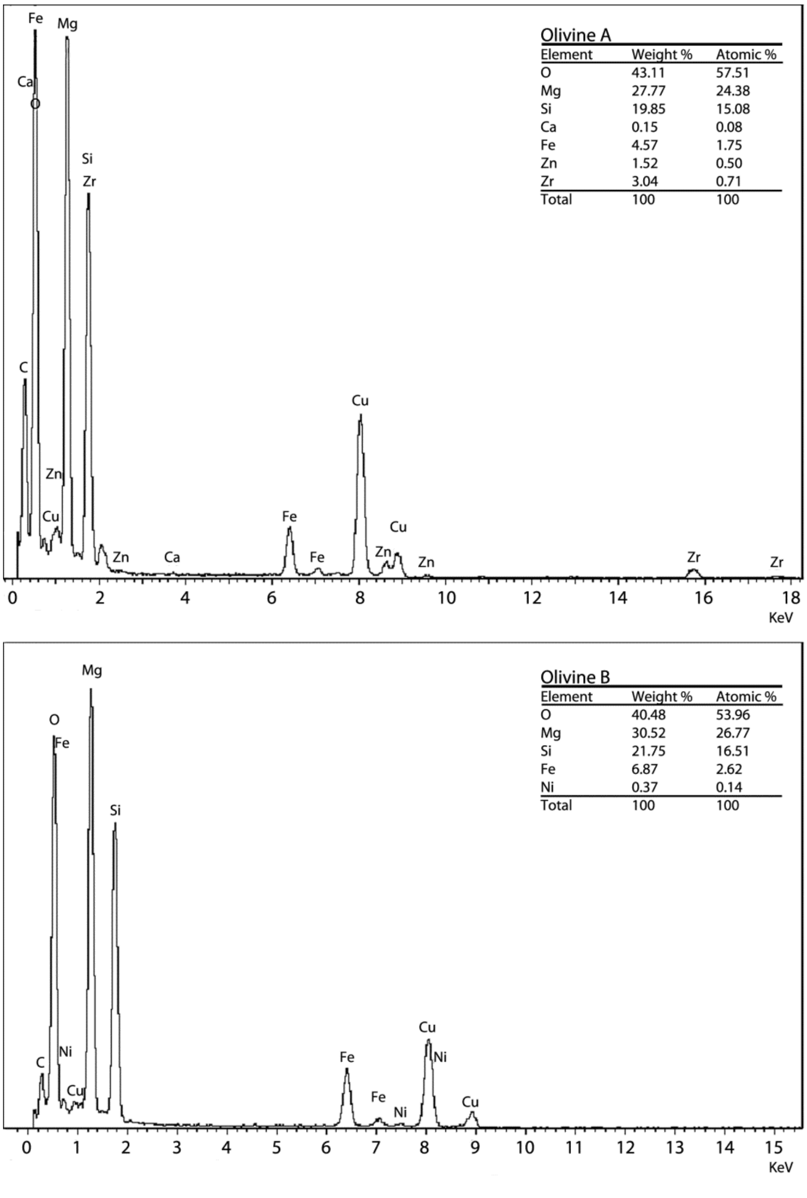

Olivine A

Element	Weight %	Atomic %
O	43.11	57.51
Mg	27.77	24.38
Si	19.85	15.08
Ca	0.15	0.08
Fe	4.57	1.75
Zn	1.52	0.50
Zr	3.04	0.71
Total	100	100

Olivine B

Element	Weight %	Atomic %
O	40.48	53.96
Mg	30.52	26.77
Si	21.75	16.51
Fe	6.87	2.62
Ni	0.37	0.14
Total	100	100

Figure 4.2. EDX spectra of Olivine A (upper panel) and B (lower panel). Copper peaks originate from the TEM sample grid.

4.3.2 Products detected

To investigate the potential reactions of H_2 and CO in the presence of olivine-type silicates, both gases were pulsed into the reactor at a ratio of 5:1 H_2:CO. The initial experiments were carried out at a temperature of 600 °C and were repeated using both Olivine A and Olivine B as catalytic grains. The mass spectra showing the detected species as a result of these experiments are given in Figure 4.3.

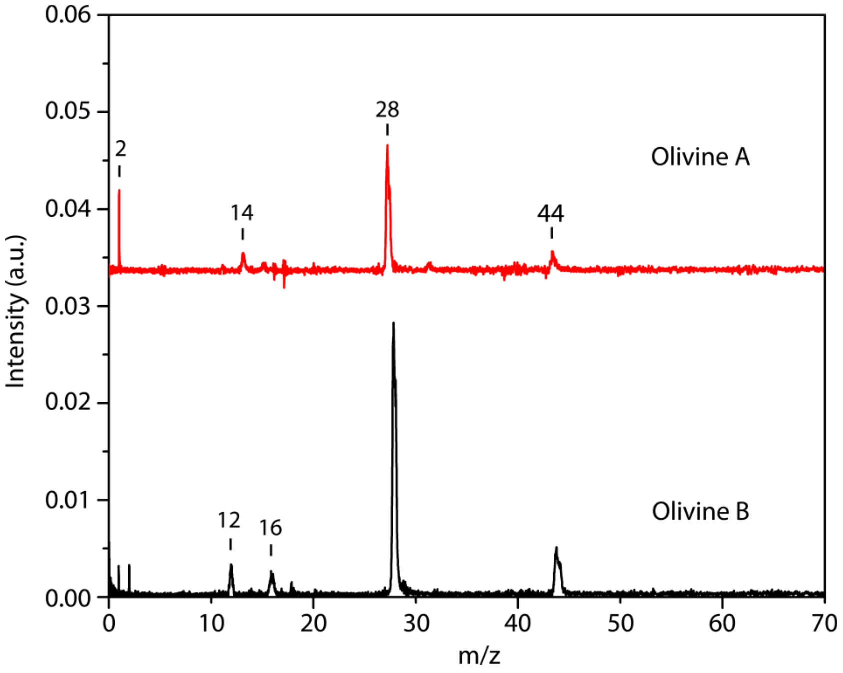

Figure 4.3. Mass spectra resulting from the pulsing of a mixture of H_2 and CO over Olivine A (upper half; red line) and Olivine B (lower half; black line) at 600 °C.

The first deduction that can be made from the results shown in Figure 4.3 is that only one newly formed species is detected; there are peaks at m/z = 2, 12, 14, 16 and 28 which correspond to H_2, C, N (which is likely a contaminant), O and CO, respectively. The only peak not readily assigned is that which falls at m/z = 44. In order to assist with the identification of the product being detected at this m/z value, the experiments were repeated using only CO as the precursor gas, to determine if the product was a result of the two gases reacting, or if H_2 has an effect on its production. The mass spectra resulting from this test experiment are given in Figure 4.4, which shows that in the absence of H_2, there is still a product detected at m/z = 44. It can be inferred, therefore, that under these conditions H_2 and CO do not react with each other, and that the species being detected at *m/z* = 44 is produced as a result of reactions involving only one of these precursor gases.

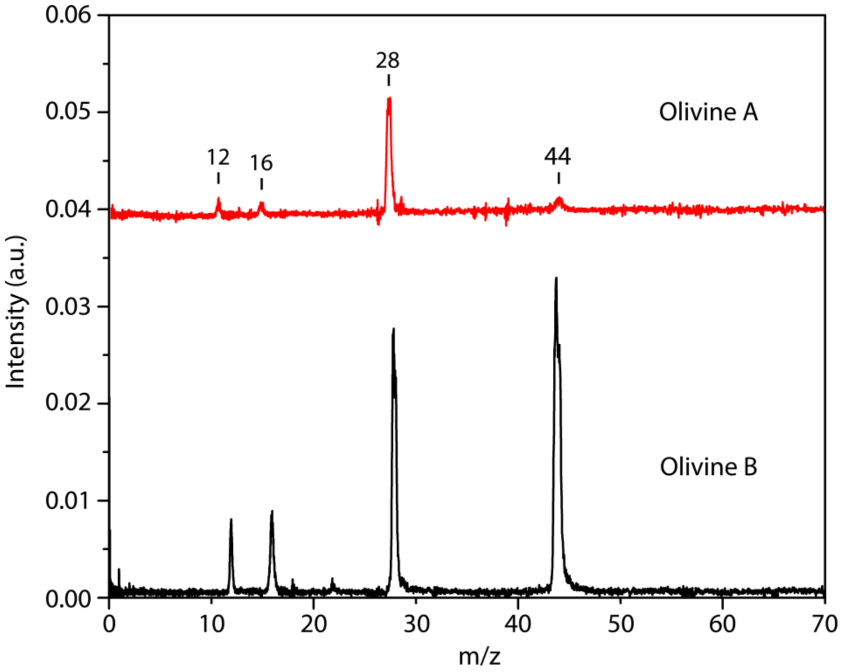

Figure 4.4. Mass spectra resulting from the pulsing of CO over Olivine A (upper half; red line) and Olivine B (lower half; black line) at 600 °C.

In order to confirm that the detected product was a result of reactions that are catalysed by the olivine samples, and not just a contaminant in the gas, a control experiment was carried out that replaced the olivine catalyst with SiO_2, to replicate the quartz housing and wool used in the reactor. The resultant mass spectrum for the control reaction is given in Figure 4.5 and shows only a peak at *m/z* = 28, corresponding to the CO gas, confirming that the species detected at *m/z* = 44 is not an impurity within the gas, and that no reactions are occurring in the absence of the silicate catalyst. It is proposed that the product that is being formed and detected at *m/z* = 44 is CO_2, produced *via* the CO disproportionation reaction. This process produces, as its second product, solid carbon, which is deposited onto the catalyst surface. The assignment of this peak to gaseous CO_2 as a result of CO disproportionation is supported by the fact that a colour change of the catalyst was observed following the reaction, in addition to a slight increase in its mass; these are both effects that suggest the deposition of solid state carbon on the surface of the olivine grains.

The CO disproportion reaction is discussed further in Section 4.3.3 and the nature of the carbon deposition in Section 4.3.4. Experiments that were carried out following this assignment used only CO as the precursor gas, as it was apparent that H_2 had no involvement in any reactions under these conditions.

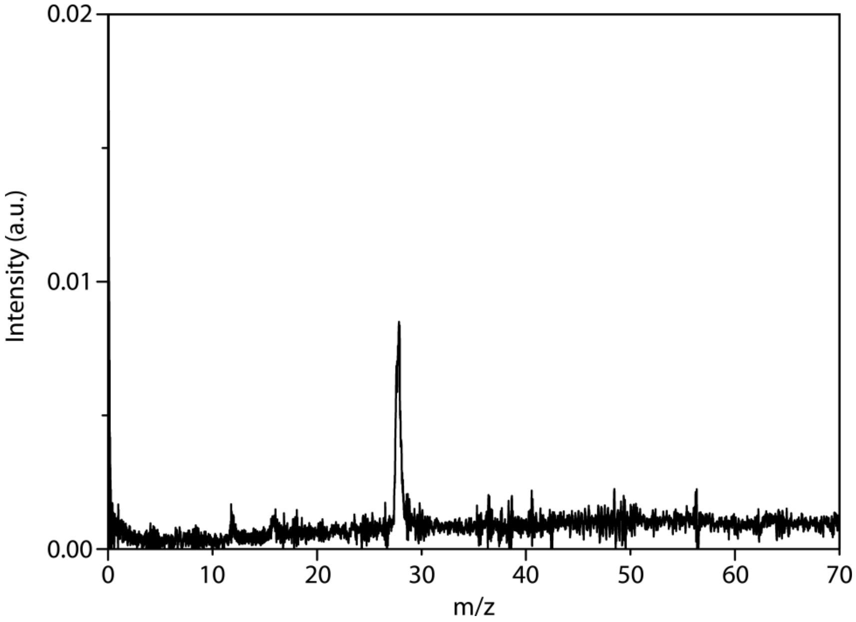

Figure 4.5. Mass spectrum resulting from the pulsing of CO over SiO_2 at 600 °C as a control experiment.

Following the assignment of the peak at *m/z* = 44 to CO_2 – a product of CO disproportionation catalysed by olivine grains, experimental conditions were varied to determine the influence of temperature and time on the formation of this product. Figure 4.6 presents the mass spectra resulting from the pulsing of CO over Olivine B at a range of temperatures between 450 and 700 °C at intervals of 50 °C. It is seen from this figure that CO_2 is efficiently produced at each temperature within the range, with the highest intensity peak occurring for the reaction at 600 °C. These results indicate that CO disproportionation takes place readily at any of the temperatures within the range investigated. Experiments following this continued to be run at a temperature of 600 °C.

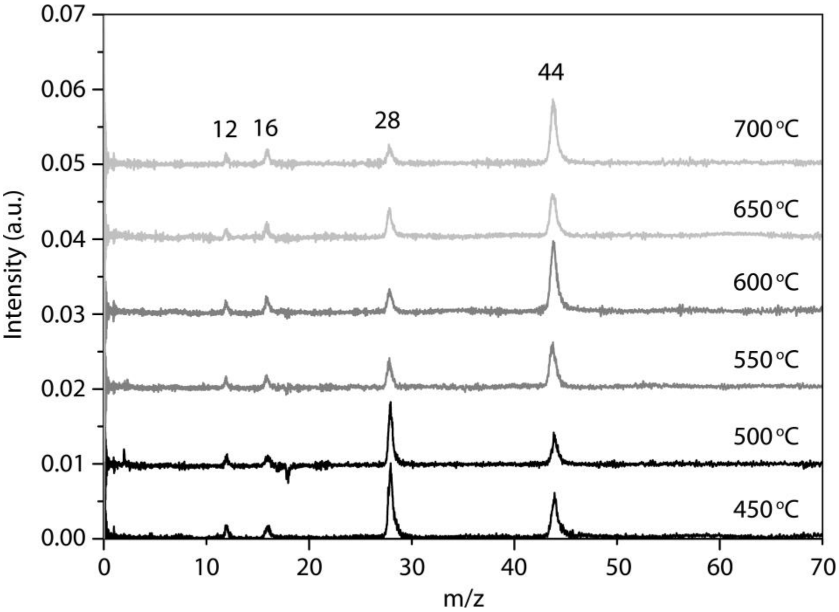

Figure 4.6. Mass spectra resulting from the pulsing of CO over Olivine B at different temperatures.

Figure 4.7 gives the resultant mass spectra following experiments that were carried out to determine how the formation of CO_2 under these conditions varies over time. For these experiments, CO was pulsed over Olivines A and B at 600 °C for an extended period, and mass spectra were recorded at various time intervals. It can be seen in Figure 4.7, for the experiment that was carried out using Olivine B, that over the first 10 minutes the peak at m/z = 44 decreases in intensity, indicating a steady decrease in the amount of CO_2 being produced. After 20 minutes the peak had a very low intensity, and at 40 minutes, CO_2 was barely detected. This decrease in the production of CO_2 over time was accompanied by an increase in the intensity of the peak at m/z = 28, corresponding to an increased amount of CO passing through the reactor unaffected. It is proposed that this occurs as a result of catalyst deactivation, which is likely due to the deposition of solid state carbon covering active sites on the catalyst surface, reducing the chance of reaction and resulting in a gradual decline in the amount of CO_2 produced.

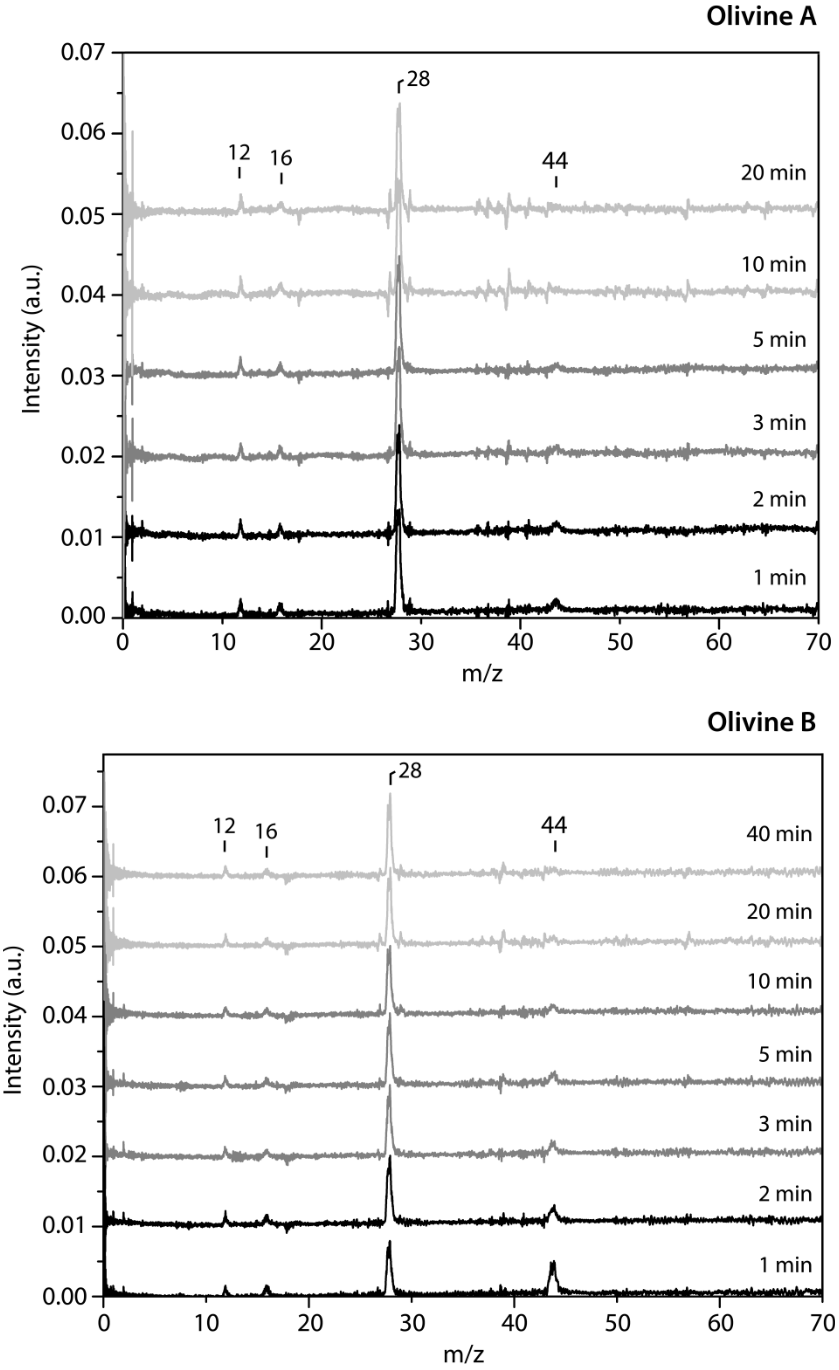

Figure 4.7. Mass spectra recorded at certain time intervals, resulting from the pulsing of CO over Olivine A (upper panel) and Olivine B (lower panel) at 600 °C.

When the experiment was carried out using Olivine A, it can be seen in Figure 4.7 that after only 10 minutes there was almost no CO_2 detected. This indicates that catalyst deactivation occurs more quickly for Olivine A than for Olivine B, suggesting that Olivine B may contain a higher number of active sites on its surface, and hence requires more time before they are deactivated by the carbon deposition.

It is interesting to note the apparent difference between the two olivines. In addition to the difference in the deactivation time, with Olivine A becoming deactivated more quickly than Olivine B, it can be seen from Figure 4.4 that far more CO_2 is produced when carrying out the reaction using Olivine B as the catalyst than when using Olivine A. These differences imply that Olivine B is more efficient as a catalyst for the CO disproportionation reaction. Olivines, with the general formula $(Mg,Fe)_2SiO_4$, differ according to the proportion of magnesium and iron that they contain. Indeed, the main difference between Olivine A and Olivine B, according to the EDX spectrum shown in Figure 4.2, is the content of iron contained in each.

The difference in Fe content may account for the difference in the observed intensity of the $m/z = 44$ peak, corresponding to the amount of CO_2 produced. If this is the case then it suggests that Fe is a key component of the catalyst in this reaction, and it may be that the active catalytic sites are Fe-based. This would then explain the higher deactivation of Olivine A, which contains a lower Fe percentage (1.75 Atomic %) than Olivine B (2.62 Atomic %).

4.3.3 CO disproportionation

The disproportionation of CO to form CO_2 and solid C is a reversible process known as the Boudouard reaction,[18] and is shown below:

$$2\mathrm{CO}_{(g)} \rightleftharpoons \mathrm{CO_2}_{(g)} + \mathrm{C}_{(s)}$$

The formation of solid state carbon in this reaction may be seen as unfavourable in some industrial processes, as its deposition shortens the life of the catalyst; however, the Boudouard reaction has also been used for the production of solid carbon. For example, graphite, in various forms,[19, 20] and carbon nanotubes[21-23] have been produced in this way, using catalytic metals such as Mg, Fe, Co, Ni, and Mo. In the presence of hydrogen, the process could produce methane, the product of a reaction between the hydrogen with the surface-deposited carbon, effectively ‘cleaning’ the surface of the catalyst.

In astrophysical terms, CO acts as a sink for the carbon and oxygen produced in a star. It is the second most abundant molecule, following H_2, and is very stable; as such, CO has not been widely considered as a carbon source for the formation of other carbon-based species such as PAHs or fullerenes. One exception is a piece of work in which the Boudouard reaction is proposed to be the route to formation of carbon cages, deposited onto TiC grain cores,[24] forming the TiC core-graphitic mantle spherules that had previously been discovered in the Murchison carbonaceous meteorite.[25] The authors suggest that because the Boudouard reaction is catalysed by small metallic particles, this process could also occur easily around AGB stars.

To date, it appears there are no reports of the Boudouard reaction being catalysed by silicate particles such as olivines, despite the fact that they contain Mg and Fe, which are both metals that have been used, in other forms, for these reactions in the past. The results presented in this Section provide evidence that suggests that in astrophysical environments in which these olivine silicates are known to exist, and at certain temperatures, CO disproportionation may be occurring.

4.3.4 Carbon deposition on the catalyst surface

Due to the occurrence of CO disproportionation in the experiments reported in Section 4.3.2, which involve all of the astrophysically relevant components, the form of the carbon deposited on the surface of the olivine grains is of interest. To investigate this, characterisation of the olivine samples following the reaction was carried out using Raman spectroscopy, MALDI-TOF MS, and TEM.

Figure 4.8 shows the Raman spectra of Olivine B before and after the CO disproportionation reaction. The spectrum of the sample before the reaction (black line) can be seen to be a typical Raman spectrum of olivine, its dominant feature being a doublet with one peak in the range 815 – 825 cm^{-1}, assigned to an asymmetric SiO stretching vibration with A_g symmetry, and another in the range 838 – 857 cm^{-1}, assigned to the corresponding symmetric vibration. The wavenumbers of these peaks are seen to vary depending on the Mg and Fe content of the sample.[26]

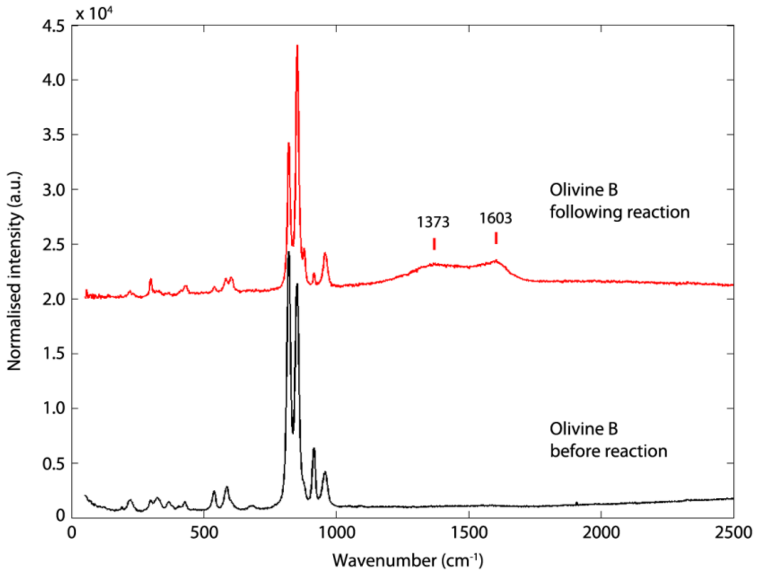

Figure 4.8. Raman spectra of Olivine B before (black; lower line) and following (red; upper line) CO disproportionation.

Following the reaction (red line in Figure 4.8) two additional, broad peaks can be seen at 1373 cm^{-1} and 1603 cm^{-1}. These can be assigned to the D (defect) and G (graphite) bands of amorphous carbon,[27] and confirm the deposition of solid state carbon on the catalyst surface. These additional peaks are accompanied by a decrease in intensity of two of the original olivine peaks, at 820 cm^{-1} and 916 cm^{-1}, which may occur as a result of the new surface-deposited carbon suppressing the vibrational modes at these frequencies. The spectra given in Figure 4.8 indicate that the deposited carbon is amorphous in nature with graphitic domains of sp^2-hybridised carbon, as evidenced by the presence of the G band. The ratio of the intensity of the D and G bands (I_D/I_G) in this case is high, at 0.89, indicating that the distance between graphitic domains within the sample is large. The spectra show no evidence for the presence of discrete carbon nanostructures; the absence of a second fundamental overtone of the D band (*i.e.* a 2D band) at ~ 2746 cm^{-1}, which would be diagnostic of structures containing highly ordered graphitic carbon, provides support for the notion that this sample only contains amorphous carbon with small graphitic domains. A reasonably large area of a sample is irradiated during Raman spectroscopy, and as such the formation of a small number of specific carbon nanostructures cannot be entirely discounted. For instance, a low concentration of formed nanotubes or fullerenes would perhaps not produce peaks that are sufficiently intense to be easily detected above the olivine and amorphous carbon peaks.

Figure 4.9 presents the MALDI-TOF mass spectra of Olivine B before (green line), and following (red line), the CO disproportionation reaction, shown alongside a mass spectrum taken of the blank MALDI target plate. The main result that can be seen from these spectra is the appearance of a new peak, following the reaction, at *m/z* = 720, corresponding to the fullerene C_{60}. This peak provides more evidence for the deposition of carbon on the surface of the olivine. It can arise either from desorption of already-formed fullerenes from the surface of the catalyst, or desorption of small carbon fragments, from amorphous or graphitic carbon, which then come together to form the fullerene molecule in the gas phase, before being detected. Because either of these situations is likely to occur, these results do not provide an absolute identification for the form of carbon on the olivine surface.

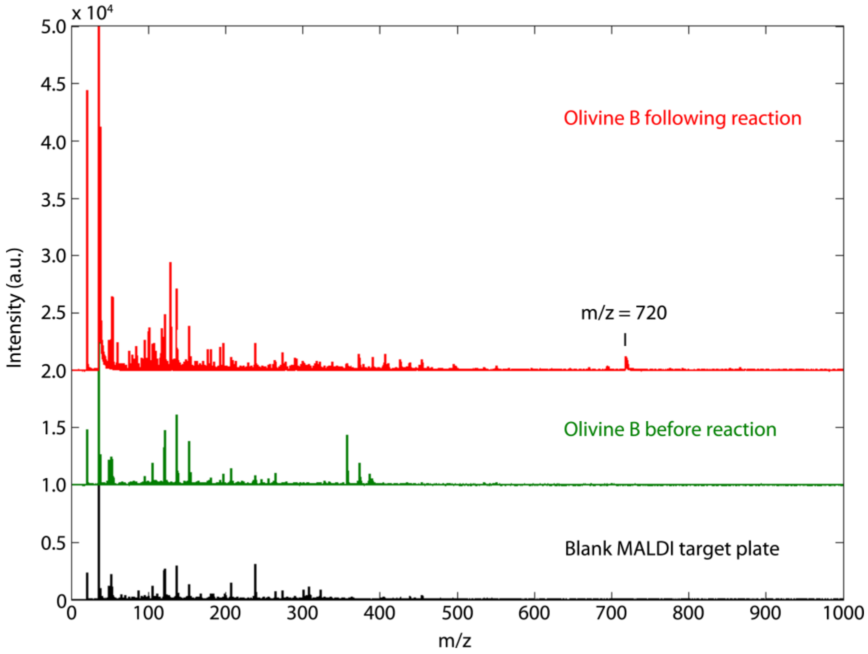

Figure 4.9. Mass spectra of the blank MALDI-TOF target plate (lower spectrum; black line), Olivine B before any experiment (middle spectrum; green line), and Olivine B following CO disproportionation (upper spectrum; red line).

TEM imaging was carried out on Olivine B before and following the CO disproportionation reaction. The images obtained from this are presented in Figure 4.10, in which, following the reaction, a significant amount of amorphous carbon can be seen on the edge of the olivine when compared with the image obtained before the reaction. There is also a notable absence of any ordered structures such as graphitic layers, fullerenes or carbon nanotubes. The formation of ordered structures such as these cannot be completely ruled out, as only a very small area of sample is analysed in TEM. However, the images in Figure 4.10 in combination with the Raman analysis given in Figure 4.8 suggest that the deposition of amorphous carbon is representative of the majority of the sample.

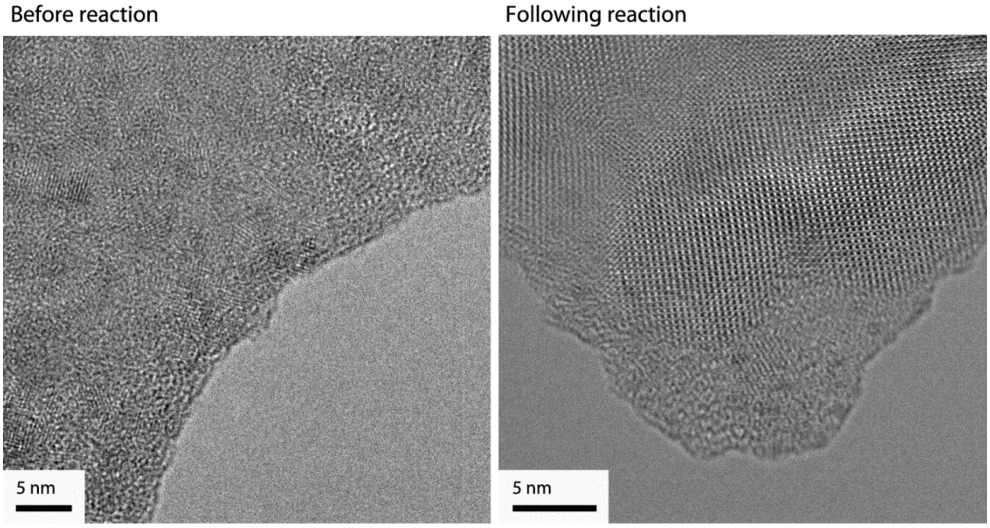

Figure 4.10. TEM images of Olivine B before (left), and following (right) CO disproportionation within experiments carried out under vacuum.

For the purpose of comparison, experiments were carried out in which a continuous flow of CO was passed through the reactor containing Olivine A or Olivine B under atmospheric pressure at 600 °C. TEM images of the olivine catalysts were acquired following these experiments and the expected CO disproportionation reaction, and these are presented in Figure 4.11. It can be seen in these images that two main types of carbon deposition have occurred. The left hand panels for both Olivine A and B show the formation of graphitic layers, or ‘carbon onion’ type structures, while the right hand panels show the formation of multi-walled carbon nanotubes (MWNTs). In the right hand panel for Olivine A, material can be seen from which the MWNT appears to have grown. This material has a darker contrast than the carbon of the nanotube, indicating a heavier element such as Fe – which is commonly used as a catalyst for nanotube growth.[28] The formation of iron nanoparticles is very important for the catalysis of nanotube formation; Section 4.5 discusses the irradiation-induced formation of iron nanoparticles from olivine samples and the implications for nanotube growth in astrophysical environments.

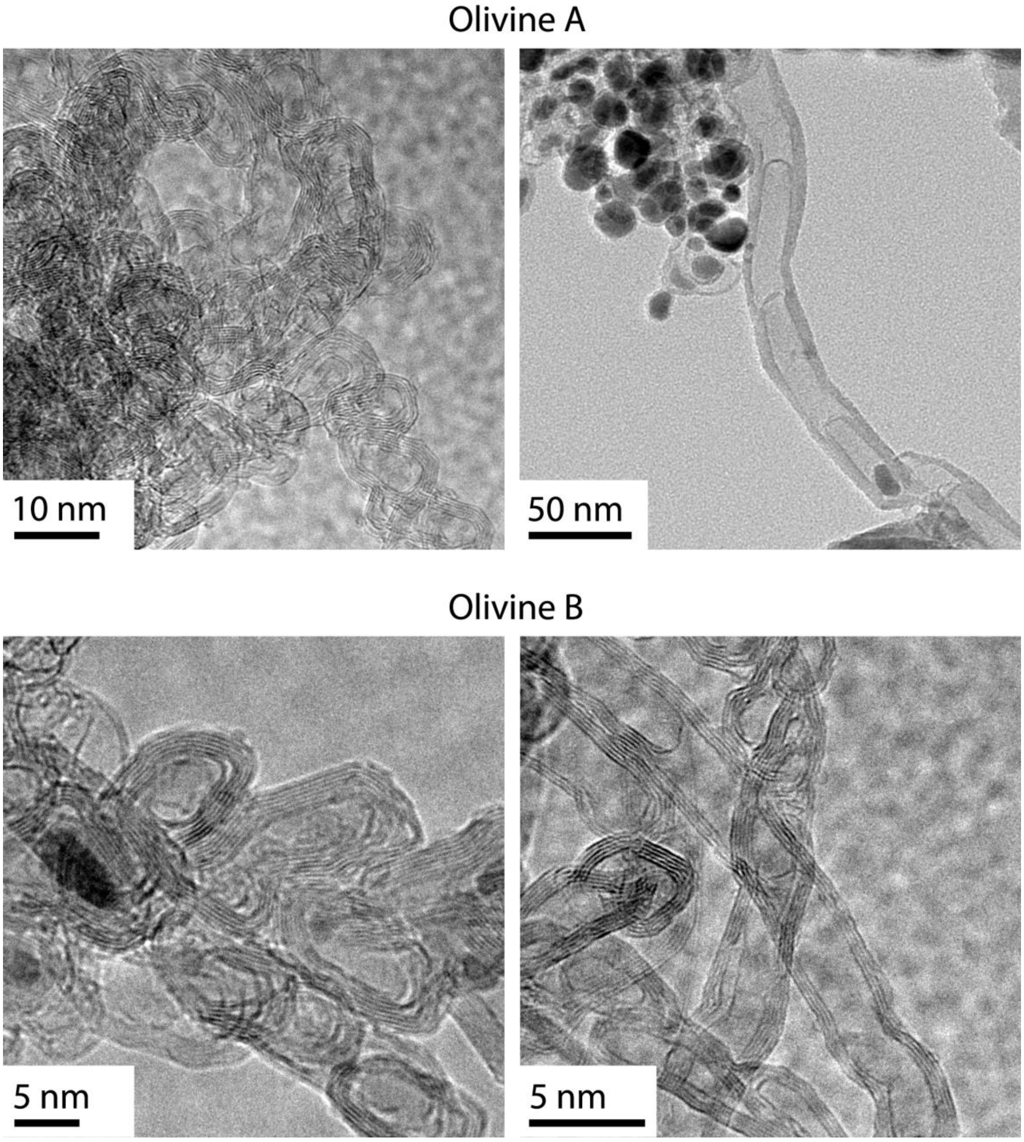

Figure 4.11. TEM images of Olivine A (upper two panels) and Olivine B (lower two panels) following CO disproportionation at atmospheric pressure.

There is a stark contrast between the images taken of the material following the experiments carried out under vacuum (Figure 4.10) and those run at atmospheric pressure (Figure 4.11), the former showing only amorphous carbon and the latter presenting more highly ordered graphitic structures and nanotubes. It is most likely that this difference is a result of the differing amount of material that is passing over the catalytic grains in each case, and therefore the amount of carbon available for deposition. Due to the low pressure of the experiments under vacuum, there would simply not be enough carbon to form nanotubes of the magnitude seen from the atmospheric pressure experiments.

The formation of graphitic layers and MWNTs is a significant result. Although these are only seen in the case of the experiments run at atmospheric pressure, which is not directly applicable to astrophysical environments, in space there are far longer timescales over which these processes can occur. This means that over many years in interstellar environments, as opposed to a matter of minutes in the laboratory, it is feasible that structures such as these graphitic layers and MWNTs could be forming on silicate grains.

4.3.5 Astrophysical implications

As shown in Section 4.3.4, experiments carried out under vacuum resulted in the deposition of amorphous carbon onto the olivine surface, and those carried out at atmospheric pressure showed formation of graphitic layers and MWNTs. A scheme summarising the products that are seen to form and may be expected to form is shown in Figure 4.12, and the products are discussed in this Section.

While the conditions of the experiments carried out under vacuum are perhaps more relevant to astrophysical conditions, those carried out at atmospheric pressure could be feasible over much longer timescales in space than those that hold in the laboratory. Examples of both forms of carbon deposition may then be expected, and in each case, a new source of carbon has been formed. If exposed to UV irradiation, shocks or cosmic rays, small carbon fragments are expected to be ejected from the amorphous deposit on the olivine surface, which could then go on to build up and form larger species, as is seen during MALDI-TOF MS of the material (Figure 4.9), which shows the formation of C_{60}. Similarly, the small graphitic domains in the amorphous material, identified by Raman spectroscopy (Figure 4.8) could be a source of aromatic material which, when broken up, can form PAH molecules.

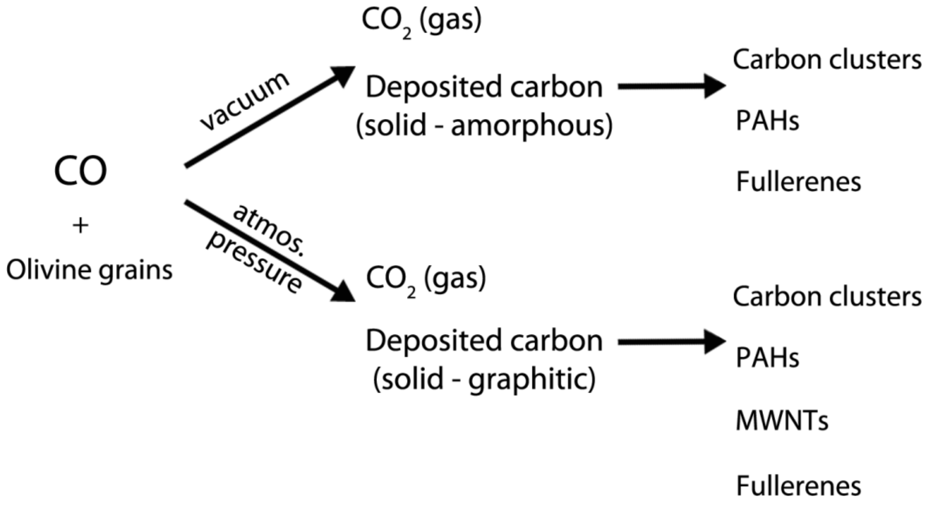

Figure 4.12. Scheme showing CO disproportionation over olivine grains when carried out under vacuum or at atmospheric pressure, including the products that are seen to form and those that may be expected.

If, in astrophysical environments, CO disproportionation over olivine-type grains occurs over sufficiently long timescales, then graphitic layers of deposited carbon may be expected. These would form an important reservoir of aromatic material that survives out into the ISM and from which larger PAH molecules can originate following the exposure of the graphitic layers to cosmic rays, shocks, or UV irradiation. In this way, the material may contribute to the PAH population in space. For example, the Red Rectangle – a so-called ‘mixed chemistry’ object – exhibits the spectral features of both crystalline olivine-type silicate grains and of PAH molecules. Previously, it has been shown that PAHs can form from acetylene gas over olivine grains,[11] thus providing an important route to PAH formation – in particular small PAHs – within objects such as the Red Rectangle. The breaking off of graphitic layers deposited on olivines may provide an additional path to the formation of PAHs, and could be responsible particularly for the larger PAH molecules within the population.

The formation and growth of multi-walled carbon nanotubes, given a sufficiently high concentration of carbon and enough time, is a significant result when considering the potential of these reactions occurring in space. To date, there has been no confirmation of the existence of carbon nanotubes in astrophysical environments, although the first detection[29-31] of the fullerene C_{60} triggered the notion that nanotubes and other carbon nanostructures should be expected and may well be detected in the future.[32] The issue in detecting carbon nanotubes spectroscopically is that a population of these structures is likely to contain a huge variety of characteristics, such as their diameters, chirality, the number of 'walls' – *i.e.* single-walled or multi-walled – and the nature of the ends of the tubes. As such, rather than a single spectral signature, a very broad range of frequencies would be expected, making nanotubes very difficult to identify in astronomical spectra. While the detection and identification of carbon nanotubes will continue to be a hurdle for some time, the results presented in this Chapter provide compelling evidence that structures such as these should be expected to exist in space. With a steady supply of carbon, from CO disproportionation for example, it is feasible that in the presence of catalysts such as the olivines used in these experiments, the growth of carbon nanotubes would occur. As mentioned in Section 4.3.3, CO disproportionation over certain metal-containing catalysts has been used specifically in the formation of carbon nanotubes,[21-23] demonstrating the ease with which this process can occur, with enough time.

Along with oxygen-rich silicates and carbon-rich PAHs, gaseous CO_2 has also been detected, in absorption, in the Red Rectangle.[7] The formation of CO_2 in the CO disproportionation reaction over olivines is therefore significant in the context of this object in particular, as it is from this reaction that the detected CO_2 probably originates. To add support to this, the absorption feature of CO_2 was detected within the circumbinary disc of the Red Rectangle, where the olivine-type silicates are also detected,[7] indicating that the CO_2 is formed in close proximity to the silicate grains.

4.4 The formation of PAHs over SiC

While olivine-type silicates continue to demonstrate their importance in catalytic chemical processes, as evidenced by the results described in the previous Section and by their role in the formation of PAHs from acetylene gas,[11] these dust grains would only be expected in mixed-chemistry or oxygen-rich objects in space. A question remains, therefore, as to the formation of PAHs within carbon-rich environments. To investigate this, this Section describes experiments that were carried out using SiC as a catalytic surface, and acetylene as a precursor.

With the exception of a recent study that proposed the formation of PAHs *via* etching of graphene layers on the annealed surface of SiC grains,[16] little attention has been given to SiC in the context of PAH formation. The experiments undertaken in this Section were carried out to determine whether SiC grains would act as a catalytic surface on which PAHs could form from acetylene, in a way similar to that which has been seen when using olivine-type silicates.

4.4.1 Products detected

Acetylene gas was pulsed into the reactor containing SiC grains at a temperature of 600 °C. The mass spectrum showing the detected species as a result of this experiment is presented in Figure 4.13.

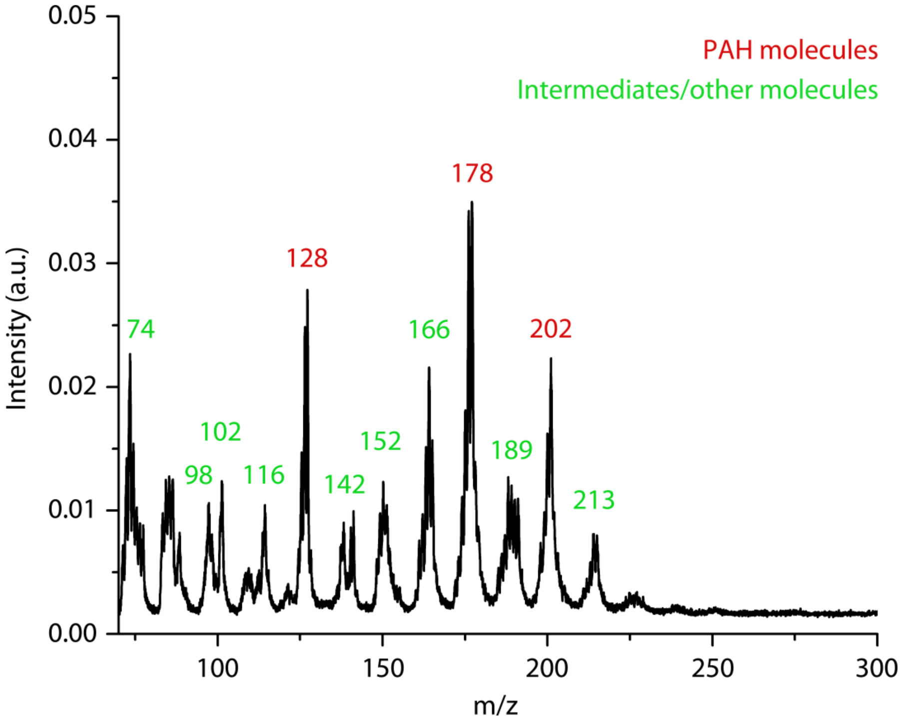

Figure 4.13. Mass spectrum resulting from the pulsing of C_2H_2 over SiC at 600 °C.

It can be seen from Figure 4.13 that a number of species formed from acetylene have been detected. Table 4.1 lists the *m/z* values and assignments of these detected species, and it is found that three well-known, small PAHs have formed – naphthalene, anthracene or phenanthrene, and pyrene. Along with these PAH molecules a number of other molecules are detected which are assigned to acetylene-containing, pentagon-containing, and PAH-type structures, all of which are likely intermediate species in the formation of PAHs from acetylene.

The results presented here demonstrate that PAH molecules can form from acetylene in the presence of SiC grains, in a similar way to that which has been shown previously, using silicate catalysts.[11, 17] This is significant in the consideration of the origin of PAHs in carbon-rich, as opposed to mixed-chemistry, objects. It has also been found, in separate TEM experiments, that following the reaction of acetylene to form PAHs, the SiC catalyst exhibited graphitic layers of carbon on its surface.[33] This carbon coating may provide a route, *via* breaking up of the graphitic layers, to larger PAH molecules; these are detected in the ISM *via* the aromatic infrared bands (AIBs). The formation of these graphitic layers on SiC grains may also offer an explanation for the apparent absence of the 11.3 μm absorption feature of SiC in the ISM, which may be suppressed by the surface coating.

Table 4.1. *m/z* values and assignments of the main peaks seen in Figure 4.13 presented as chemical formulae, names and structures.

m/z	Formula	Name	Structure
74	C_6H_2	Triacetylene	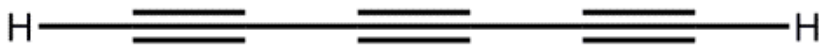
98	C_8H_2	Tetraacetylene	
102	C_8H_6	Phenylethylene	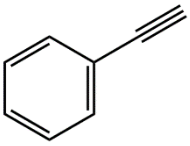
116	C_9H_8	Indene	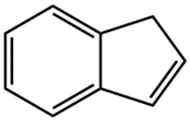
128	$C_{10}H_8$	Naphthalene	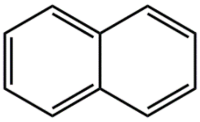
142	$C_{11}H_{10}$	Methylnaphthalene	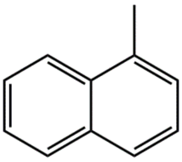
152	$C_{12}H_8$	Acenaphthalene	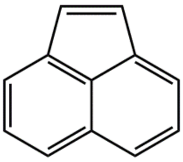
166	$C_{13}H_{10}$	Fluorene	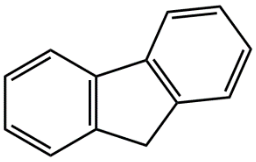
178	$C_{14}H_{10}$	Anthracene/phenanthrene	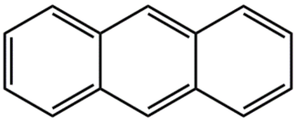 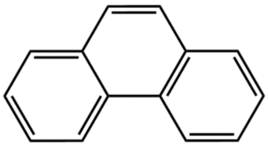
189	$C_{15}H_9$	Fluorenylacetylene	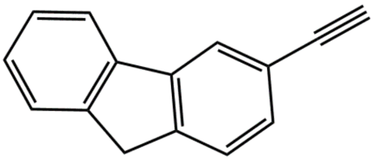
202	$C_{16}H_{10}$	Pyrene	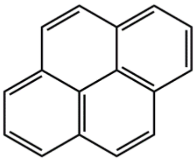
213	$C_{17}H_9$	Fluorenyldiethynyl	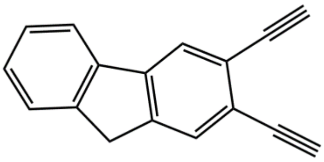

4.5 The behaviour of silicate grains under irradiation

4.5.1 Olivines in TEM

As crystalline olivine-type silicates have been identified in objects such as the Red Rectangle,[7] and appear to play an important role in catalytic reactions as demonstrated throughout this Chapter, their behaviour under the irradiation of the e-beam in TEM was investigated. This investigation was carried out to determine whether any changes in an olivine sample might be expected in astrophysical environments, either under harsh irradiation or over long timescales under less intense radiation.

The irradiation of olivine samples has been previously investigated to some extent, mainly in the context of 'space weathering' – which is the alteration of planet surface materials, both physically and chemically, such that their optical spectra are changed.[34] Space weathering can occur due to bombardment of the materials by ions, energetic electrons, photons, or cosmic rays, and some experiments have been carried out to mimic this on olivine samples using pulsed laser irradiation,[34, 35] and He^+ ions.[36] The results of these studies revealed the formation of Fe nanoparticles, which were proposed to be at least partly responsible for the altered optical spectra. The experiments described in this Section used the e-beam of TEM as a form of irradiation and are focussed on the structural changes of the sample.

An olivine sample was irradiated by the e-beam in TEM, at an accelerating voltage of 100 kV, for approximately 15 minutes with images being taken periodically. These are given in Figure 4.14, in which significant changes in the sample, which was very unstable under the electron beam, are observed.

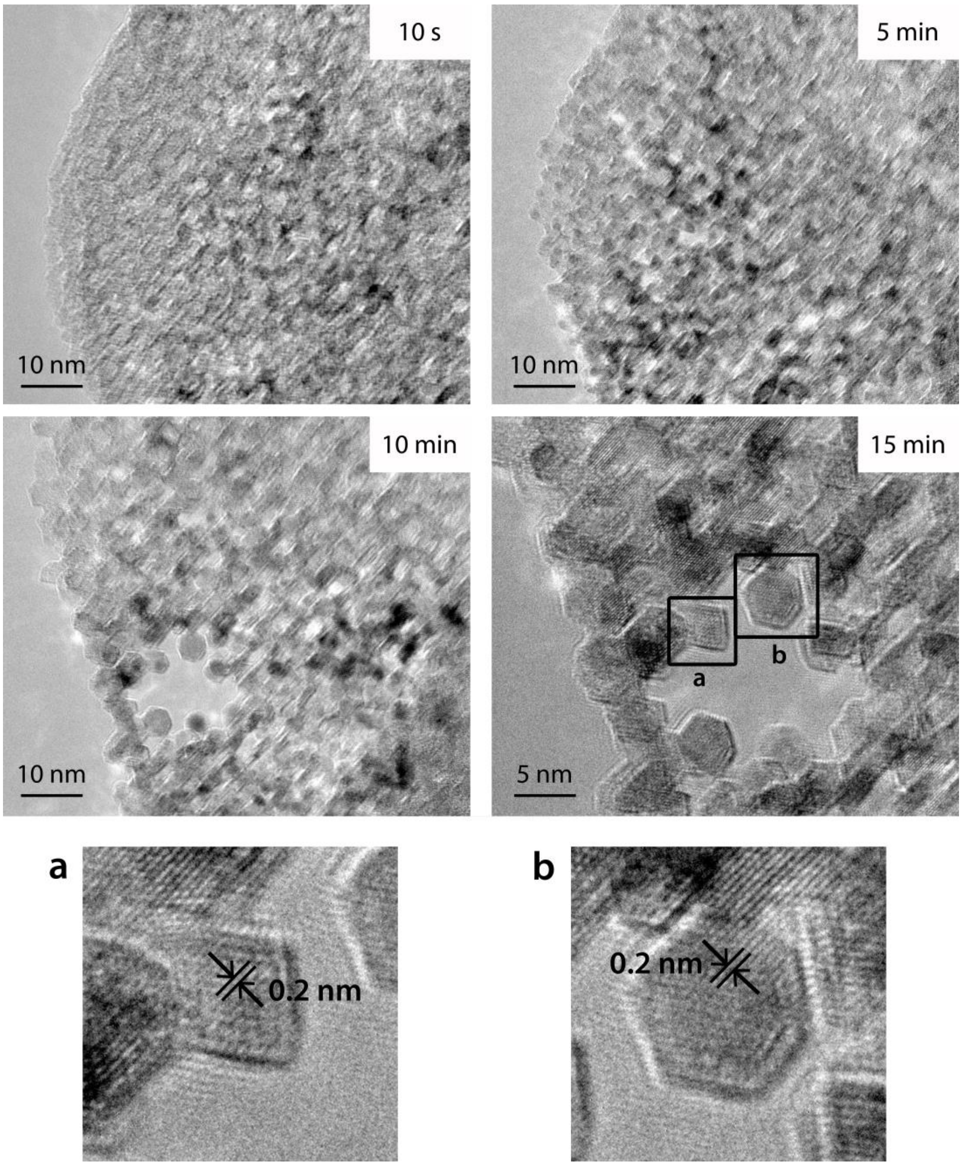

Figure 4.14. TEM images showing the 100 keV e-beam irradiation of an olivine sample over time. Nanoparticles are seen to form, two of which are highlighted by the black boxes (a and b) and shown at higher magnification with their measured interplanar spacing labelled.

It can be seen in Figure 4.14 that within the first five minutes of irradiation, there is a build-up of dark areas within the sample, corresponding to the grouping together of heavier atoms, which have a higher contrast in TEM. Over time, instability of the sample becomes apparent as observed in changes to the edge of the area of the sample being viewed; it can be seen that the sample is almost ‘etched’ away at the edges, and there are more clearly defined, geometric structures throughout the sample. After 10 minutes, a hole can be seen to have formed within the sample, around which are a number of well-defined shapes. These are characterised as nanoparticles, and in the fourth frame of the time series, at 15 minutes, the lines corresponding to the lattice spacing can be seen (see also the magnified images at the bottom of Figure 4.14).

The formation of nanoparticles from the olivine sample under these conditions is proposed to occur as a result of the insulating nature of the silicate. As electrons are knocked from the sample by the e-beam, a build-up of the holes that are left result in the sample becoming very unstable. The heavier elements (Mg, Fe) are left to group together, and they are then likely to be reduced to form the nanoparticles that are then seen. To assist with identification of the nanoparticles seen in the images, EDX spectra were recorded at the beginning and at the end of the period of irradiation. The atomic percentages obtained are listed in Table 4.2.

Table 4.2. Atomic % values obtained using EDX spectroscopy on the olivine sample shown in Figure 4.14 at the beginning and the end of the time series of images.

	Atomic %	
Element	Beginning	End
C	2.3	3.2
O	50.9	37.8
Mg	32.9	33.5
Si	6.9	1.1
Fe	7.0	24.4

The values given in Table 4.2 indicate that over the course of irradiation, the amounts of Si and O have decreased significantly, and that there is a large increase in the amount of Fe. The formation of Fe nanoparticles under these conditions would not be unexpected, considering the results of earlier work in which alternative forms of irradiation were used to bombard olivine samples.[34-36] However, the fact that by the end of the irradiation period there remain significant amounts of Mg, O and Fe suggests that there is more than one type of nanoparticle in the final image of the time series shown in Figure 4.14.

It is proposed that due to the 1:1 ratio of the atomic percentage values of Mg and O seen in Table 4.2, both Fe nanoparticles and MgO nanoparticles would be expected in the sample at the end of the time series. The interplanar *d*-

spacing of a crystal lattice plane (110) of α-Fe is 0.203 nm,[34] and that of a (200) plane of MgO is 0.21 nm.[37] The measured interplanar *d*-spacing shown in Figure 4.14 is found to be ~ 0.2 nm for each of the two nanoparticles highlighted, which is very close to the value for both Fe and MgO nanoparticles. Unfortunately, due to the resolution of the TEM instrument used (which is around 0.2 nm), it is not possible to determine the *d*-spacing with any higher accuracy, and hence if both types of nanoparticle are present, they cannot be distinguished in this way only. However, taking the EDX results in Table 4.2 in combination with the measured *d*-spacing, it can be safely concluded that the final image of the time series shown in Figure 4.14 contains both Fe and MgO nanoparticles.

The structural changes of olivines under e-beam irradiation are interesting when considering catalysed reactions in addition to those already discussed. Fe in particular is associated with the synthesis of carbon nanotubes,[28] and so it is feasible that any carbon adsorbed onto the ‘olivine’ (following irradiation and the consequent nanoparticle formation) surface can undergo reactions to form other carbon-based structures, such as nanotubes.

4.5.2 PAHs and olivines in TEM

As seen in Section 4.3, certain reactions on olivine surfaces, in locations where they are still expected to have their original structure (e.g. the Red Rectangle), can result in a coating of carbon on a grain, having been deposited as a reaction product. Experiments were therefore also carried out in which a carbon-coated olivine sample was irradiated in TEM, to determine whether the behaviour of the sample under the e-beam differs from that described in Section 4.5.1, in which ‘bare’ olivines were used.

An olivine sample deposited on a TEM grid was coated in carbon using gas-phase deposition of the PAH perylene, as detailed in Section 4.2.3. The experiment was carried out using the same conditions as described earlier, in which the sample was irradiated for approximately 15 minutes, with the TEM set at an accelerating voltage of 100 kV. The images from this time series are presented in Figure 4.15.

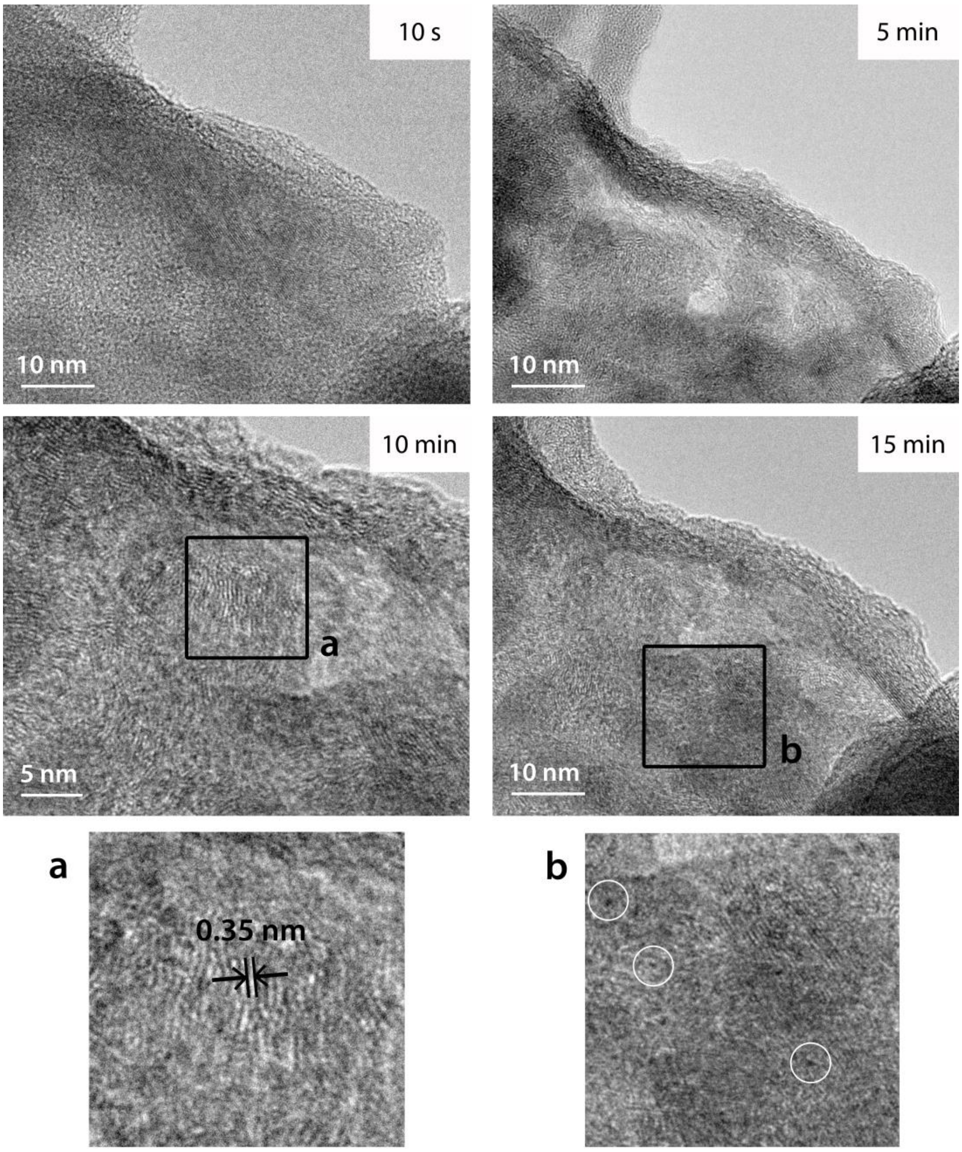

Figure 4.15. TEM images showing the 100 keV e-beam irradiation of an olivine sample with perylene over time. The magnified region ‘a’ shows the measured spacing between lines seen on the surface, and the region ‘b’ shows some examples of darker points, highlighted in white circles, which are likely to be Fe atoms.

It can be seen in Figure 4.15 that over time, the PAH-coated olivine sample does not undergo drastic changes in the same way as the olivine sample shown in Figure 4.14. The edge of the area of sample being observed is not etched as significantly as the bare olivine sample, and no obvious large nanoparticles are formed. The sample was not fully stable under the e-beam, however, as the carbon-coating was seen to move around on the surface as time went on. This is not unexpected, as the e-beam at this accelerating voltage causes ejection of H atoms from the PAH molecules,[38] leaving reactive radical sites at their edges. As a result, the PAHs are expected to react with each other (as seen in Chapter 3 of this Thesis), and in fact were never seen to settle into particular structures. The third image of the time series in Figure 4.15 is at a higher magnification, in which features can be seen such as lines across the surface of the sample. These have been enhanced further, in box 'a', and the measured distance between the observed lines was found to be ~ 0.35 nm – which corresponds to the interplanar spacing of graphitic layers. This confirms that the carbon layers are simply moving around on the surface of the olivine and no larger carbon structures, or metallic nanoparticles, appear to have formed. Furthermore, the magnified image shown in box 'b' of Figure 4.15 shows a number of small dark points, some of which are circled, that are likely to be due to atoms of Fe.

It appears from this behaviour that having a layer of carbon – in this case in the form of PAH molecules – shields the olivine sample from the e-beam such that the decomposition that was observed in Figure 4.14 is not seen. As Fe and C can interact very strongly, it may be that bonds are forming between the two elements, preventing the grouping together of Fe atoms to form nanoparticles.

The results of these experiments indicate that under irradiative conditions, 'bare' olivine grains can decompose and form metallic nanoparticles of Fe and MgO. This behaviour is not replicated when a coating of a carbon species (*i.e.* PAHs) is present. If the formation of metallic nanoparticles from olivine grains were to occur in astrophysical environments then it would mean the formation of new Fe catalytic particles – that are particularly associated with the formation of carbon nanostructures such as nanotubes in the laboratory. Interestingly, it seems that the formation of carbon nanostructures in this case could only occur upon deposition of carbon onto the grain *following* irradiation-induced nanoparticle formation, rather than as a result of irradiation of carbon-coated olivine grains.

4.6 Conclusions

This Chapter has discussed various aspects of astrophysically relevant grains, and their potential roles in catalytic processes. Olivine-type silicates and SiC grains have both been examined, covering carbon-rich, oxygen-rich and mixed-chemistry objects.

By means of experimental apparatus that has been used in previous studies on the formation of PAHs from acetylene over silicate grains, pyroxenes and alumina,[11, 17] the potential reactions of CO and H_2 over olivines were investigated. It was found that, when passing a mixture of CO and H_2 over catalytic grains – under vacuum and at 600 °C, a product was detected at an *m/z* value of 44. Through control reactions, it was determined that H_2 was not involved in any interactions or reactions, and that the molecule being detected was gaseous CO_2 as a product of the CO disproportionation reaction. Results indicate that Fe in the olivine structure is an important component in this process, with the higher Fe-containing olivine demonstrating a longer lifetime towards catalyst poisoning and a higher intensity product peak. CO disproportionation forms, as a second product, solid state carbon which is deposited onto the surface of the catalyst. The occurrence of this surface carbon deposition was confirmed by Raman spectroscopy, MALDI-TOF MS and TEM, all of which provided characterisation of the carbon, and determined that most of this carbonaceous material was amorphous. A separate experiment demonstrated that when the reaction proceeds under atmospheric pressure, the deposited carbon on the olivine surface was more highly ordered, and in the form of graphitic layers and multi-walled carbon nanotubes. The results of these experiments have significant astrophysical implications, providing a formation route to gaseous CO_2 – which is especially relevant to the Red Rectangle – in addition to a new source of carbon, which could lead to the formation of PAHs or other carbon structures. Finally, the results presented indicate strong evidence to support the idea of existence of carbon nanotubes in astrophysical environments.

To address the question of PAH formation in carbon-rich objects, experiments were carried out in which acetylene gas was passed over heated SiC grains under vacuum. The formation of small PAH molecules as a result of this was confirmed by the detection of naphthalene, anthracene or phenanthrene, and pyrene, along with several molecules that are likely to be intermediates in the

PAH formation process. This result provides a viable formation route to PAHs in environments such as the envelopes of mass-losing carbon-rich stars.

The behaviour of olivines under e-beam irradiation in TEM was investigated. It was found that when an olivine sample was exposed to the e-beam, over time the olivine began to decompose, and metallic nanoparticles were seen to form. These were characterised using EDX and by measuring the lattice *d*-spacing and it is postulated that both Fe nanoparticles and MgO nanoparticles were formed. If this behaviour were to occur in astrophysical environments, it would provide a route to the formation of new potentially catalytic surfaces. The experiment was repeated using an olivine sample that had been coated in carbon, by gas deposition of perylene. Interestingly, the carbon-coated olivine behaved differently under the e-beam to the ‘bare’ olivine sample; although the carbon material moved around on the olivine surface, no drastic decomposition or formation of metallic nanoparticles was observed. This indicates that ‘bare’ olivine grains that have decomposed under irradiation to form nanoparticles could then go on to act as catalysts upon adsorption of other species, but that already carbon-coated olivines, such as those expected following CO disproportionation, would be more shielded from irradiation, resulting in very little change in their structure.

The investigations reported in this Chapter provide insight into some of the roles and behaviour of astrophysically relevant grains that had not previously been explored. A new catalytic reaction involving CO and olivines has been identified, the formation of PAHs over SiC grains has been addressed, and the behaviour of olivines under irradiation has been investigated. The results of these studies not only add to the existing knowledge of astrophysical grains, but they also provide starting points for future investigations into mechanisms and limitations of these processes, which could be carried out using finely-tuned laboratory experiments and computational modelling.

4.7 References

1. B. T. Draine, *Annu. Rev. Astron. Astrophys.*, 2003, **41**, 241-289.
2. N. J. Woolf and E. P. Ney, *ApJ*, 1969, **155**, L181.
3. T. Henning, *Annu. Rev. Astron. Astrophys.*, 2010, **48**, 21-46.
4. F. Kemper, W. J. Vriend and A. Tielens, *ApJ*, 2004, **609**, 826-837.
5. L. Waters, F. J. Molster, T. deJong, D. A. Beintema, C. Waelkens, A. C. A. Boogert, D. R. Boxhoorn, T. deGraauw, S. Drapatz, H. Feuchtgruber, R. Genzel, F. P. Helmich, A. M. Heras, R. Huygen, H. Izumiura, K. Justtanont, D. J. M. Kester, D. Kunze, F. Lahuis, H. Lamers, K. J. Leech, C. Loup, D. Lutz, P. W. Morris, S. D. Price, P. R. Roelfsema, A. Salama, S. G. Schaeidt, A. Tielens, N. R. Trams, E. A. Valentijn, B. Vandenbussche, M. E. vandenAncker, E. F. vanDishoeck, H. vanWinckel, P. R. Wesselius and E. T. Young, *Astronomy & Astrophysics*, 1996, **315**, L361-L364.
6. C. Jäger, F. J. Molster, J. Dorschner, T. Henning, H. Mutschke and L. Waters, *Astron. Astrophys.*, 1998, **339**, 904-916.
7. L. B. F. M. Waters, C. Waelkens, H. van Winckel, F. J. Molster, A. G. G. M. Tielens, J. T. van Loon, P. W. Morris, J. Cami, J. Bouwman, A. de Koter, T. de Jong and T. de Graauw, *Nature*, 1998, **391**, 868-871.
8. D. A. Williams and S. D. Taylor, *Q. J. R. Astr. Soc.*, 1996, **37**, 565-592.
9. V. Pirronello, O. Biham, C. Liu, L. O. Shen and G. Vidali, *ApJ Lett.*, 1997, **483**, L131-L134.
10. V. Pirronello, C. Liu, L. Y. Shen and G. Vidali, *ApJ Lett.*, 1997, **475**, L69-L72.
11. M. Tian, B. S. Liu, M. Hammonds, N. Wang, P. J. Sarre and A. S. C. Cheung, *Phys. Chem. Chem. Phys.*, 2012, **14**, 6603-6610.
12. R. Treffers and M. Cohen, *ApJ*, 1974, **188**, 545.
13. T. Fujiyoshi, C. M. Wright and T. J. T. Moore, *MNRAS*, 2015, **451**, 3371 - 3384.
14. D. C. B. Whittet, W. W. Duley and P. G. Martin, *MNRAS*, 1990, **244**, 427-431.
15. A. K. Speck, G. D. Thompson and A. M. Hofmeister, *ApJ*, 2005, **634**, 426-435.

16. P. Merino, M. Švec, J. I. Martinez, P. Jelinek, P. Lacovig, M. Dalmiglio, S. Lizzit, P. Soukiassian, J. Cernicharo and J. A. Martin-Gago, *Nature Comm.*, 2014, **5**, 3054.

17. M. Tian, B. S. Liu, M. Hammonds, N. Wang, P. J. Sarre and A. S. C. Cheung, *Phil. Trans. R. Soc. A,* 2013, **371**, 20110590.

18. A. F. Holleman, E. Wiberg and N. Wiberg, *Inorganic Chemistry*, Academic Press, 2001.

19. T. Baird, J. R. Fryer and B. Grant, *Carbon*, 1974, **12**, 591-602.

20. D. L. Trimm, *Catal. Rev. Sci. Eng.*, 1977, **16**, 155-189.

21. H. J. Dai, A. G. Rinzler, P. Nikolaev, A. Thess, D. T. Colbert and R. E. Smalley, *Chem. Phys. Lett.*, 1996, **260**, 471-475.

22. P. Chen, H. B. Zhang, G. D. Lin, Q. Hong and K. R. Tsai, *Carbon*, 1997, **35**, 1495-1501.

23. P. Nikolaev, M. J. Bronikowski, R. K. Bradley, F. Rohmund, D. T. Colbert, K. A. Smith and R. E. Smalley, *Chem. Phys. Lett.*, 1999, **313**, 91-97.

24. Y. Kimura, J. A. Nuth and F. T. Ferguson, *Meteorit. Planet. Sci.*, 2006, **41**, 673-680.

25. T. J. Bernatowicz, S. Amari, E. K. Zinner and R. S. Lewis, *ApJ*, 1991, **373**, L73-L76.

26. K. E. Kuebler, B. L. Jolliff, A. Wang and L. A. Haskin, *Geochimica Et Cosmochimica Acta*, 2006, **70**, 6201-6222.

27. A. C. Ferrari and J. Robertson, *Phys. Rev. B*, 2000, **61**, 14095-14107.

28. R. Andrews, D. Jacques, D. L. Qian and T. Rantell, *Acc. Chem. Res.*, 2002, **35**, 1008-1017.

29. J. Cami, J. Bernard-Salas, E. Peeters and S. E. Malek, *Science*, 2010, **329**, 1180-1182.

30. K. Sellgren, M. W. Werner, J. G. Ingalls, J. D. T. Smith, T. M. Carleton and C. Joblin, *ApJ Lett.*, 2010, **722**, L54-L57.

31. K. Sellgren, M. W. Werner, J. G. Ingalls, J. D. T. Smith, T. M. Carleton and C. Joblin, in *PAHs and the Universe: A Symposium to Celebrate the 25th Anniversary of the PAH Hypothesis*, eds. C. Joblin and A. G. G. M. Tielens, E D P SCIENCES, 2011, vol. 46, pp. 209-214.

32. P. Ehrenfreund and B. H. Foing, *Science*, 2010, **329**, 1159-1160.

33. T. Q. Zhao, Q. Li, B. S. Liu, R. K. E. Gover, P. J. Sarre and A. S. C. Cheung, *Phys. Chem. Chem. Phys.*, 2016, **18**, 3489-3496.

34. S. Sasaki, K. Nakamura, Y. Hamabe, E. Kurahashi and T. Hiroi, *Nature*, 2001, **410**, 555-557.

35. M. J. Loeffler, C. A. Dukes, R. Christoffersen and R. A. Baragiola, *Meteorit. Planet Sci.*, 2016, **51**, 261-275.

36. M. J. Loeffler, C. A. Dukes and R. A. Baragiola, *J. Geophys. Res. Planets.*, 2009, **114**, E03003.

37. T. Selvamani, T. Yagyu, S. Kawasaki and I. Mukhopadhyay, *Catal. Commun.*, 2010, **11**, 537-541.

38. T. W. Chamberlain, J. Biskupek, S. T. Skowron, P. A. Bayliss, E. Bichoutskaia, U. Kaiser and A. N. Khlobystov, *Small*, 2015, **11**, 622-629.

5. Concluding remarks

The work described in this Thesis has utilised a combination of laboratory techniques and computational methods to address some of the outstanding questions in the field of astrochemistry. A variety of topics have been covered, including the variation in the profile of one of the aromatic infrared bands (AIBs), the formation of fullerenes in astrophysical environments, and the catalytic roles of some cosmic dust analogues.

Chapter 2 detailed a theoretical investigation into the relationship between the profile of the 11.2 μm AIB and the mass distribution of polycyclic aromatic hydrocarbons (PAHs). Astronomical spectra recorded at different positions within each of two objects – NGC 7023 and the Red Rectangle – show changes in the shapes of their 11.2 μm solo H out-of-plane (OOP) bend features as a function of offset from the exciting star. A previously reported computational model was employed to calculate the emission spectra of four neutral, solo H-containing PAHs, which were then used to fit the 11.2 μm band at each position within the two objects. By using the relative contribution of each of the PAHs to the fit, and categorising the included PAHs as either 'low-mass' ($N_C < 50$) or 'high-mass' ($N_C > 50$), a ratio of low-mass to high-mass PAHs was obtained for each spectrum which could be used as a tracer for the varying mass distribution of PAHs within each object. It was found that with increased offset from the star HD 200775 in NGC 7023, the proportion of low-mass PAHs increased, in line with a decrease in the intensity of the radiation field. The results of the model applied to spectra of the Red Rectangle showed little variation in the mass distribution of PAHs with increased offset, in contrast with the trends seen in other bands in the spectra, which indicate an increase in the proportion of high-mass PAHs with increased offset. It was concluded that for the Red Rectangle, a model including only four solo-containing PAHs was probably not sufficient to obtain an accurate interpretation of the varying profile of the 11.2 μm band.

The results obtained for NGC 7023 were in agreement with parallel studies that used alternative less specific methods, and reached broadly similar conclusions. This supports the profile-based emission model as a useful tool for investigating the profiles of the AIBs. The results also support the theory that the varying profile of the 11.2 μm band in particular can be explained in terms of the masses of the PAHs responsible for it – a band with a steep blue edge and less extended red tail being associated with a population of higher-mass PAHs, while a longer wavelength and more extended red tail can be associated with a population of lower-mass PAHs.

Chapter 3 described experiments carried out to explore the formation of the fullerene C_{60} from PAH molecules. Transmission electron microscopy (TEM) and matrix-assisted laser desorption/ionisation time-of-flight mass spectrometry (MALDI-TOF MS) were used as sources of electron beam (e-beam) and UV irradiation, respectively, to which PAH samples were exposed in order to investigate their resultant transformations. It was found that under either type of irradiation, PAHs lose one or more of their peripheral hydrogen atoms, creating reactive radical sites which initiate the creation of new bonds between molecules, resulting in the formation of larger PAH oligomer-type structures. These oligomers were seen to form in the direct-space imaging of TEM, and were detected in MALDI-TOF MS experiments at *m/z* values that made it possible to determine the potential structures of the species being formed. Of the PAHs studied, perylene and coronene exhibited C_{60} formation in MALDI-TOF MS studies, detectable by a peak at *m/z* = 720, while anthracene and pyrene showed formation of oligomers but no C_{60}. Mechanisms were proposed that gave detailed steps between the perylene and coronene oligomers and C_{60}, in which fjord and bay hydrogens were found to be important structural features for the formation of pentagons within the molecules. DFT calculations on fjord-containing PAHs showed that their vibrational spectra could feasibly be incorporated with a ‘typical’ AIB spectrum, and as such molecules with this structural feature may exist as part of astronomical PAH populations.

An experiment was designed and implemented to use TEM and MALDI-TOF MS in conjunction, to initiate and monitor transformations in the PAH sample. This experiment involved the low-dose TEM imaging of the sample before and after irradiating it with the UV laser in MALDI-TOF MS, and was used to confirm the formation of oligomers and C_{60} under these conditions. The novel use of these two techniques in combination prompted a comparative discussion about the cross-sections of decomposition for each PAH under each type of irradiation, and their respective lifetimes.

The formation of PAH oligomers and C_{60}, phenomena that were also replicated when irradiating mixtures of PAHs, is hugely significant in relation to the transformations of PAHs in astrophysical environments. The results provide experimental information that can be added to the widely discussed topic of fullerene formation in space, providing specific mechanistic steps and highlighting the importance of structural features such as fjord and bay hydrogens.

Chapter 4 includes a number of experiments designed to explore aspects of the catalytic roles of cosmic dust analogues, and carried out while the author visited Hong Kong University. A previously reported and purpose-built experimental setup was used to pass a mixture of H_2 and CO over heated olivine grains under vacuum. It was found that while H_2 was not involved in any reactions, CO underwent a disproportionation reaction over the grains, resulting in the detection of gaseous CO_2 by MS, and the deposition of solid-state carbon on the olivine surface. The nature of the deposited carbon was investigated, and was found to be mainly amorphous, with a small number of graphitic areas. The same reaction carried out at atmospheric pressure yielded deposited carbon in the form of graphitic layers and multi-walled carbon nanotubes, indicating that over very long timescales in astrophysical conditions, the same process may be expected to occur, providing evidence that nanotube structures may well exist in space. Aside from this, the disproportionation of CO on olivine grains provides a route to the formation of gaseous CO_2, which has been detected in the Red Rectangle, and to a source of solid carbon, capable of fragmenting to yield carbon-based species such as

PAHs, on the olivine surface. Experiments were carried out that involved reactions of acetylene over SiC grains, specifically focussing on the potential formation of PAH molecules as suspected occurs in mass-losing carbon stars. The results of these experiments revealed the formation of a number of small PAHs, along with other intermediate species, providing a route to PAH formation that can be applied to carbon-rich objects, in which olivines would not be found.

In a separate study, an isolated olivine sample was irradiated using the e-beam of TEM and its behaviour monitored. The sample was seen to decompose under irradiation, forming metallic nanoparticles that were characterised as MgO and pure Fe. The same behaviour in astrophysical environments would mean the formation of a new type of catalytic surface, and could have implications in the possible formation of structures such as carbon nanotubes which are found in terrestrial laboratory experiments. An olivine sample coated in perylene was irradiated using the same conditions and was found to behave in a way that indicated the shielding of the olivine by the carbon layer, *i.e.* no decomposition or nanoparticle formation.

In summary, the aim of the work presented in this Thesis has been to advance the knowledge of, and add evidence to, the field of astrochemistry, particularly in areas concerning carbon-containing species and carbon nanostructures. This has been achieved, providing a new way of interpreting the profile of one of the most investigated AIBs, finding a new route to the formation of C_{60} from small PAH precursors, and discovering further catalytic potential of cosmic dust analogues. The results that have been reported here can take their place alongside existing research to assist in the direction of future work, moving closer to finding absolute answers within some of the most discussed astrophysical topics.

6. Further work

Moving forward from the research described in this Thesis, it is worth considering work that may be carried out in the future to build upon and enhance the knowledge obtained through these studies. To that end, this final Chapter is included to present the author's opinions on the direction of future work in this area of research.

The emission model described and utilised in Chapter 2 of this Thesis, while still in its relative infancy, is already proving to be a useful tool in the analysis of the band profile of astrophysical emission features. To develop the model further, a greater understanding of the uncertainties in the values it obtains would be required. This, in addition to an expansion of the model to include a wider range of molecules, and sizes of molecule, would make this model a standout method for the study of the aromatic infrared bands.

In terms of laboratory astrochemistry, the focus must increasingly be on closing the gap between experimental and astrophysical conditions. The majority of issues and discrepancies that exist in experimental data arise from the inability to accurately replicate conditions relevant to the area of research. Parts of the work presented in this Thesis could be improved through the customisation of a commercial MALDI-TOF instrument to adapt three main conditions: lower temperatures of measurements, improved vacuum, and the use of a source of photons that could be controlled to an even higher degree.

More generally, the field of astrochemistry would benefit greatly from a continued and increased focus on the improvement of computational methods and the combination of theoretical and laboratory data. In addition to the development of techniques, there is a wider area for improvement. A greater level of communication between laboratory-based and theory-based research groups, in addition to a larger awareness of experimental and theoretical work outside of the field, would provide new, and perhaps unexpected, sources of inspiration for future lines of enquiry.